

Studies of Charged Higgs Boson Observability in the $H \rightarrow tb$ Decay at the ATLAS Experiment within the Minimal Supersymmetric Standard Model

DISSERTATION

zur Erlangung des akademischen Grades
Doctor rerum naturalium
(Dr. rer. nat.)

vorgelegt
der Fakultät Mathematik und Naturwissenschaften
der Technischen Universität Dresden

von
Diplom-Physiker Thomas Göpfert
geboren am 04. Februar 1979 in Freiberg

Gutachter: Prof. Dr. Michael Kobel
Prof. Dr. Heiko Lacker

Tag der Verteidigung: 15. Dezember 2010

Abstract

This thesis presents a Monte Carlo study of the search for charged Higgs bosons heavier than the mass of the top quark within the Minimal Supersymmetric Standard Model (MSSM) at the ATLAS experiment at the CERN Large Hadron Collider. Charged Higgs bosons are predicted in many non-minimal Higgs extensions of the Standard Model. Their discovery would be a clear signal for the existence of New Physics beyond the Standard Model, possibly the first experimental evidence to be found if the MSSM is realized in nature. The feasibility of detecting the heavy charged Higgs boson with a mass up to 600 GeV is studied in the decay channel $H^+ \rightarrow t\bar{b}$ for an integrated luminosity of 30 fb^{-1} at a center-of-mass energy of $\sqrt{s} = 10 \text{ TeV}$.

A major difficulty for charged Higgs boson reconstruction is the combinatorial background in the complex multi-jet final state environment. It is shown that this can be overcome by applying a kinematic fitting procedure and by a subsequent cut-based event and candidate selection. An iterative solution of the developed kinematic fit with non-linear constraints is presented. In addition, the reconstruction of charged Higgs bosons makes high demands on the ability to identify jets containing b -hadrons. A special b -tagging algorithm is introduced and a comparison with first ATLAS data is presented showing good agreement of the expected performance.

This study is performed with a realistic simulation of the ATLAS detector and takes into account all dominant experimental uncertainties and statistical uncertainties arising from limited Monte Carlo statistics. The result is given in terms of discovery and exclusion contours in the $(m_{H^+}, \tan\beta)$ parameter space in the m_h -max scenario of the MSSM. This study indicates that the heavy charged Higgs boson can be discovered in this decay channel only for large values of $\tan\beta$. It, however, can contribute to a combined H^+ sensitivity including other decay channels. Compared to previous studies the discovery reach could be improved.

Kurzfassung

Die vorliegende Arbeit präsentiert eine Monte Carlo Studie zur Suche nach geladenen Higgs Bosonen mit einer Masse größer als die des top Quarks im Kontext des Minimal Supersymmetrischen Standardmodells (MSSM) am ATLAS Experiment am CERN Large Hadron Collider. Geladene Higgs Bosonen werden von vielen Erweiterungen des Standardmodells vorhergesagt. Ihre Entdeckung wäre ein klares Indiz für neue Physik jenseits des Standardmodells, möglicherweise der erste experimentelle Befund für das MSSM. Eine Machbarkeitsstudie zur Entdeckung geladener Higgs Bosonen mit Massen bis zu 600 GeV im Zerfallskanal $H^+ \rightarrow t\bar{b}$ für eine integrierte Luminosität von 30 fb^{-1} und einer Schwerpunktsenergie von $\sqrt{s} = 10 \text{ TeV}$ wird vorgestellt.

Eine der Hauptschwierigkeiten bei der Rekonstruktion geladener Higgs Bosonen ist der durch den komplexen Endzustand mit vielen Jets auftretende kombinatorische Untergrund. Es wird gezeigt, dass die Rekonstruktion durch Anwendung eines kinematischen Fits mit anschließender schnittbasierter Ereignis- und Kandidatenselektion möglich ist. Eine iterative Lösung des entwickelten kinematischen Fits mit nicht-linearen Zwangsbedingungen wird vorgestellt. Des Weiteren stellt die Rekonstruktion geladener Higgs Bosonen hohe Ansprüche an die Möglichkeit, Jets, welche b -Hadronen beinhalten, zu identifizieren. Ein spezieller b -tagging Algorithmus wird vorgestellt und ein Vergleich mit den ersten ATLAS Daten zeigt eine gute Übereinstimmung mit den erwarteten Eigenschaften.

Die Studie wurde mit einer realistischen ATLAS Detektorsimulation durchgeführt und beinhaltet alle dominanten experimentellen Unsicherheiten sowie die statistische Unsicherheiten aufgrund begrenzt vorhandener simulierter Ereignisse. Die erwarteten Entdeckungs- und Ausschlusskonturen im m_h -max Szenario des MSSM werden als Funktion der geladenen Higgs Boson Masse und $\tan\beta$ gegeben. Die durchgeführte Studie zeigt, dass geladene Higgs Bosonen in diesem Zerfallskanal nur bei großen Werten von $\tan\beta$ entdeckt werden können. Dennoch kann dieser Zerfallskanal zur H^+ Sensitivität beitragen, wenn andere Zerfallskanäle mit in Betracht gezogen werden. Im Vergleich zu vorherigen Studien konnte die Sensitivität erhöht werden.

Contents

1	Introduction	1
2	Theoretical framework	3
2.1	The Standard Model of particle physics	3
2.1.1	Quantum Electrodynamics	5
2.1.2	Electroweak interactions	6
2.1.3	The Higgs mechanism	8
2.1.4	Theoretical constraints on the Standard Model Higgs boson mass	11
2.1.5	Experimental status of the Standard Model Higgs boson	12
2.2	Beyond the Standard Model	13
2.2.1	Motivation	14
2.2.2	Supersymmetry	16
2.2.3	The Minimal Supersymmetric Standard Model	17
2.3	The charged Higgs boson	19
2.3.1	The Two-Higgs-Doublet Model	20
2.3.2	Constraints in the MSSM	22
2.3.3	Production and decay modes of charged Higgs bosons	24
3	The ATLAS experiment at the Large Hadron Collider	27
3.1	Introduction	27
3.2	The ATLAS detector	29
3.2.1	The coordinate system	31
3.2.2	The magnet system	32
3.2.3	The inner detector	33
3.2.4	The calorimeter system	36
3.2.5	The muon spectrometer	37
3.2.6	Trigger and data acquisition	40
4	Outline of the analysis strategy	43
5	Analysis	45
5.1	Signal and Background	45
5.1.1	Physics background	45
5.1.2	Monte Carlo samples and cross-sections	45
5.2	Reconstruction of physics objects	47
5.3	Reconstruction of semileptonic top anti-top candidates	52
5.3.1	Final state reconstruction	53
5.3.2	Association of reconstructed objects to particles on Monte Carlo generator level	55
5.3.3	Event selection	57

5.4	Kinematic fit with constraints	62
5.4.1	Introduction	62
5.4.2	Fitting technique: non-linear least square fits with constraints . .	62
5.5	Kinematic fit of semileptonic top anti-top events	66
5.5.1	Four-vector parametrization	67
5.5.2	Constraints	72
5.5.3	Results	72
5.6	Reconstruction of charged Higgs bosons	78
6	Evaluation of systematic uncertainties	89
6.1	Experimental systematic uncertainties	89
6.2	Theoretical systematic uncertainties	90
6.3	Effects of the systematic uncertainties	90
7	Calculating significances	93
7.1	Introduction	93
7.2	The likelihood function	94
7.3	Discovery potential for $H \rightarrow tb$	96
7.4	Exclusion sensitivity for $H \rightarrow tb$	96
7.5	Results	96
8	Conclusion and outlook	99
A	Signal sample production	103
B	Resolutions	105
C	Variations in the kinematic fit	111
D	Additional discriminating variables	117
	Bibliography	127

1 Introduction

For several decades particle physicists have been striving for a complete theory describing the elementary particles in nature and their fundamental interactions. The current knowledge is summarized in the so-called Standard Model of particle physics which successfully describes the constituents of known matter and three of the four interactions between them: the strong, weak and electromagnetic interactions. Gravity, an attractive force acting on large scales, is negligible for the description of the interactions of elementary particles and is not incorporated in the Standard Model but described by general relativity. The Standard Model is based on symmetries that seem to be realized in nature. Within this model, interactions between the known elementary particles, which are spin- $1/2$ fermions, are described in terms of a local gauge theory where forces are mediated by the exchange of spin-1 bosons. The Standard Model has successfully been validated by high precision measurements to correctly describe the three interactions at energies currently accessible by experiments. However, one fundamental pillar remains experimentally unverified: the origin of particle masses. Within the Standard Model, particle masses are generated by the electroweak symmetry breaking mechanism which entails a new scalar particle, the Higgs boson. Since its prediction in 1964, particle physicists have been eagerly striving for a discovery of the Higgs boson at particle accelerators such as the Large Electron Positron (LEP) collider at CERN¹ and the Tevatron at Fermilab. While the allowed mass range has been constrained, the Higgs boson remains the last undiscovered particle in the Standard Model.

As already mentioned before, the Standard Model is based on symmetry principles. It seems natural to explore if these symmetries can be extended. One example of such an extension is Supersymmetry, where for each fermion a bosonic partner particle is predicted and vice versa. Besides complementing the symmetries of the Standard Model, Supersymmetry can also resolve some aesthetic shortcomings of the Standard Model. Several supersymmetric extensions of the Standard Model models exist, with the Minimal Supersymmetric Standard Model (MSSM) being the most economic in terms of the amount of new particles predicted and the number of free parameters. In the MSSM only partner particles of the Standard Model particles are added, but nothing else. In addition to the existence of the supersymmetric partner particles, the MSSM predicts more than one physical Higgs bosons, three neutral and two charged ones.

Charged Higgs bosons appear in many extensions of the Standard Model, such as Two Higgs Doublet Models (2HDMs). Their discovery would be a clear signal for the existence of New Physics beyond the Standard Model, possibly the first experimental evidence to be found if the MSSM is realized in nature.

In the year 2000, LEP was decommissioned in order to allow for the construction of its successor, the Large Hadron Collider (LHC) which will provide proton-proton collisions at a yet unrivaled center-of-mass energy of 14 TeV and a design luminosity of up to

¹CERN - Conseil Européene pour la Recherche Nucléaire

$10^{34} \text{ cm}^{-2}\text{s}^{-1}$. Since November 2009, the LHC is the highest energy particle accelerator in the world. It is by now capable of accelerating protons to energies of up to 3.5 TeV and colliding them, thus opening a gateway to the TeV scale. Subsequently, the center-of-mass energy will be increased up to the design value. Due to the large increase in energy compared to former accelerators and due to the expected unprecedented rate of interactions, the LHC will be able to produce the Higgs boson, if it exists.

One of the experiments at the LHC is the ATLAS experiment. It is one of the two general-purpose detectors designed to study the full physics spectrum of proton-proton interactions provided by the LHC.

Within this thesis a study of the ATLAS discovery potential for charged Higgs bosons heavier than the mass of the top quark is presented. This work is based on simulated data, so-called Monte Carlo, and only considers the 2HDM, in particular in the context of the MSSM which is a so-called Type II 2HDM. For such high masses of the charged Higgs boson the decay into a top and a b quark dominates. This decay mode is subject in the presented study. This channel has previously been studied in ATLAS at a center-of-mass energy of 14 TeV. No discovery or exclusion power could be extracted. Special emphasis is placed on improving the discovery reach by applying a different analysis technique.

This thesis is organized as follows:

Chapter 2 introduces the theoretical framework of the Standard Model and the MSSM with a special emphasis on the Higgs sector.

Chapter 3 reports about the design and performance of the ATLAS experiment, which is used to detect the decay products of the charged Higgs boson investigated in this thesis. The LHC and all ATLAS subdetectors are briefly described.

Chapter 4 gives a short outline of the analysis method used for the detections of charged Higgs bosons.

Chapter 5 describes the measurement in more detail. The datasets used in this study, basic reconstruction criteria and event selection methods are introduced. An overview about kinematic fits in general and the mathematics of the general non-linear least square fit technique using Lagrange multipliers is given together with its application for the reconstruction of semileptonic top anti-top events. Finally, the cut-based selection of charged Higgs bosons decaying into a top and a b quark in the MSSM is described.

Chapter 6 summarizes the evaluation of the main systematic uncertainties that have been considered in the evaluation of the charged Higgs boson discovery potential. The obtained uncertainties are discussed.

Chapter 7 introduces the method and gives the evaluated result of the ATLAS discovery potential of charged Higgs bosons decaying into a top and a b quark in the MSSM.

Chapter 8 closes with a summary and an outlook.

2 Theoretical framework

2.1 The Standard Model of particle physics

The Standard Model of particle physics (SM) is a consistent theory of fundamental microscopic interactions that successfully explains most of the known phenomena in elementary particle physics. The SM describes the strong, the electromagnetic and the weak interactions and it provides a description of nature that so far accounts for almost all observed microscopic phenomena. For example, the forces that hold together the quarks in the nucleus and the protons and neutrons in the atomic nuclei are due to strong interactions, the binding of electrons to nuclei in atoms or of atoms in molecules is caused by electromagnetism and the energy production in the sun and other stars occurs through nuclear reactions induced by weak interactions. In principle, the gravitational force should also be included in the list of fundamental interactions but their impact on fundamental particle processes at accessible energies is negligible.

The Standard Model is a gauge theory, based on the symmetry group $SU(3)_C \otimes SU(2)_L \otimes U(1)_Y$, where the $SU(3)_C$ subgroup characterizes the strong interaction and the $SU(2)_L \otimes U(1)_Y$ subgroup describes the mixed electromagnetic and weak interactions as formulated in the Glashow-Weinberg-Salam model (cf. [1–3]).

The gauge fields associated with the generators of the algebra of the particular symmetry group are:

$$\begin{array}{ccc}
 SU(3)_C & \otimes & SU(2)_L & \otimes & U(1)_Y \\
 \downarrow & & \downarrow & & \downarrow \\
 8G_\mu^a & & 3W_\mu^a & & B_\mu \\
 a = 1, \dots, 8 & & a = 1, 2, 3 & &
 \end{array} \tag{2.1}$$

The interactions are described by the exchange of the spin-one gauge bosons. The eight massless particles, linear combinations of G_μ^a , associated with the factor $SU(3)_C$ are called gluons and the subscript ‘‘C’’ is meant to denote *color*, the quantum number of the strong interaction. Three spin-one particles, linear combinations of W_μ^a , are associated with the factor $SU(2)_L$, and one, B_μ , with the factor $U(1)_Y$. The subscript ‘‘L’’ is meant to indicate that only the left-handed fermions turn out to carry this quantum number. The subscript ‘‘Y’’ is meant to distinguish the group associated with the quantum number of weak hypercharge, denoted by Y, from the group associated with ordinary electric charge. The electromagnetic group is written as $U(1)_{em}$. The four spin-one bosons associated with the factors $SU(2)_L \otimes U(1)_Y$ are related to the physical bosons that mediate the weak interactions, W^\pm and Z, and the photon, γ , in a way will be explained in the next Sections.

With the current experimental knowledge, the fermionic content is given by quarks and leptons, both having spin-1/2. They can be organized in three generations with increasing mass as illustrated in Table 2.1. For the quarks the mass eigenvalues corresponding to the eigenstates participating in strong interactions are listed. For the d , s , b quarks and the neutrinos, the interaction eigenstates are different from the mass eigenstates. The three

2 Theoretical framework

Generation	Particle	Electric charge [e]	Mass	
first	e	electron	1	0.511 MeV ¹
	ν_e	electron neutrino	0	$m_{\nu_e}^{\text{eff.}} = \sqrt{\sum_i U_{ei} ^2 m_{\nu_i}^2} < 2 \text{ eV}$
	u	up quark	+2/3	1.7-3.3 MeV
	d	down quark	-1/3	4.1-5.8 MeV
second	μ	muon	1	105.7 MeV
	ν_μ	muon neutrino	0	$m_{\nu_\mu}^{\text{eff.}} = \sqrt{\sum_i U_{\mu i} ^2 m_{\nu_i}^2} < 0.19 \text{ MeV}$
	c	charm quark	+2/3	101 MeV
	s	strange quark	-1/3	1.27 GeV
third	τ	tau	1	1176.8 MeV
	ν_τ	tau neutrino	0	$m_{\nu_\tau}^{\text{eff.}} = \sqrt{\sum_i U_{\tau i} ^2 m_{\nu_i}^2} < 18.2 \text{ MeV}$
	t	top quark	+2/3	172.0 GeV
	b	bottom quark	-1/3	4.2 GeV

Table 2.1: Fundamental fermionic content of the Standard Model organized in three generations. Their electric charge and mass (or upper limit) is given [4]. Their corresponding anti-particles are also included in the SM. The matrix elements U_{ei} , $U_{\mu i}$ and $U_{\tau i}$ connect the mass and weak eigenstates of the neutrinos. The corresponding matrix for the quarks is left out.

fermionic families appear to have identical gauge couplings and they differ only by their mass and flavor quantum numbers. The electromagnetic force only acts on electrically charged particles, the strong force only on quarks and the weak interaction acts on all fermions.

The gauge symmetry of the SM is broken by the vacuum causing the Spontaneous Symmetry Breaking (SSB) of the electroweak group to the electromagnetic subgroup:

$$SU(3)_C \otimes SU(2)_L \otimes U(1)_Y \xrightarrow{SSB} SU(3)_C \otimes U(1)_{em} . \quad (2.2)$$

The SSB mechanism generates the masses of the weak gauge bosons and gives rise to the appearance of a physical scalar particle, the so-called Higgs boson. The fermion masses and mixings are also generated through the SSB.

The following Sections give a short summary of the electroweak sector of the SM, i.e. the $SU(2)_L \otimes U(1)_Y$ part. The strong $SU(3)_C$ piece is discussed in more detail in Reference [5]. The power of the gauge principle is shown in Section 2.1.1, where the simpler Lagrange density of quantum electrodynamics is derived. In Sections 2.1.2 and 2.1.3 the electroweak gauge sector and the SSB mechanism is presented and discussed. Sections 2.1.4

¹Within this thesis a system of units is used where $\hbar = c = 1$.

and 2.1.5 summarize the phenomenological and experimental status of the Higgs boson searches, which is predicted by the mechanism of Spontaneous Symmetry Breaking.

2.1.1 Quantum Electrodynamics

The simplest local gauge theory is quantum electrodynamics (QED). It is based on the $U(1)_{em}$ symmetry group which can be described mathematically as a phase transformation of the Dirac spinors of charged fermions. The Lagrangian density describing a free Dirac fermion field ψ_f with spin-1/2 and of mass m_f is given by

$$\mathcal{L}_0 = i\bar{\psi}\gamma^\mu\partial_\mu\psi - m_f\bar{\psi}\psi, \quad (2.3)$$

where γ^μ are the Dirac matrices. \mathcal{L}_0 is invariant under *global* $U(1)$ transformation

$$\psi(x) \xrightarrow{U(1)} \psi'(x) = e^{iq\theta}\psi(x), \quad (2.4)$$

where $q\theta$ is an arbitrary real constant. Hence, the global phase of the fermion field is then pure convention and has no physical meaning. However, the Lagrangian density is not invariant if the phase transformation is dependent on the space-time coordinate, i.e. not invariant under *local* phase redefinition $\theta = \theta(x)$, because

$$\partial_\mu\psi(x) \xrightarrow{U(1)} e^{iq\theta}(\partial_\mu + iq\partial_\mu\theta)\psi_\mu. \quad (2.5)$$

The *gauge principle* requires that the invariance of the Lagrangian under $U(1)_{em}$ phase transformation holds locally. This is only possible if an additional term is added to the Lagrangian density which transforms in such a way that it cancels the $\partial_\mu\theta$ part in Eq. 2.5. This can be achieved by introducing a new spin-one field A_μ that transforms as

$$A_\mu \xrightarrow{U(1)} A'_\mu = A_\mu + \frac{1}{e}\partial_\mu\theta \quad (2.6)$$

and by defining the covariant derivative $D_\mu = \partial_\mu - iqeA_\mu$. The resulting Lagrangian

$$\mathcal{L}_{QED} = \mathcal{L}_0 + \underbrace{eqA_\mu\bar{\psi}\gamma^\mu\psi}_{\mathcal{L}_{int}} - \underbrace{\frac{1}{4}F_{\mu\nu}F^{\mu\nu}}_{\mathcal{L}_{kin,A_\mu}}, \quad (2.7)$$

where $F^{\mu\nu} = \partial_\mu A_\nu - \partial_\nu A_\mu$ is the usual electromagnetic field tensor, is then invariant under local $U(1)$ transformation. The gauge principle has generated an interaction, described by \mathcal{L}_{int} , between the gauge field A_μ and the fermions that is proportional to its electric charge q . The gauge invariant kinematic term \mathcal{L}_{kin,A_μ} is added in addition to the Lagrangian to have a true propagating field A_μ that can be identified with the photon. To preserve local gauge invariance, any explicit mass term for the photon is forbidden, as such a term in the Lagrangian would need to be of the form $\mathcal{L}_m = \frac{1}{2}m^2 A^\mu A_\mu$ and would not be invariant under the gauge transformation. Experimentally, it is known that $m_\gamma < 7 \cdot 10^{-19}$ eV [6].

The Lagrangian density in Eq. 2.7 gives rise to the well known Maxwell equations:

$$\partial_\mu F^{\mu\nu} = J^\nu, \quad J^\nu = -eq\bar{\psi}\gamma^\mu\psi, \quad (2.8)$$

where J^ν is the fermion electromagnetic current.

The QED Lagrangian in Eq. 2.7 is derived from a simple gauge symmetry requirement leading to a very successful quantum field theory. QED has been tested to very high levels of precision and all experiments agree with the prediction from theory. This enormous success of local gauge theory has inspired the development of gauge theories for the other interactions observed in nature.

2.1.2 Electroweak interactions

One important requirement in describing weak interactions is that the underlying theory has to be a chiral gauge theory. This means that the building blocks are massless left- and right-handed fermions:

$$\psi_L = \frac{1}{2}(1 - \gamma^5)\psi, \quad \psi_R = \frac{1}{2}(1 + \gamma^5)\psi. \quad (2.9)$$

Low-energy experiments have provided a large amount of information about the dynamics of flavor-changing processes. The detailed analysis of the energy and angular momentum of β -decays (cf. [7–9]) showed that only left-handed (right-handed) fermion (anti-fermion) chiralities participate in those weak interaction. In addition, it is shown that neutrinos have left-handed chirality while anti-neutrinos are right-handed.

The corresponding gauge groups are chosen in a way that this is reflected. The symmetry group representation to consider is $SU(2)_L \otimes U(1)_Y$. The quantum number of the $SU(2)_L$ is the *weak isospin* T_W and the one for the $U(1)_Y$ the *weak hypercharge* Y . The irreducible representations of the $SU(2)_L$ group are charged doublets and chargeless singlets. Since the weak isospin interaction acts only on left-handed fermions it is natural to assign them to the doublets and the right-handed fermions to the singlet. The $U(1)_Y$ group has only a one-dimensional representation. They have different hypercharges in the $SU(2)_L$ doublet and singlet representation. The hypercharge quantum number is related to the electric charge q and the third component of the weak isospin T_W^3 by the Gell-Mann-Nishijima relation,

$$Y = 2(q - T_W^3). \quad (2.10)$$

The fundamental fermions and their assignment to the doublets and singlets, along with their quantum numbers are shown in Table 2.2. Right-handed neutrinos have been added to the Standard Model particle content, although these are singlets under all Standard Model gauge groups. They are needed within the Standard Model only if the neutrinos are massive. Experimental results show that they have a small rest mass [10–14]. Non zero neutrino masses have no significant impact on the results of this work.

The Lagrangian density describing the dynamics and electroweak interactions of the fermion fields is given by

$$\mathcal{L} = \sum_{i=1,2,3} i\bar{\psi}_L^i \gamma_\mu \mathcal{D}_L^\mu \psi_L^i + \sum_{i=1,2,3} i\bar{\psi}_R^i \gamma_\mu \mathcal{D}_R^\mu \psi_R^i - \frac{1}{4} \vec{W}_{\mu\nu} \vec{W}^{\mu\nu} - \frac{1}{4} B_{\mu\nu} B^{\mu\nu}, \quad (2.11)$$

	T_W	T_W^3	q	Y
Quarks				
$Q_L^i = \begin{pmatrix} u^i \\ d^i \end{pmatrix}_L$, $u^i = u, c, t$ $d^i = d', s', b'$	1/2	+1/2	+2/3	+1/3
$u_R^i = u_R, c_R, t_R$	0	0	+2/3	+4/3
$d_R^i = d'_R, s'_R, b'_R$	0	0	-1/3	-2/3
Leptons				
$L_L^i = \begin{pmatrix} \nu^i \\ \ell^i \end{pmatrix}_L$, $\nu^i = \nu_e, \nu_\mu, \nu_\tau$ $\ell^i = e, \mu, \tau$	1/2	+1/2	0	-1
$\nu_R^i = \nu_{eR}, \nu_{\mu R}, \nu_{\tau R}$	0	0	0	0
$\ell_R^i = e_R, \mu_R, \tau_R$	0	0	-1	-2

Table 2.2: Fundamental representation of quarks and leptons in the electroweak interaction. The fields Q_L and L_L are left-handed quark and lepton doublets, respectively. The right-handed singlet fields are indicated by the subscript R. The given quantum numbers are the weak isospin T_W , the third component of the weak isospin T_W^3 , the electric charge q and the weak hypercharge Y .

where ψ_L^i is either the left-handed quark doublet Q_L^i or the left-handed lepton doublet L_L^i . ψ_R^i are the right-handed quark and lepton fields u_R^i, d_R^i, ℓ_R^i or ν_R^i , respectively. The index i denotes the flavor generation index. D_L^μ and D_R^μ are the covariant derivatives of the left- and right-handed fields,

$$D_L^\mu = \partial^\mu + ig \frac{\vec{\sigma}}{2} \vec{W}^\mu + ig' Y_W B^\mu, \quad D_R^\mu = \partial^\mu + ig' Y_W B^\mu, \quad (2.12)$$

with the Pauli matrices $\vec{\sigma}$ as the generators of the $SU(2)_L$ group, Y_W as the hypercharge operator and g and g' as the coupling constant of the two gauge groups. The gauge fields are W_μ^1, W_μ^2 and W_μ^3 for $SU(2)_L$ and B_μ for $U(1)_Y$. The dynamic of the weak and hypercharge gauge fields are described by the field strength tensors $\vec{W}^{\mu\nu}$ and $B^{\mu\nu}$. They are given by $\vec{W}_{\mu\nu} = \partial_\mu \vec{W}_\nu - \partial_\nu \vec{W}_\mu + ig \vec{W}^\mu \times \vec{W}^\nu$ and $B_{\mu\nu} = \partial_\mu B_\nu - \partial_\nu B_\mu$. However, the four gauge fields \vec{W}_μ and B_μ are not the fields observed in nature. W_μ^1 and W_μ^2 mix to the physical W^\pm bosons states:

$$W_\mu^\pm = \frac{W_\mu^1 \mp iW_\mu^2}{\sqrt{2}}. \quad (2.13)$$

The B_μ field cannot be the photon, since it would couple to hypercharged neutrinos. Also the third component of \vec{W}^ν cannot be the Z boson, which also couples to right-handed fermions. Rather the physical fields have to be mixtures of these two, and they can be expressed as:

$$\begin{pmatrix} Z_\mu \\ A_\mu \end{pmatrix} = \begin{pmatrix} \cos \theta_W & \sin \theta_W \\ -\sin \theta_W & \cos \theta_W \end{pmatrix} \begin{pmatrix} W_\mu^3 \\ B_\mu \end{pmatrix}, \quad (2.14)$$

with the Weinberg mixing angle θ_W .

Experimental observations show that the quarks, leptons and weak gauge bosons are massive with the exception of the photon. Up to this point all gauge and fermion fields appearing in the electroweak Lagrangian (cf. Eq. 2.11) are massless, i.e. the Lagrangian contains no mass term. And as explained before, gauge invariance even forbids explicit mass terms for the gauge bosons. Furthermore, in contrast to QED, it is also not possible to insert explicit fermion mass terms since they would mix left- and right-handed fermions and are also not gauge invariant under the $SU(2)_L \otimes U(1)_Y$ group. Therefore, a dedicated mechanism had to be devised in the Standard Model to solve this problem. This will be explained in more detail in the next Section.

2.1.3 The Higgs mechanism

A possible solution to the above mentioned problems, inspired by similar phenomena in the study of spin systems, was proposed by several physicists in 1964 [15–17], and it is known as the *Higgs mechanism*. The principle of this mechanism is Spontaneous Symmetry Breaking.

In the Standard Model, electroweak symmetry breaking is achieved by an additional scalar field, the Higgs field, with an appropriate potential. One of its components acquires a vacuum expectation value that spontaneously breaks the gauge symmetry. Fermions and gauge bosons interacting with this field acquire an effective mass while still preserving the gauge invariance of the theory.

The Higgs mechanism is implemented in the SM by introducing a complex scalar field ϕ ,

$$\phi = \begin{pmatrix} \phi^+ \\ \phi^0 \end{pmatrix} = \begin{pmatrix} \phi_3 + i\phi_4 \\ \phi_1 + i\phi_2 \end{pmatrix}, \quad (2.15)$$

as a doublet of $SU(2)_L$ with hypercharge $Y = +1$. It contains four real scalar fields $\phi_{1,2,3,4}$ representing four degrees of freedom. The gauge invariant Lagrangian of this model containing a kinematic term and a potential $V(\phi)$ is given by

$$\mathcal{L}_\phi = (D_\mu \phi)^\dagger (D^\mu \phi) - V(\phi), \quad (2.16)$$

with

$$V(\phi) = \mu^2 \phi^\dagger \phi + \lambda (\phi^\dagger \phi)^2 \quad (2.17)$$

with the left-handed covariant derivative D_μ from Eq. 2.12. The shape of the potential $V(\phi)$ depends on the parameters μ^2 and λ . The latter has to be positive so that the total energy is bounded from below. For the case $\mu^2 > 0$, the lowest point of the potential corresponds to $\phi_1 = \phi_2 = \phi_3 = \phi_4 = 0$ and a zero vacuum energy. Only for $\mu^2 < 0$ spontaneous symmetry breaking occurs. The shape of the potential for this case is sketched in Figure 2.1 in dependence of two of the components. The minimum of the potential is now at non-zero values, although the potential is still symmetric with respect to the origin. This is the analogy of the still present, but broken, gauge symmetry.

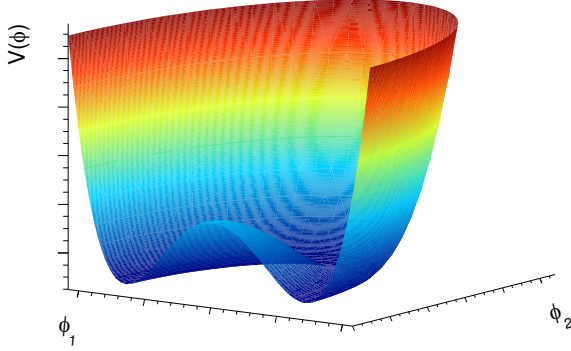


Figure 2.1: Shape of the scalar potential $V(\phi)$ with $\phi = \phi_1 + i\phi_2$ for a negative value of μ^2 .

There is an infinite set of degenerated states with minimum energy with a field “length” ρ with

$$\rho_0 = \sqrt{\phi^\dagger \phi} = \sqrt{\frac{-\mu^2}{2\lambda}} \equiv \frac{v}{\sqrt{2}}. \quad (2.18)$$

Where $v = |\mu|/\sqrt{\lambda}$ denotes the vacuum expectation value. The position of the minima in the two-dimensional space of weak isospin is not fixed. The ground states, where all of them are equivalent, can be parametrized by

$$\phi_{min} = e^{i\vec{\sigma}\vec{\psi}} \frac{1}{\sqrt{2}} \begin{pmatrix} 0 \\ v \end{pmatrix}, \quad (2.19)$$

with $|\vec{\psi}| < 2\pi$. From an arbitrary but fixed point in the minimum the $SU(2)_L \otimes U(1)_Y$ symmetry gets spontaneously broken. Choosing one such point with only one non-vanishing field component, e.g.

$$\phi_0 = \frac{1}{\sqrt{2}} \begin{pmatrix} 0 \\ v \end{pmatrix}, \quad (2.20)$$

corresponds to spontaneous symmetry breaking. In this way, the vacuum expectation value has non-vanishing hypercharge and weak isospin quantum numbers, thus spontaneously breaking both the $SU(2)_L$ and the $U(1)_Y$ gauge groups. The $U(1)_{em}$ gauge group remains unbroken since the vacuum state has no electric charge. The excitations of the field around the ground state have to be interpreted as particles. Seen from the chosen vacuum state there are three directions in which the energy is unchanged (in Figure 2.1 only one of these is visible). These correspond to massless bosons that would also be visible as non-vanishing values for ϕ_2 , ϕ_3 and ϕ_4 . They are called the Goldstone bosons and are unphysical states that can be removed by a gauge transformation, the so-called *unitary gauge*. Their degrees of freedom are absorbed by the additional degrees of freedom that the weak gauge bosons acquire when becoming massive.

In addition to these massless excitations, there is one massive excitation along the ϕ_1 direction which can be parametrized as:

$$\phi = \frac{1}{\sqrt{2}} \begin{pmatrix} 0 \\ v + H(x) \end{pmatrix}. \quad (2.21)$$

The covariant derivative (cf. Eq. 2.12) couples the scalar multiplet to the electroweak gauge bosons. With the physical unitary gauge, the kinetic term of the scalar potential (cf. Eq. 2.16) takes the form:

$$(D_\mu \phi)^\dagger (D^\mu \phi) = \frac{1}{2} \partial_\mu H \partial^\mu H + (v + H)^2 \left\{ \frac{g^2}{4} W_\mu^\dagger W^\mu + \frac{g^2}{8 \cos^2 \theta_W} Z_\mu Z^\mu \right\}. \quad (2.22)$$

The vacuum expectation value of the neutral scalar has generated a quadratic term for the W^\pm and Z bosons, i.e. those gauge bosons acquired masses,

$$M_Z \cos \theta_W = M_W = \frac{1}{2} v g, \quad (2.23)$$

while the photon remains massless. Furthermore, scalar field interactions with the gauge bosons appear and they are proportional to their mass. Hence, the elaborated theoretical framework implies the existence of massive intermediate gauge bosons, W^\pm and Z and moreover, the SSB mechanism gives a precise prediction for its masses, relating them to the vacuum expectation value.

Inserting Eq. 2.21 into Eq. 2.17 the scalar potential becomes:

$$V(\phi) = \mu^2 H^2 - \lambda v H^3 - \frac{1}{4} \lambda H^4. \quad (2.24)$$

Triple and quartic scalar field self-couplings as well as a mass term is apparent. This massive scalar particle with $m_H = \sqrt{-2\mu^2} = \sqrt{2\lambda} v$ is called the Higgs boson and has not yet been found, but it is predicted by the electroweak Standard Model.

From experimental point of view the measurement of the Fermi coupling, e.g. through the measurement of the muon lifetime [4], gives a direct determination of the electroweak scale, i.e. the scalar vacuum expectation value:

$$v = (\sqrt{2} G_F)^{-1/2} = 246 \text{ GeV}. \quad (2.25)$$

Hence, the physics of the SM Higgs boson is actually just a function of its mass m_H , since its second free parameter, v , is known.

The Higgs mechanism does not directly provide fermion mass terms. However, it is possible to generate the masses in a gauge invariant way by using dimensionless Yukawa couplings of the fermions to the Higgs field. This can be done by adding the following term to the Lagrangian:

$$\mathcal{L}_{Yukawa} = -\Gamma_u^{ij} \bar{Q}_L^i \phi^c u_R^j - \Gamma_d^{ij} \bar{Q}_L^i \phi d_R^j - \Gamma_\ell^{ij} \bar{L}_L^i \phi \ell_R^j + h.c., \quad (2.26)$$

where $\phi^c = -i\sigma^2\phi^*$ and Γ_f ($f = u, d, \ell$) are matrices of couplings arbitrarily introduced to realize the Yukawa coupling between the field ϕ and the fermionic fields of the SM. Q_L^i and L_L^i (with $i = 1, 2, 3$ as generation index) represent quark and lepton left-handed doublets of $SU(2)_L$, while u_R^i, d_R^i and l_R^i are the corresponding right-handed singlets. When the scalar field ϕ acquires a non zero vacuum expectation value through SSB, each fermionic degree of freedom coupled to ϕ develops a mass term with a mass parameter

$$m_f = \Gamma'_f \frac{v}{\sqrt{2}}, \quad (2.27)$$

where the process of diagonalization from the current eigenstates in Eq. 2.26 to the corresponding mass eigenstates is understood, and Γ'_f are therefore the elements of the diagonalized Yukawa matrices corresponding to a given fermion f .

The Yukawa couplings of the f fermion to the Higgs boson is proportional to Γ'_f . As long as the origin of fermion masses is not better understood in some more general context beyond the SM, the Yukawa couplings represent free parameters of the Standard Model Lagrangian.

Right-handed neutrinos could be added to the Standard Model particle content, although these are singlets under all Standard Model gauge groups. This will lead to so-called neutrino Dirac mass terms by interactions with the Higgs field as in the case for the other fermions. Another possible mass term for neutrinos would be a so-called Majorana mass term, which is not discussed here.

2.1.4 Theoretical constraints on the Standard Model Higgs boson mass

Even though the mass of the Higgs boson cannot be predicted in the Standard Model, upper and lower bounds can nevertheless be derived from internal consistency conditions and extrapolations of the model to high energies. It is possible to place constraints on it by requiring the SM to be a unitary, perturbative and stable theory up to an energy scale Λ where new physics might appear. A comprehensive discussion of these constraints can be found in Reference [18].

In order that certain processes like $W^+W^- \rightarrow W^+W^-$ yield unitary scattering amplitudes, the Higgs boson mass has to be smaller than about 780 GeV.

Other constraints can be derived from radiative corrections to the quartic coupling parameter λ . From the need that the coupling remains perturbative, which means that no trivial Landau pole appears, up to a scale Λ an upper bound on the Higgs boson mass can be given (so-called *triviality* bound). The Higgs boson mass can be limited from below by demanding λ to be positive up to the cut-off scale (so-called *vacuum stability* bound). The allowed region for the mass of the Higgs boson from these theoretical considerations is shown in Figure 2.2 in dependence of the scale Λ up to which the Standard Model is assumed to be valid and a stable and perturbative theory.

If the Standard Model is assumed to be valid up to the scale of grand unification (GUT) of about 10^{16} GeV, the scale where gravity is predicted to become a strong force, the

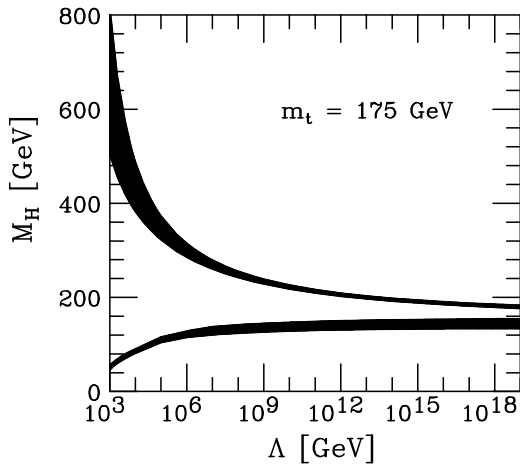


Figure 2.2: Theoretically allowed region for the Higgs boson mass m_H in dependence of the cut-off scale Λ . The limits have been derived by demanding the Higgs quartic coupling λ to be positive and finite up to Λ (from [19]). The bands indicate the theoretical uncertainties.

Higgs mass is restricted to a narrow window between 130 and 190 GeV. The observation of a Higgs mass above or below this window would demand a new physics scale below the GUT scale.

2.1.5 Experimental status of the Standard Model Higgs boson

In addition to the theoretical constraints already discussed, the Higgs sector has already been probed for the past decades in experiments. No conclusive signal of a Standard Model Higgs boson signatures has been found yet. In this Section a short overview of existing indirect and direct searches for the SM Higgs boson is given.

Indirect bounds from electroweak precision measurements

Assuming that the Standard Model is the correct theory, virtual Higgs field excitations contribute to several observables, like e.g. the W boson mass or the electroweak mixing angle $\sin\theta_W$. Since the Higgs boson mass is the only parameter in the SM that is not directly determined neither by theory nor by experiment, it can be extracted indirectly from precision fits of all measured electroweak observables.

The $\Delta\chi^2$ of a global fit of all Standard Model parameters to the precision observables is shown in Figure 2.3 in dependence of the assumed Higgs boson mass [20, 21]. Within the SM a light Higgs boson is preferred.

Direct searches

The Higgs boson has been searched for in collider experiments for the last decades. No signal was found, but it was possible to place limits on its mass assuming Standard Model production cross-sections.

The four LEP experiments have searched for the Higgs boson in the processes $e^+e^- \rightarrow ZH$. No conclusive signal was found, instead a lower limit on the mass of the

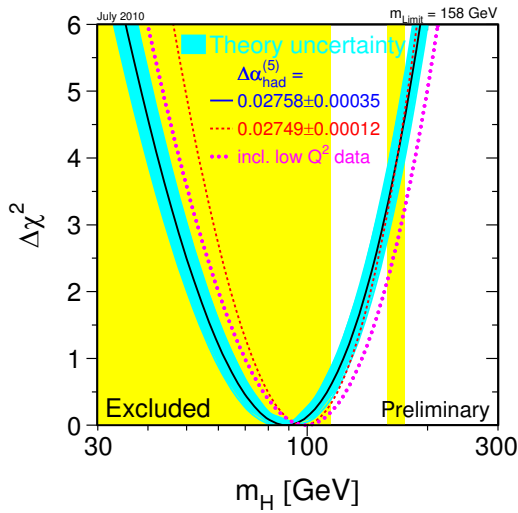


Figure 2.3: $\Delta\chi^2$ vs. m_H curve [21]. The line is the result of the fit using all electroweak data; the band represents an estimate of the theoretical error due to missing higher order corrections. The shaded areas represent the 95% CL exclusion limit on m_H from the direct searches.

Standard Model Higgs boson was placed at [22]:

$$m_H > 114.4 \text{ GeV} \quad \text{at 95\% CL,} \quad (2.28)$$

which is also shown in Figure 2.3. The value for m_H most preferred by the electroweak precision data is already excluded by the direct searches for the Higgs boson.

At the Tevatron proton-antiproton collider currently two experiments, CDF [23] and DØ [24], are taking data. The most important search channels are the associated Higgs production $q\bar{q} \rightarrow VH$ ($V = W^\pm, Z$) with $H \rightarrow b\bar{b}$ and the gluon fusion process $gg \rightarrow H$ with $H \rightarrow W^+W^-$ for low and high Higgs boson masses, respectively. The production cross-sections, relative to the Standard Model one for the tested Higgs boson mass, that can be excluded using the currently analyzed datasets are shown in Figure 2.4.

At the moment the regions of Higgs boson masses excluded at the 95% CL are $100 < m_H < 109 \text{ GeV}$ and $158 < m_H < 175 \text{ GeV}$. The lower mass limit is nearly as high as the LEP limit. With projected improvements, the Tevatron expects to be able to exclude SM Higgs over the entire mass range between 100 and 185 GeV.

2.2 Beyond the Standard Model

Despite its success, the SM is generally believed not to be a final theory but rather an effective theory valid up to a certain energy. Some of the candidates for a theory beyond the Standard Model are Extra Dimensions [26], Little Higgs models [27] or Technicolor [28]. One of the most promising extension, Supersymmetry [29], is presented in more detail in the following Sections.

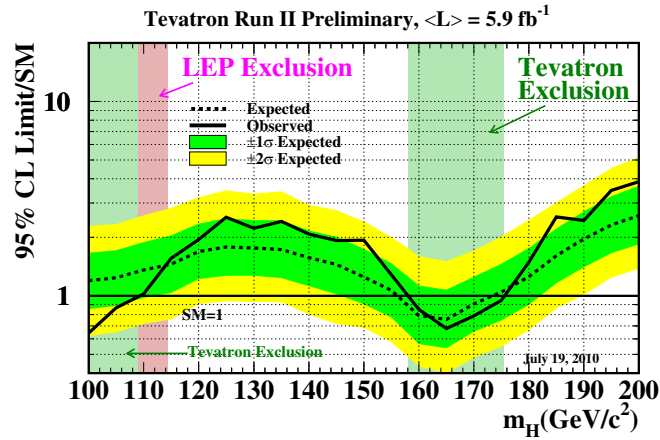


Figure 2.4: Observed and expected 95% CL upper limits on the ratios to the SM cross-section, as functions of the Higgs boson mass for the combined CDF and DØ analysis. The limits are expressed as a multiple of the SM prediction. The bands indicate the 68% and 95% probability regions where the limits can fluctuate, in the absence of signal (from [25]).

2.2.1 Motivation

There are several facts which cannot be derived from the Standard Model, as it would be expected from a final theory, and it faces a number of theoretical problems that could be solved by extending the SM. Some problems are briefly discussed and summarized in the following:

- **Number of free parameters:** Assuming massless neutrinos the Standard Model has at least 19 free parameters; 9 fermion masses, two boson masses (one of the gauge boson masses is not a free parameter as soon as the couplings are defined), three couplings, three quark mixing angles and one CP-violating phase in the CKM matrix [4] and one possible CP violating parameter that occurs in strong interactions and is zero in the Standard Model. If neutrino masses are added as simple Dirac masses seven additional parameters, three masses, three mixing angle, and one CP violating phase, have to be added. Although this is not directly a problem, these are more free parameters than generally expected in a final theory.
- **Three generations:** The Standard Model does not explain why there are three generations of matter particles.
- **Dark Matter and Dark Energy:** Measurements of the Cosmic Microwave Background [14] suggest that only about 4-5% of the matter in the universe is composed of SM particles, i.e. by baryons; neutrinos can only account for at most another few

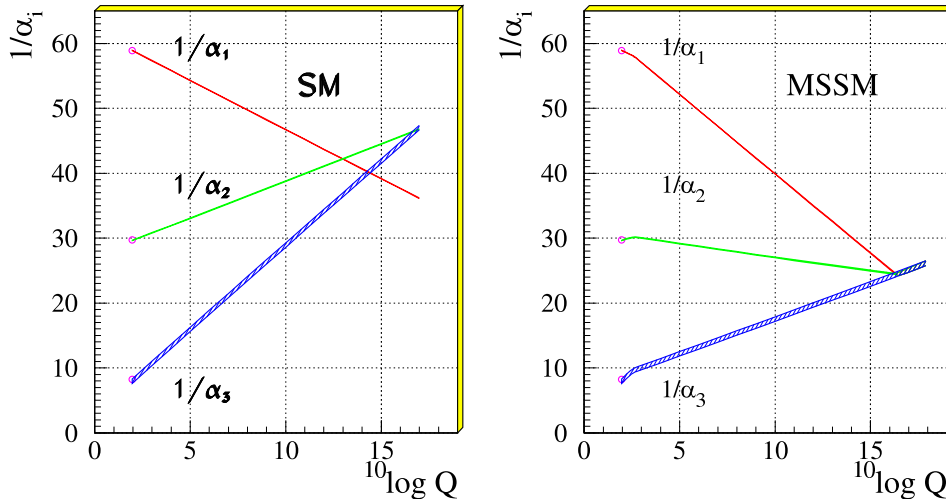


Figure 2.5: Evolution of the inverse of the three coupling constants in the Standard Model (left) and in the supersymmetric extension of the SM like the MSSM (cf. Section 2.2.3) (right). Unification is only obtained in the latter case. The supersymmetric particles are assumed to contribute only above the effective scale of about 1 TeV, which causes a change in the slope in the evolution of couplings (from [30]).

percent. About 23% consists of Dark Matter and 73% of Dark Energy. The SM does not provide appropriate candidates for this phenomena.

- **Gravity:** The gravitational force is not included within the Standard Model. At energies of the order of the Planck mass ($M_{Planck} \approx 10^{19}$ GeV), gravity cannot be neglected anymore and a new theory is necessary.
- **Grand Unification Theories (GUTs):** A unification of the coupling strengths requires an evolution of the couplings with energy to meet at the same point. If only the Standard Model particles enter the evolution equations for the couplings, they come generally close to each other at a scale of about 10^{13-14} GeV, but do not meet. In the supersymmetric extension of the SM like the MSSM (cf. Section 2.2.3) all three couplings unify at an energy of about 10^{16} GeV. This is shown in Figure 2.5.
- **Hierarchy problem:** The Standard Model has very different natural scales in the theory. The electroweak scale is given by the vacuum expectation value $v = 246$ GeV, which is the same order of magnitude as the mass of the weak gauge bosons and the expected mass of the SM Higgs boson. The other natural scale is the Planck scale of 10^{19} GeV. This huge scale difference is completely unexplained within the SM.
- **Fine-tuning problem:** Calculating loop corrections leads to a so-called quadratic divergence of the mass squared of the scalar field. The correction depends on the cut-off scale in the loop diagram and in addition on the spin of the particle which can occur in the loop. The cut-off parameter itself can be motivated by the assumption

that the Standard Model is only an effective theory that is valid up to an energy scale where new physics has to set in and regularize the divergences. This new physics might be at the GUT scale or at the very latest at the Planck scale. Calculating the corrections at those scales leads to a Higgs mass that is several orders of magnitude larger than the expected mass of the Standard Model Higgs boson, which should be at the electroweak scale. This has to be compensated by adjusting the bare mass accordingly in renormalization. As the same divergences reappear in each order of perturbation theory, this fine-tuning is in the order of 10^{-34} [31].

2.2.2 Supersymmetry

There are two kinds of symmetries in the Standard Model: External and internal symmetries. Internal symmetries are symmetries in particle space under transformations of the groups mentioned in the previous Sections such as weak isospin $SU(2)$ or strong color $SU(3)$, each associated with an interaction. External symmetries are symmetries concerning spacetime transformations which are described by the Poincaré group, a generalization of the Lorentz group.

There were many attempts to combine internal with spacetime symmetries in a common group such as $SU(6)$. However, it has been shown by Coleman and Mandula [32] that no non-trivial combination of internal and external symmetries can be achieved. Hence, it is not possible to have a larger spacetime symmetry. Additional internal (local or global) symmetries can only be realized as direct product of these symmetry groups with the Poincaré group. As a consequence, the unification of spin-2 (the graviton, the theoretical gauge boson of the gravitational interaction, must have spin-2) and spin-1 gauge fields within a unique algebra is forbidden.

But the hypothesis of Coleman and Mandula was too restrictive. Their theorem can be evaded but it imposes severe constraints on the possible ways out. It turned out that the only exception is supersymmetry algebra. The Haag-Lopuszanski-Sohnius theorem [33] states that the largest symmetry incorporating an interacting unitary field theory has to be the direct product of Poincaré invariance, gauge symmetry and Supersymmetry (SUSY). In this context, one is tempted to argue that if anything is not illegal it is compulsory, so there “must” exist a physical realizations of Supersymmetry.

SUSY algebra appears as a generalization of Poincaré algebra and links together various representations with different spins. A SUSY transformation Q generates a fermionic state from a bosonic state and vice versa:

$$Q|boson \rangle = |fermion \rangle, \quad Q|fermion \rangle = |boson \rangle \quad (2.29)$$

In a supersymmetric theory, there has to be a fermionic partner particle to each boson with otherwise the same quantum numbers and vice versa. Unfortunately, none of the known fermions can be paired with any of the known bosons because their internal quantum numbers do not match. Hence, the only possibility is the introduction of new supersymmetric partners (spartners) for all Standard Model particles: quark \rightarrow squark, lepton \rightarrow slepton, photon \rightarrow photino, $Z \rightarrow$ Zino, $W \rightarrow$ Wino, gluon \rightarrow gluino, Higgs \rightarrow Higgsino. No supersymmetric partner particles with the same mass as its corresponding

Standard Model particle, e.g. a scalar partner of the electron with a mass of 0.511 MeV, have been observed in nature. Hence, SUSY must be a broken symmetry leading to different masses of the superpartners. In addition, the SUSY breaking scale, M_{SUSY} , should not be too large, i.e. ≤ 1 TeV to avoid fine-tuning.

In addition to aesthetic reasons, SUSY also solves some problems of the SM mentioned in the previous Section. If there were supersymmetric partner particles, they would also lead to corrections to the Higgs boson mass. Due to the spin difference of the superpartners, the quadratic divergences would be canceled exactly in all orders of perturbation theory. This would stabilize the Higgs boson mass and the electroweak scale.

SUSY with sparticle masses at the TeV scale would also lead to a unification of the gauge couplings. The additional supersymmetric partners have to be taken into account in the evolution of the couplings. The result is also shown in the right-hand plots in Figure 2.5 for the case of the minimal extension of the Standard Model to a supersymmetric theory. In this case, the three gauge couplings meet at a scale of the order of 10^{16} GeV.

2.2.3 The Minimal Supersymmetric Standard Model

Several supersymmetric extensions of the Standard Model models exist, with the Minimal Supersymmetric Standard Model (MSSM) being the most economic in terms of the amount of new particles predicted and the number of free parameters. At tree level and with Supersymmetry as an exact symmetry, no additional free parameters for the SUSY sector would be needed. However, as will be explained in the next Section, additional SM parameters are needed for the (SM-)Higgs sector.

Since none of the Standard Model particles can be identified as a superpartner, the particle spectrum is doubled. The particle content of the MSSM is summarized in Table 2.3. The SUSY scalars are named after their fermionic SM partners. Left- and right-handed fermions have different quantum numbers due to their chiral nature. Hence, each Standard Model fermion gets two distinct superpartners (sfermions). The SM gauge bosons (spin-1) have gaugino (spin-1/2) superpartners, named after the gauge eigenstates of their SM partners plus an “ino”-suffix: Bino, Wino and gluino. In addition to the sparticles, it is also necessary to introduce a second Higgs doublet field. Both scalar fields have eight degrees of freedom and as in the Standard Model three are used to generate the gauge boson masses. The leftover five degrees of freedom manifest as five physical Higgs bosons, two charged and three neutral ones. The Higgs sector will be discussed in more detail in Section 2.3.1. Binons and Winos mix with the Higgsino states, the spin-1/2 superpartners of the Higgs bosons. This leads to four neutral (neutralinos) and two charged mass eigenstates (charginos).

In order to conserve baryon and lepton number, a discrete and multiplicative symmetry called R -parity is imposed [34]. It is defined by:

$$R = (-1)^{2s+3B+L}, \quad (2.30)$$

where L and B are the lepton and baryon numbers and s is the spin quantum number.

Standard Model particles		SUSY partners	
Quarks, spin-1/2	$Q_L = \begin{pmatrix} u \\ d \end{pmatrix}_L$ u_R, d_R	Squarks, spin-0	$\tilde{Q}_L = \begin{pmatrix} \tilde{u} \\ \tilde{d} \end{pmatrix}_L$ \tilde{u}_R, \tilde{d}_R
Leptons, spin-1/2	$L_L = \begin{pmatrix} \nu \\ \ell \end{pmatrix}_L$ ℓ_R	Sleptons, spin-0	$\tilde{L}_L = \begin{pmatrix} \tilde{\nu} \\ \tilde{\ell} \end{pmatrix}_L$ $\tilde{\ell}_R$
Photon, spin-1	γ	Photino, spin-1/2	$\tilde{\gamma}$
Gluon, spin-1	g	Gluino, spin-1/2	\tilde{g}
W boson, spin-1	W^\pm	Wino, spin-1/2	\tilde{W}^\pm
Z boson, spin-1	Z	Zino, spin-1/2	\tilde{Z}
Higgs, spin-0	$\begin{pmatrix} H_u^+ \\ H_u^0 \end{pmatrix}, \begin{pmatrix} H_d^0 \\ H_d^- \end{pmatrix}$	Higgsino, spin-1/2	$\begin{pmatrix} \tilde{H}_u^+ \\ \tilde{H}_u^0 \end{pmatrix}, \begin{pmatrix} \tilde{H}_d^0 \\ \tilde{H}_d^- \end{pmatrix}$

Table 2.3: Particle content of the MSSM. The superpartners mix to the mass eigenstates as described in the text. Generation indices for the fermions are suppressed.

The R -parity quantum numbers are $R = +1$ for particles and $R = -1$ for their superpartners. Conservation of R -parity not only forbids baryon and lepton number violation, which would lead e.g. to proton decay, but also has the consequence that supersymmetric particles always have to be produced in pairs. In addition, in their decay products there is always an odd number of SUSY particles and the lightest supersymmetric particle (LSP) remains stable. If this LSP has no electrical nor color charge and is only weak interacting, it would be a suitable Dark matter candidate. However, it must be mentioned that there is no physical principle behind R -parity conservation.

As already mentioned, SUSY must be a broken symmetry. A spontaneously breaking Supersymmetry would require an additional field that acquires a non-zero vacuum expectation value, just as in the case of the Higgs mechanism. But this would spoil gauge invariance. Instead it is supposed that spontaneous supersymmetry breaking takes place via some other fields. The most common model for producing supersymmetry breaking postulates a *hidden sector*. According to this model, there exist two sectors: the usual matter belongs to the *visible* sector, while the second, the *hidden* sector, contains fields which lead to the breaking of supersymmetry. These two sectors interact with each other by exchange of some fields called *messengers*, which mediate SUSY breaking from the hidden to the visible sector. The SUSY breaking scenarios are generally based on how the breaking is mediated to the visible sector. For a more detailed discussion of the hidden sector see Reference [30].

Instead of assuming an explicit breaking mechanism, in the MSSM so-called *soft breaking terms* are added to the Lagrangian, which just parametrize the unknown breaking mechanism. More than hundred new free parameters appear; the masses of the new particles,

phases, mixing parameters, and couplings. Once the SUSY breaking mechanism is fully understood, this number is expected to decrease dramatically. The MSSM Lagrangian including soft breaking terms is given by [29]:

$$\begin{aligned}
 -\mathcal{L}_{\text{soft}}^{\text{MSSM}} &= \frac{1}{2} \left(M_3 \tilde{g} \tilde{g} + M_2 \tilde{W} \tilde{W} + M_1 \tilde{B} \tilde{B} + h.c. \right) \\
 &+ \left(\tilde{u} \mathbf{A}_u \tilde{Q} H_u - \tilde{d} \mathbf{A}_d \tilde{Q} H_d - \tilde{e} \mathbf{A}_e \tilde{L} H_d + h.c. \right) \\
 &+ \tilde{Q}^\dagger \mathbf{m}_Q^2 \tilde{Q} + \tilde{L}^\dagger \mathbf{m}_L^2 \tilde{L} + \tilde{u} \mathbf{m}_u^2 \tilde{u}^\dagger + \tilde{d} \mathbf{m}_d^2 \tilde{d}^\dagger + \tilde{e} \mathbf{m}_e^2 \tilde{e}^\dagger \\
 &+ m_{H_u}^2 H_u^* H_u + m_{H_d}^2 H_d^* H_d + (B\mu H_u H_d + h.c.) , \tag{2.31}
 \end{aligned}$$

with the gluino, Wino and Bino mass terms M_3 , M_2 and M_1 in the first line. The terms in the second line contain trilinear couplings between sfermions and Higgs bosons and the third line describes slepton and squark mass terms. The last line contains the supersymmetric contributions to the Higgs potential. The MSSM Lagrangian in Eq. 2.31 contains in total 105 new parameters in addition to the Standard Model parameters.

Since it is not possible to examine the whole SUSY parameter space, the number of parameters are commonly reduced by making some assumptions reasonably justified to constrain the MSSM [35]. These assumptions are:

- The masses of the gauge fermions are assumed to be real and the same at the GUT scale:

$$M_1(\Lambda_{\text{GUT}}) = M_2(\Lambda_{\text{GUT}}) = M_3(\Lambda_{\text{GUT}}) = m_{1/2} , \tag{2.32}$$

where $m_{1/2}$ is the common mass. This corresponds to the unification of the gauge couplings at Λ_{GUT} .

- It is assumed that the scalar fermion masses and the trilinear couplings are diagonal, real and universal for all three generations at the GUT scale. The common sfermion masses and trilinear couplings are called m_0 and A_0 . These assumptions reduce large effects beyond the Standard Model that would be present at tree-level, such as flavor changing neutral currents or additional CP violation, which are strongly limited by flavor observables.
- The Higgs mass parameters are assumed to be real at the GUT scale.

This reduces the number of additional parameters to five: m_0 , $m_{1/2}$, A_0 , $\tan\beta$ and $\text{sign}(\mu)$. Commonly the MSSM is only studied in this constrained form. The low energy MSSM parameters can be derived by the renormalization group equations. A detailed discussion can be found in Reference [35].

2.3 The charged Higgs boson

Charged Higgs bosons are predicted in many non-minimal Higgs scenarios. The most important examples are Two-Higgs-Doublet Models (2HDM), as ad-hoc extension to the SM

as well as in the context of SUSY and models with Higgs triplets, including Little Higgs models [27]. The discovery of a charged Higgs boson would be a definite signal for the existence of New Physics beyond the Standard Model and possibly one of the first experimental evidences to be found if the Minimal Supersymmetric Standard Model is realized in nature.

The following Sections will give a short review of general Two-Higgs-Doublet Models. The Higgs sector of the MSSM and in particular the properties of charged Higgs bosons within this context will be presented and discussed.

2.3.1 The Two-Higgs-Doublet Model

The strongest motivation for charged Higgs boson searches is that SUSY requires at least two Higgs doublets and thus charged Higgs bosons. There are two reasons for this requirement. In the SM, Yukawa interactions involving the Higgs field ϕ (cf. Eq. 2.15) give masses to the $T_W^3 = -1/2$ components of the fermion doublets when ϕ^0 acquires a vacuum expectation value, while the corresponding interactions with the charged conjugated field ϕ^c give masses to the $T_W^3 = +1/2$ components (cf. Eq. 2.26). But in the supersymmetric version such right-handed chiral superfields are not allowed since they would spoil gauge invariance [36]. Hence, a second Higgs doublet is needed to give mass to the $T_W^3 = +1/2$ fermions. In addition, the second doublet solves another problem. The superpartners of the Higgs field, the Higgsinos, would lead to the appearance of chiral anomalies which would spoil the gauge invariance. These anomalies are canceled by the Higgsinos from the second doublet.

A Two-Higgs-Doublet Model is favored by (but not limited to) Supersymmetry as it is the minimal necessary extension of the SUSY Higgs sector. The Higgs mechanism works similarly to the case with one scalar doublet as shown in Section 2.1.3 and is only presented schematically here.

The Higgs field is introduced by two $SU(2)_W$ doublet scalar fields ϕ_1 and ϕ_2 with hypercharge $Y = 1$. The most general 2HDM Higgs potential which is gauge invariant, renormalizable, CP invariant and ensures small Flavor Changing Neutral Currents (FCNC) [36] depends on six real parameters λ_i and is given by:

$$\begin{aligned}
 V(\phi_1, \phi_2) &= \lambda_1 \left(\phi_1^\dagger \phi_1 - v_1^2 \right)^2 + \lambda_2 \left(\phi_2^\dagger \phi_2 - v_2^2 \right)^2 \\
 &+ \lambda_3 \left[\left(\phi_1^\dagger \phi_1 - v_1^2 \right) + \left(\phi_2^\dagger \phi_2 - v_2^2 \right) \right]^2 \\
 &+ \lambda_4 \left[\left(\phi_1^\dagger \phi_1 \right) \left(\phi_2^\dagger \phi_2 \right) - \left(\phi_1^\dagger \phi_2 \right) \left(\phi_2^\dagger \phi_1 \right) \right] \\
 &+ \lambda_5 \left[\text{Re}(\phi_1^\dagger \phi_2) \right]^2 + \lambda_6 \left[\text{Im}(\phi_1^\dagger \phi_2) \right]^2 .
 \end{aligned} \tag{2.33}$$

If all parameters λ_i are positive, then the minimum of the potential is given by the vac-

uum expectation values v_1 and v_2 of the Higgs doublets,

$$\phi_1^0 = \begin{pmatrix} 0 \\ v_1 \end{pmatrix}, \quad \phi_2^0 = \begin{pmatrix} 0 \\ v_2 \end{pmatrix}, \quad (2.34)$$

and breaking $SU(2)_W \otimes U(1)_Y$ down to $U(1)_{em}$ as desired. One of the key parameters of the model is the ratio of the vacuum expectation values

$$\tan\beta = v_2/v_1. \quad (2.35)$$

This general 2HDM model has eight degrees of freedom, three of them give masses to the electroweak gauge bosons just like in the case of one Higgs doublet. This leaves five physical Higgs bosons: a charged pair (H^\pm)²; two neutral CP -even scalars (H and h) and a neutral CP -odd scalar (A). In contrast to the one Higgs doublet model with one free parameter, the Higgs boson mass, the number of free parameters increased to 6: four Higgs masses, $\tan\beta$ and a Higgs mixing angle α , the mixing angle between the two CP -even neutral Higgs states. The vacuum expectation values satisfy $v_1^2 + v_2^2 = v^2 = (246 \text{ GeV})^2$ are thus related to the mass of the weak gauge bosons.

In such a general 2HDM, the Yukawa interactions can be built in four different and independent ways that are free from FCNCs. The so-called Type II of 2HDM is that where ϕ_2 couples to up-type quarks and ϕ_1 couples to down-type quarks and leptons [37]. The relevant part in the Type II Lagrangian describing the H^+tb Yukawa coupling is given by [38]:

$$\bar{t}bH^+ : \frac{g}{\sqrt{2}M_W} V_{tb} [\tan\beta m_b \bar{t}b_R + \cot\beta m_t \bar{t}b_L], \quad (2.36)$$

where $V_{tb} \approx 1$ is the CKM Matrix element. This coupling and hence the production and decay mode of charged Higgs bosons involving top and bottom quarks strongly depends on the value of $\tan\beta$. This is discussed in more detail in Section 2.3.3.

Regarding the Higgs sector, the MSSM is an example of a Type II Higgs Doublet Model. In order to use the results of such a 2HDM one has to be careful with the notation. In SUSY two Higgs doublet fields with opposite hypercharge, H_1 with $Y = -1$ and H_2 with $Y = 1$, are needed. The relation between those fields and ϕ_i are:

$$(\phi_1)^j = \varepsilon_{ij} H_1^{i*}, \quad (\phi_2)^j = H_2^j, \quad (2.37)$$

where i, j are $SU(2)$ indices and $\varepsilon_{12} = -\varepsilon_{21} = 1$, $\varepsilon_{11} = \varepsilon_{22} = 0$.

In addition, Supersymmetry imposes strong constraints on the 2HDM parameters. SUSY enforces relations amongst Higgs masses and couplings, on the one hand, and weak gauge boson masses and interaction parameters, on the other hand, in such a way that, of the original 6 independent parameters, only two survive as such in the MSSM. Hence, the complete Higgs sector at tree level is defined by only two parameters, which can for example be chosen as $\tan\beta$ and a mass scale, usually the mass of one of the physical Higgs bosons.

²In the following, the charged Higgs boson will be denoted with H^+ , but H^- and charge conjugate processes are always implicitly included

2.3.2 Constraints in the MSSM

The $\bar{t}bH^+$ Yukawa coupling given in Eq. 2.36 can be ultraviolet divergent. This means that the theory would not be perturbatively well-defined at high energies. Requiring it to remain perturbative up to the GUT scale implies

$$1 < \tan\beta < m_t/m_b(\sim 50) . \quad (2.38)$$

However, this assumes the absence of any new physics beyond the MSSM up to the GUT scale, i.e. the so-called desert scenario. Without this assumption one gets weaker limits from the perturbative bounds on this coupling at the electroweak scale [39] leading to

$$0.3 < \tan\beta < 200 . \quad (2.39)$$

In addition, it is a common belief that SUSY models, as long as the Higgs sector is not enlarged, are unnatural if $\tan\beta$ is large [40]. This means that at least one fine tuning in the order of $1/\tan\beta$ of the parameters of the Higgs potential would be necessary to achieve electroweak symmetry breaking. In Reference [41] it is discussed that this conclusion is only based on tree level analysis and that the same conclusion does not follow once radiative corrections are included. Hence, SUSY models are not unnatural in the technical sense even if the parameter $\tan\beta$ is large.

The Higgs potential given in Eq. 2.33 together with the MSSM constraints on the parameters yields the following set of relations for the masses at tree level:

$$m_{h,H}^2 = \frac{1}{2} \left(m_A^2 + m_Z^2 \pm \sqrt{(m_A^2 + m_Z^2)^2 - 4m_A^2 m_Z^2 \cos^2 2\beta} \right) , \quad (2.40)$$

$$m_{H^+}^2 = m_A^2 + m_W^2 . \quad (2.41)$$

This leads to the SUSY mass relations:

$$\begin{aligned} m_{H^+} &\geq m_W \\ m_h &\leq m_A \leq m_H \\ m_h &\leq m_Z \\ m_h^2 + m_H^2 &= m_A^2 + m_Z^2 \end{aligned} \quad (2.42)$$

At tree level the Higgs sector in the MSSM is completely defined by only two parameters usually chosen to be the mass of the pseudoscalar or charged Higgs boson (A_0 or H^+) and $\tan\beta$. However, at loop level there are additional contributions from a large number of MSSM parameters. In order to still be able to present results in two-dimensional planes, benchmark scenarios are used. They define all relevant parameters except for $\tan\beta$ and m_{H^+} (or m_A). They are chosen to have different impact especially on the Higgs sector. The most frequently used scenario is called m_h -max [42] and is used in this analysis. This scenario has been proposed already in [43] and has been chosen to maximize the mass of the lightest Higgs boson for a given m_A and $\tan\beta$ leading to the smallest excluded parameter region from the LEP experiments.

The m_h -max scenario can be described by the following set of parameters:

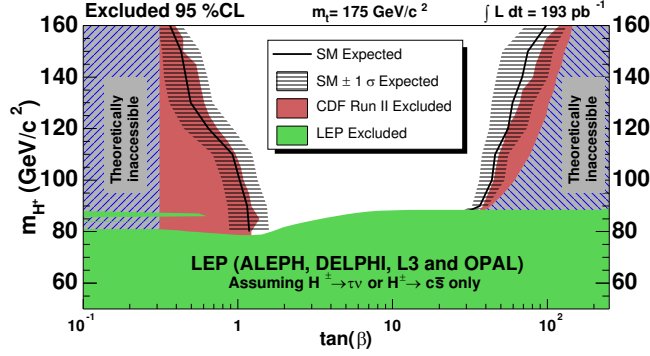


Figure 2.6: Charged Higgs boson exclusion limits from direct searches. Results from the LEP and the CDF Experiment [45, 48] for the m_h -max scenario.

- $M_{SUSY} = 1000$ GeV, the sfermion mass parameter at the electroweak scale
- $\mu = 200$ GeV, the Higgs-Higgsino mass parameter
- $X_t = 2000$ GeV, where $A_t = X_t + \mu/\tan\beta$ is a third generation trilinear coupling
- $M_2 = 200$ GeV, the Wino mass parameter at the electroweak scale
- $M_3 = 800$ GeV, the Gluino mass parameter at the electroweak scale

At tree level, the mass of the lightest Higgs boson h appears to be lower than the Z boson mass (cf. Eq. 2.42). If higher order contributions are included, the upper bound on its mass is expected to be around $m_h < 135$ GeV (m_h -max scenario). The other Higgs bosons are almost degenerate in mass if they are heavier than a few hundred GeV. The lower theoretical limit on the H and H^+ masses is given by the Z and W boson masses, see Eq. 2.40 and 2.41 and is thus similar to the experimental lower limit $m_{H^+} > 79.3$ GeV from the LEP experiments [44]. For low and high $\tan\beta$, a charged Higgs boson mass of less than about 160 GeV is excluded by the CDF and $D\bar{O}$ experiments [45–47]. The exclusion limits from direct searches for the m_h -max scenario are shown in Figure 2.6.

Exclusion limits can also be obtained indirectly, for example from observing meson decays which can be mediated by charged Higgs bosons: $B \rightarrow \tau\nu$, $B \rightarrow X_s\gamma$, $B \rightarrow \mu^+\mu^-$, $K \rightarrow \mu\nu$ or by measuring $g-2$, the anomalous magnetic moment of the muon [49]. The current indirect exclusion limits are shown in Figure 2.7 for a Non-Universal Higgs mass scenario. This model generalizes the constraint MSSM [50], where several parameters obey a set of boundary conditions at the Unification scale (cf. Section 2.2.3), allowing for the GUT scale mass parameters of the Higgs doublets to have different values, i.e. $m_{H_u} \neq m_{H_d}$. These two additional parameters can be traded for two other parameters at a lower scale, conveniently the μ parameter and the mass m_A of the CP-odd Higgs boson. The tree level mass relation given in Eq. 2.41 then implies that the charged Higgs boson mass can be treated essentially as a free parameter, an important difference comparing to the constraint MSSM. The allowed points in the $(m_{H^+}, \tan\beta)$ parameter space fall in a

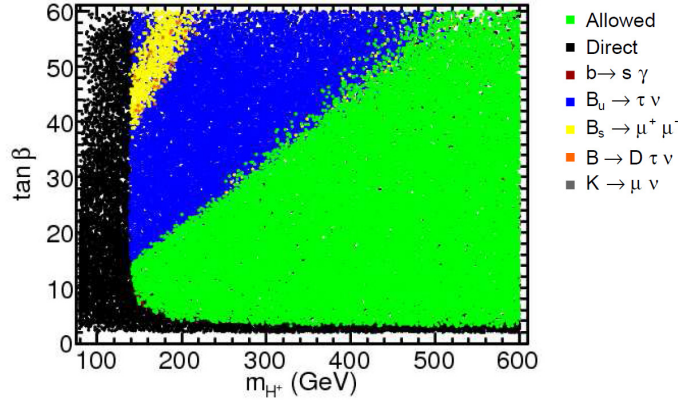


Figure 2.7: Charged Higgs boson exclusion from B physics and other constraints for a Non-Universal Higgs mass scenario [49]. The allowed points in the $(m_{H^+}, \tan\beta)$ plane are marked in green.

distinct region, forming a triangular shape. Within this model, charged Higgs masses down to $m_{H^+} \simeq 135$ GeV can be accommodated, with the lowest masses allowed for intermediate $\tan\beta \sim 7$ -15.

But it must be mentioned that the exclusion limits from indirect searches are very model-dependent. E.g. a limit on the charged Higgs boson mass $m_{H^+} > 316$ GeV at 95% CL is obtained irrespective of the value of $\tan\beta$ [51]. This exclusion limit only considers a general Type II 2HDM with no further extension to the SM. Such indirect searches are very sensitive to New Physics due to loop contribution of new particles. Hence, the obtained limit will change e.g. in supersymmetric extensions of the Standard Model.

Equation 2.41 together with the experimental constraint $m_A > 93.4$ GeV [52] translates into another indirect limit: $m_{H^+} > 123$ GeV.

2.3.3 Production and decay modes of charged Higgs bosons

The search strategies for charged Higgs bosons depend on the charged Higgs boson mass, m_{H^+} , which dictates both the production and the available decay modes.

If the charged Higgs boson mass satisfies $m_{H^+} < m_t - m_b$ (light charged Higgs boson), where m_b and m_t are the bottom and top quark mass, respectively, H^+ particles could be produced in the decays of on-shell top quarks, $t \rightarrow bH^+$. At the LHC, such light charged Higgs bosons will be dominantly produced through the process $q\bar{q}, gg \rightarrow t\bar{t} \rightarrow bH^+\bar{t}$, as depicted in Figure 2.8. Here, the top quarks have been produced in gg fusion or $q\bar{q}$ annihilation. Below the top quark mass, the charged Higgs boson predominantly decays into a τ lepton and a neutrino. For values of $\tan\beta \gtrsim 3$ this branching ratio is close to 100%, as shown in Figure 2.9. Decay modes involving $c\bar{s}$ or W^+h are also present, but depending on the value of $\tan\beta$ the branching ratios are at least one or two orders of magnitude smaller than for the $\tau^+\nu$ mode.

Above the top quark mass (heavy charged Higgs) the main contribution to the charged Higgs boson production is through the so-called twin processes, $gg \rightarrow bH^+\bar{t}$ and $g\bar{b} \rightarrow H^+\bar{t}$.

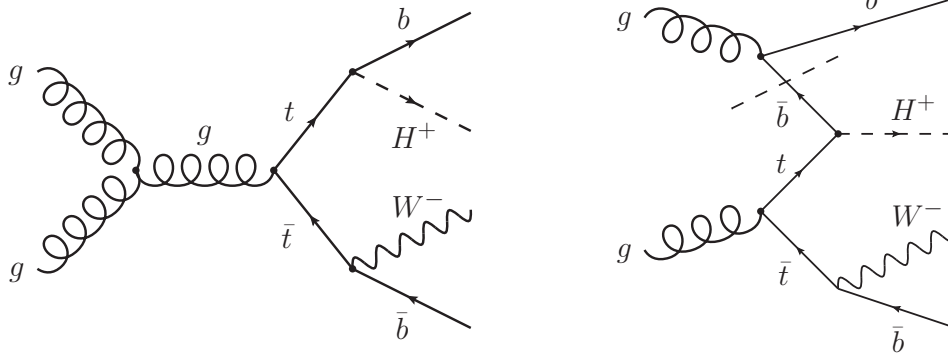


Figure 2.8: Feynman diagrams showing the dominant production mode for light charged Higgs bosons via $gg \rightarrow t\bar{t} \rightarrow bH^+\bar{t}$ (left) and the two production modes for heavy charged Higgs bosons (right). The dashed line indicates where the factorization between the parton densities and the hard scattering is performed, leading either to the $gg \rightarrow bH^+\bar{t}$ process (when starting on the left) or to the $g\bar{b} \rightarrow H^+\bar{t}$ process (when starting on the dashed line).

The reason for calling them twin processes is simply that they describe the same basic process but using different approximations as shown in Figure 2.8. The first process enters in the next-to-leading order (NLO) calculation of the latter one and thus cannot be added trivially as this would lead to double counting. Further details about these two contributions can be found in Reference [54]. Above the top quark mass threshold, the branching fraction of the $t\bar{b}$ decay mode shows a rapid growth and soon becomes the dominant decay mode as shown in Figure 2.9. This decay mode is the subject of this analysis. Contrary to the light charged Higgs boson, which almost exclusively decays into $\tau^+\nu$, the heavy charged Higgs boson does not solely decay into $t\bar{b}$, but a significant fraction is allowed to decay into other decay channels like $\tau^+\nu$, W^+h , $c\bar{s}$ and SUSY particles, where kinematically allowed. The branching ratios of the H^+ decays are calculated using FeynHiggs 2.6.5 [55].

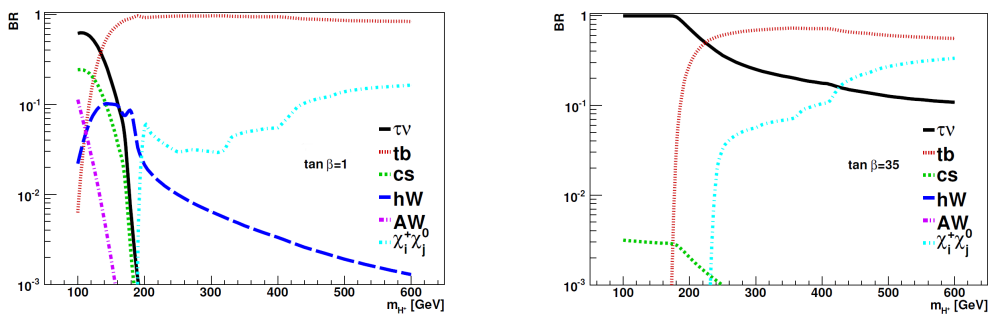


Figure 2.9: Charged Higgs boson branching ratios as a function of m_{H^+} for two different values of $\tan\beta$ for the m_h -max scenario. Left: $\tan\beta = 1$, Right: $\tan\beta = 35$ (from [53]).

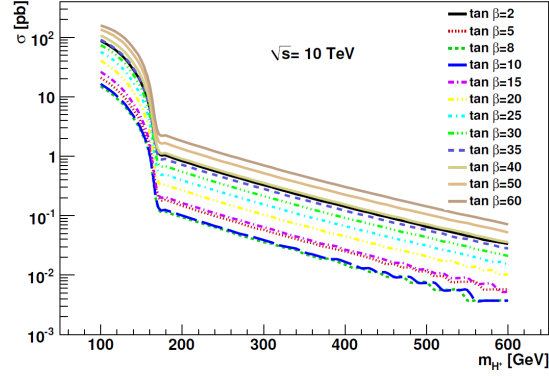


Figure 2.10: Charged Higgs boson production cross-section as a function of m_{H^+} for various values of $\tan\beta$ for the m_h -max scenario. Charge conjugate processes are included (from [53]).

The charged Higgs boson production cross-section at NLO precision [56] is shown in Figure 2.10 for the m_h -max scenario. A change in the behavior around the top quark mass is clearly visible. Here, both contributions ($gg \rightarrow t\bar{t} \rightarrow bH^+\bar{t}$ and $g\bar{b}/gg \rightarrow [b]H^+\bar{t}$) are of similar size. The cross-section falls off quickly with increasing m_{H^+} and it is enhanced at small and large values of $\tan\beta$. The relevant part of the MSSM Lagrangian describing the $H^+\bar{t}b$ coupling is given by Eq. 2.36, which has a minimum at $\tan\beta \approx \sqrt{m_t/m_b}$. This behavior is illustrated in Figure 2.11 showing production cross-section times branching ratio (BR) for the process $H^+ \rightarrow t\bar{b}$ as a function of $\tan\beta$. The dip around $\tan\beta \approx 7$ is apparent.

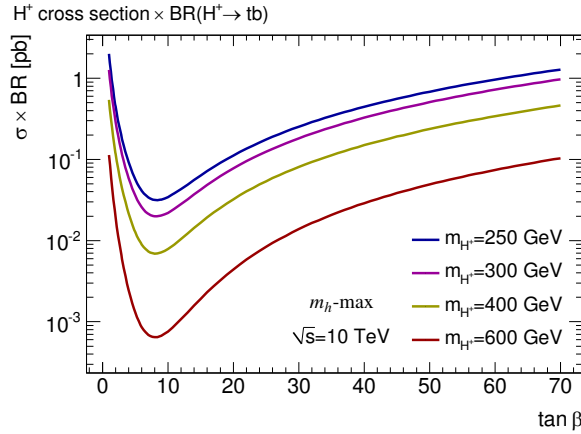


Figure 2.11: Charged Higgs boson production cross-section times branching ratio $\text{BR}(H^+ \rightarrow t\bar{b})$ as a function of $\tan\beta$ for various values of m_{H^+} for the m_h -max scenario (from [53]). For values of $\tan\beta > 70$ the production cross-section is extrapolated with a quadratic fit.

3 The ATLAS experiment at the Large Hadron Collider

3.1 Introduction

Since its prediction in 1964, the Higgs boson has become one of the holy grails in particle physics. Physicists have been eagerly striving for its discovery for several decades at particle accelerators like the Tevatron at Fermilab and the Large Electron Positron (LEP) collider at CERN. While the former is still in operation, LEP was decommissioned in the year 2000 after eleven years of data taking in order to allow for the construction of its successor, the Large Hadron Collider (LHC) [57] which is depicted in Figure 3.1. For LEP as electron-positron collider, the attainable center-of-mass energy was limited by synchrotron radiation accompanying circulating charged particles. Since for accelerated particles of mass m the total radiated power is proportional to $1/m^4$, this limitation can be overcome by accelerating heavier particles than electrons. At the Tevatron protons and antiprotons are brought into collision at a center-of-mass energy of 1.96 TeV. In comparison to protons, the production and acceleration of a large number of antiprotons is technically much more demanding. Therefore, at the LHC two counter-rotating beams of protons are accelerated up to energies of 7 TeV providing a yet unrivaled center-of-mass energy of 14 TeV. Superconducting dipole magnets, providing a magnetic field strength of 8.33 T, are employed to keep the proton beams on the circular track of 26.7 km circumference in the former LEP tunnel.

Four different experiments are installed at the four interaction points covering a broad range of experimental studies. The two general-purpose detectors, ATLAS (A Toroidal LHC Apparatus) [58] and CMS (Compact Muon Solenoid) [59] will provide information on long anticipated new phenomena and precision measurements of Standard Model processes. The LHCb (Large Hadron Collider beauty) experiment [60] is designed to study B -meson physics and to explore CP-violation in B decays at high precision. In addition to protons, the LHC will also accelerate and collide heavy ions. ALICE (A Large Ion Collider Experiment) [61] is dedicated to the study of heavy ion collisions and of the quark-gluon plasma, a state consisting of free quarks and gluons.

During commissioning (without beam) of the LHC sectors at high current for operation at 5 TeV, an incident occurred in September 2008. The cause was a faulty electrical connection between two of the accelerator's magnets. This resulted in mechanical damage and release of helium from the magnet cold mass into the tunnel. Due to the delay caused by this incident, the collider was not operational until November 2009. Investigations of the problem showed that the LHC can not provide 7 TeV proton beams without a major repair but rather 5 TeV beams. As by this reason, this analysis is carried out for a center-of-mass energy of $\sqrt{s} = 10$ TeV. However, at the beginning of 2010 it was decided that an operation at this energy is not safe enough not to risk another incident which would spoil the LHC program for a long time. In the end, the decision was to operate the LHC at 3.5 TeV beam energy ($\sqrt{s} = 7$ TeV), 3.5 times that of the Tevatron and accumulate a substantial amount

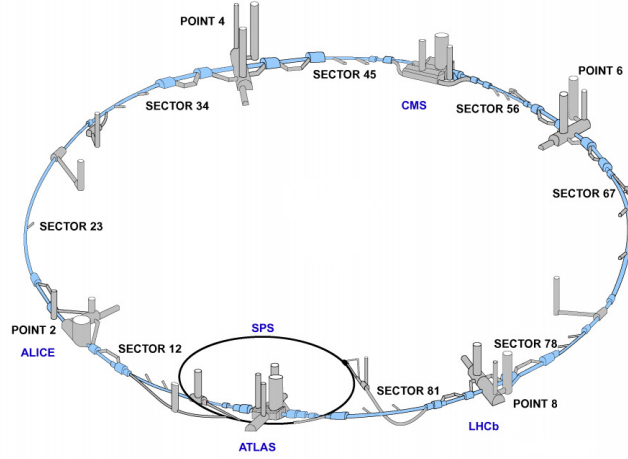


Figure 3.1: Schematic layout of the LHC at CERN.

of data of 1 fb^{-1} or stop by the end of 2011. After a 1-1.5 year shutdown in 2012 to repair the rest of the machine and to make other preparations, the LHC will attempt to reach its design energy of $\sqrt{s} = 14 \text{ TeV}$.

During the startup phase, the LHC will operate only at a center-of-mass energy of $\sqrt{s} = 7 \text{ TeV}$ to allow for safe commissioning of the accelerator. Subsequently, the center-of-mass energy will be increased up to the design value of $\sqrt{s} = 14 \text{ TeV}$. At the beginning, the LHC will also operate at relatively low instantaneous luminosities of $\mathcal{L} = 10^{30} - 10^{32} \text{ cm}^{-2}\text{s}^{-1}$, with the luminosity being defined by beam parameters such as the number of particles per bunch, N_b , the number of bunches per beam, n_b , and the revolution frequency, f_{rev} , as $\mathcal{L} \propto N_b^2 n_b f_{rev}$. The number of events per second generated in the LHC collisions is given by:

$$N_{event} = \mathcal{L} \cdot \sigma_{event}(\sqrt{s}), \quad (3.1)$$

where σ_{event} is the cross-section of the physics process under study at the proton-proton center-of-mass energy \sqrt{s} . After this initial phase, the luminosity will first be increased to $\mathcal{L} = 10^{33} \text{ cm}^{-2}\text{s}^{-1}$ before the LHC will finally reach its design luminosity of $10^{34} \text{ cm}^{-2}\text{s}^{-1}$ corresponding to an integrated luminosity of approximately 100 fb^{-1} per year. To achieve the design luminosity, 2835 bunches of 10^{11} protons are accelerated in each direction leading to bunch crossings every 25 ns at the interaction points. In this case, on average 23 inelastic proton-proton collisions will take place at each bunch crossing. Hence, each selected physics event will be overlaid on average by 22 so-called pile-up events. This high interaction rate and the therefore very high particle production rate impose an unprecedented technical challenge on all the experiments.

3.2 The ATLAS detector

ATLAS is one of the two general-purpose detectors at the LHC designed to study a broad spectrum of physics processes. The detector design is largely driven by an optimal discovery potential for the Higgs boson. However, proton-proton collisions at the LHC allow for the exploration of various other Standard Model processes and, furthermore, of phenomena beyond the Standard Model. The most important physics goals are briefly summarized in the following:

- **Precision measurements:** Already at low integrated luminosities, precise measurements of the W and Z boson masses and production cross-sections are possible and allow for the calibration and for performance measurements of all detector components.
- **Top physics:** The top quark has been discovered by the experiments at the Tevatron in 1995 [62, 63]. The expected top quark production cross-section at the LHC surpasses the one at Tevatron by two orders of magnitude allowing for very precise measurements of its properties like mass, production cross-section and decay branching ratios.
- **Higgs physics:** The LHC experiments provide access to a mass range up to 1 TeV for searches for the Higgs boson in the Standard Model and beyond and will therefore provide insight into the question of the origin of the particle masses.
- **Supersymmetry:** Supersymmetry (SUSY) [29] is an extensively studied extension of the Standard Model which has not been observed yet experimentally. Discovery of SUSY is already possible with an integrated luminosity of 1 fb^{-1} for favorable combinations of model parameters [64], because of relatively large production cross-sections and the clear signature of large missing energy in the detector due to the lightest supersymmetric particle (LSP), which is stable and weakly interacting, escaping detection.
- **Beyond the Standard Model:** Besides Supersymmetry, signatures of various other new physics processes beyond the Standard Model will be searched for by the LHC experiments. New phenomena discoverable by ATLAS are, for instance, new heavy gauge bosons W' and Z' with masses up to $\sim 6 \text{ TeV}$, rare decays of heavy quarks and leptons as well as mini black holes and other consequences of extra spatial dimensions.

Figure 3.2 shows the production cross-sections of the most important Standard Model processes. The search for rare processes with very low cross-sections such as the Higgs boson production or processes predicted by theories beyond the Standard Model is hampered by several orders of magnitude by more frequent processes such as b and top quark, QCD jet or W and Z boson production. While being interesting subjects of high precision Standard Model measurements themselves, these processes constitute large backgrounds to the search for rare processes.

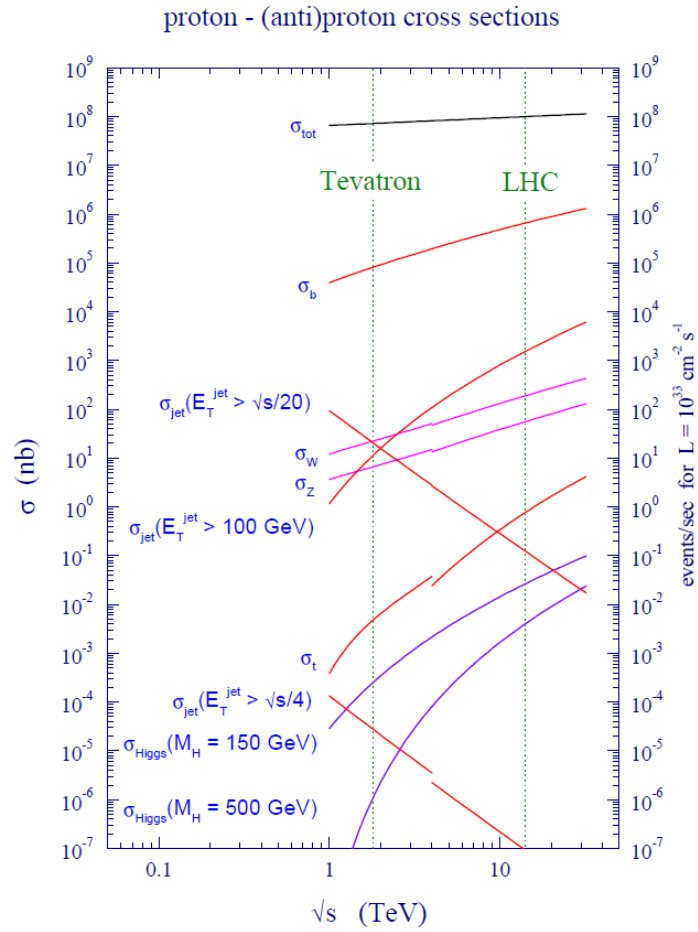


Figure 3.2: Production cross-sections and event rates for the dominant processes in proton-(anti)proton collisions as a function of the center-of-mass energy \sqrt{s} at a luminosity of $10^{33} \text{ cm}^{-2} \text{ s}^{-1}$ [65]. The discontinuities in the curves at $\sqrt{s} = 4 \text{ TeV}$ are due to the different colliding particles: $p\bar{p}$ at the Tevatron and pp at the LHC.

The high particle rates at the LHC are very demanding for the detector design and construction requiring fast and radiation-hard detector technologies and electronics, very precise tracking and momentum measurement, large calorimeter coverage with precise jet and missing transverse energy measurement as well as a very selective trigger system which has to provide strong reduction of the event rate while efficiently selecting interesting physics events.

A schematic view of the ATLAS detector is shown in Figure 3.3. It consists of three major subsystems which are arranged cylindrically around the beam pipe. Based on References [58, 66], they will be described in more detail in the following Sections. From the in- to the outside the main detector systems provide:

- **Inner detector (ID):** Tracking as well as momentum and charge measurement of

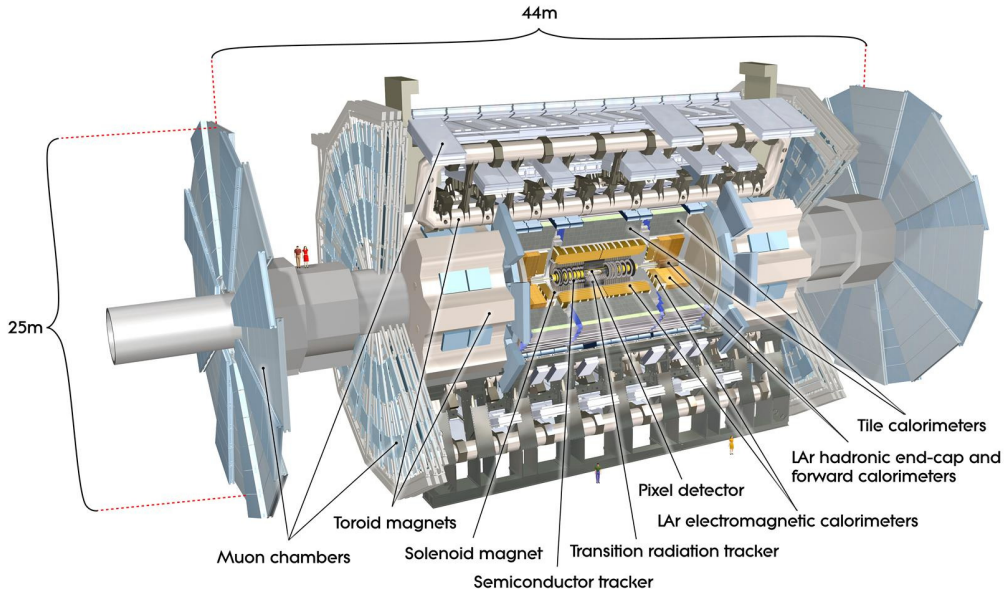


Figure 3.3: Cut-away view of the ATLAS detector [58]. The dimensions of the detector are 25 m in height and 44 m in length. The overall weight of the detector is approximately 7000 tonnes.

charged particles,

- **Calorimeter system (CS):** Identification and energy measurement of electrons, photons and hadron jets,
- **Muon spectrometer (MS):** Identification, tracking as well as stand-alone momentum and charge measurement of muons.

Each subdetector consists of three parts: a cylindrically shaped barrel part and two end-caps enclosing the barrel on both sides.

3.2.1 The coordinate system

The origin of the ATLAS coordinate system is located at the nominal interaction point. The x -axis points from the origin towards the center of the LHC ring while the y -axis points upwards. The z -axis is pointing along the beam axis with the orientation chosen such that the coordinate system is right-handed. The A-side of the detector is defined as the hemisphere with $z > 0$ whereas $z < 0$ defines the C-side.

The azimuthal angle ϕ is the angle in the x - y plane with respect to the positive x -axis whereas the polar angle θ is defined with respect to the positive z -axis. An important variable in high-energy physics at hadron colliders is the so-called rapidity:

$$y = \frac{1}{2} \ln \left(\frac{E - p_z}{E + p_z} \right), \quad (3.2)$$

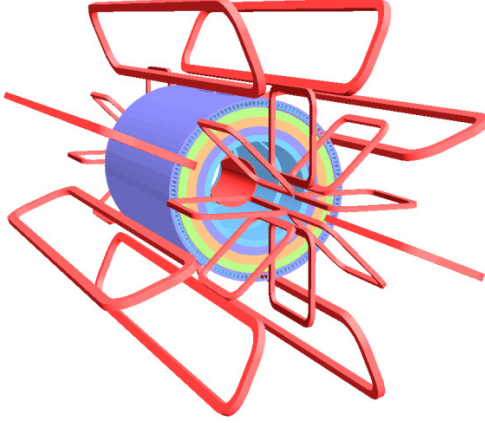


Figure 3.4: Sketch of the ATLAS magnet system with the central solenoid and the three toroids [58].

which is invariant under Lorentz transformations along the z -axis. In the limit of small masses it simplifies to the frequently used pseudo-rapidity:

$$\eta = -\ln\left(\tan\left(\frac{\theta}{2}\right)\right). \quad (3.3)$$

ϕ and η are the commonly used coordinates for physics objects in ATLAS with the distance ΔR in the η - ϕ -space defined as:

$$\Delta R = \sqrt{\Delta\eta^2 + \Delta\phi^2}. \quad (3.4)$$

In proton-proton collisions, the momentum of the incoming partons is unknown. The momentum components in x - and y -direction can, however, be assumed to be zero. Hence, the center-of-mass system of the interaction is not known and quantities defined in the transverse plane to the z -axis, are of particular importance. Transverse variables used throughout this work are for instance, the transverse momentum p_T , the transverse energy E_T and the missing transverse energy E_T^{miss} .

The helical tracks of charged particles in the uniform magnetic field of the inner detector can be described by five parameters. They can be chosen e.g. p_T - the transverse momentum w.r.t. the beam axis, d_0 - the point of closest approach of the track trajectory in the transverse plane to the beam axis, the so-called transverse impact parameter (IP), $\phi_0 = \tan^{-1}(p_y/p_x)$ at the transverse IP, $\cot\theta = p_z/p_T$ and z_0 - the z position of the transverse IP.

3.2.2 The magnet system

The magnetic field, essential to measure particle momenta, is provided by a superconducting magnet system shown in Figure 3.4.

The inner tracking detector is surrounded by the central superconducting solenoid which is operated at a temperature of 4.5 K and generates a 2 T solenoidal magnetic field at a nominal operating current of approximately 7.7 kA. The solenoid coil extends 5.8 m in length and 2.6 m in diameter. Since it is placed between the tracking detector and the electromagnetic calorimeter, the design of the central solenoid has to minimize the amount

of material in order to allow for a precise energy measurement of particles reaching the calorimeter. Therefore, the solenoid shares one vacuum vessel with the electromagnetic calorimeter exploiting its iron absorbers as return yoke for the magnetic field.

The magnetic field for the muon spectrometer is provided by three large air-core toroid magnets that are 25 m long in the barrel and 5 m long in the two end-caps. Each of them consists of eight coils arranged symmetrically around the beam axis. The two end-cap toroids are placed in the forward regions of the detector inside the barrel toroid. While for each of the end-cap toroids all eight magnet coils are housed in the same vacuum vessel, each of the barrel toroid coils is housed in an individual cryostat. All three toroids are operated at a nominal current of 20.5 kA. The barrel toroid provides a magnetic field strength between 0.2 T and 2.5 T in the region $|\eta| < 1.4$ whereas the end-cap toroids provide a field of 0.2 - 3.5 T in the region $1.6 < |\eta| < 1.7$. In the transition region $1.4 < |\eta| < 1.6$ where the magnetic fields overlap, the field strength is lower. An air core magnet system has been chosen in order to minimize material the muons have to traverse and hence the multiple scattering which deteriorates the muon momentum resolution.

3.2.3 The inner detector

At the LHC design luminosity of $10^{34} \text{ cm}^{-2}\text{s}^{-1}$, every 25 ns approximately 1000 tracks will emerge from the collision point within $|\eta| < 2.5$ creating a large track density in the detector. The inner detector (ID) is a fast and highly granular tracking detector designed to reconstruct the tracks of charged particles. Since it is situated inside the solenoidal magnetic field, the momentum of charged particles can be measured from the resulting curvature. By extrapolating a track back towards the interaction point, it is possible to identify jets containing B hadrons. This so-called b -tagging will be discussed in more detail in Section 5.2. The ID is 5.5 m long, has a diameter of 2.1 m and covers $|\eta| < 2.5$. It is designed on the principle that close to the interaction point only a few, but very precise space points are measured with detectors with a high degree of segmentation, while at larger radii less precise detectors with a larger number of measurements along the particle track are used. This also minimizes the detector occupancy for the high track density expected at the LHC design luminosity, making readout and pattern recognition easier.

The ID consists of three subdetectors: A high resolution pixel detector, a micro-strip Semi Conductor Tracker (SCT) and a Transition Radiation Tracker (TRT). A schematic view of the inner detector is shown in Figure 3.5.

The expected resolutions of track impact parameters are [66]:

$$\sigma(d_0) = 11 \oplus \frac{73}{p_T / \text{GeV} \sqrt{\sin \theta}} \mu\text{m} , \quad (3.5)$$

$$\sigma(z_0) = 87 \oplus \frac{115}{p_T / \text{GeV} \sqrt{\sin^3 \theta}} \mu\text{m} . \quad (3.6)$$

The expected resolution of the momentum measurement of single particles is [66]:

$$\sigma(1/p_T) = 0.36 \oplus \frac{13}{p_T / \text{TeV} \sqrt{\sin \theta}} \text{TeV}^{-1} . \quad (3.7)$$

In the following the three sub-detectors of the ID are described in more detail.

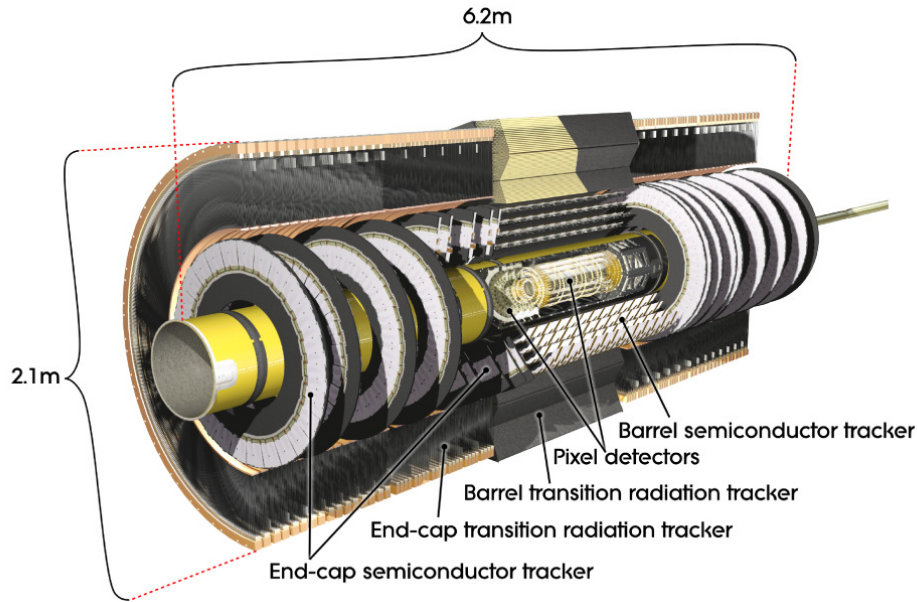


Figure 3.5: Cut-away view of the ATLAS inner detector [58].

The pixel detector

The pixel detector is the innermost tracking detector of ATLAS, giving high precision space points of charged particles close to the interaction region.

It is a hybrid silicon pixel detector, consisting of three barrel layers and three forward disks on each side. The barrel layers consist of 1456 modules located at mean radii of 5.05 cm, 8.85 cm and 12.25 cm from the nominal beam position. The disks with 48 modules each are located on either side of the barrel modules at $z = \pm 49.5$ cm, $z = \pm 58.0$ cm, and $z = \pm 65.0$ cm. A pixel module consists of a silicon sensor and 16 FE-I2 readout-chips, each reading out 18×160 pixel cells. The sensor itself acts as a diode, which is depleted by an applied bias voltage. Charged particles traversing the depleted silicon material create electron-hole-pairs by ionization. The resulting electrons drift to the cathode side of the sensor, where they are collected in tiny bump bonds which connect the sensor with the readout-chips. In this way, the sensor is segmented into $16 \times 18 \times 160$ pixels with a size of $400 \times 50 \mu\text{m}^2$, resulting in 46080 pixels per module and about 80 million pixels in total. The spacial resolution of the pixel detector is expected to be $10 \mu\text{m}$ in $R\phi$, $115 \mu\text{m}$ in z for the barrel, and $10 \mu\text{m}$ in $R\phi$, $105 \mu\text{m}$ in R for the disks. The very high degree of segmentation is also necessary to cope with the high track density expected in high luminosity running conditions and at the same time provide a robust pattern recognition capability.

The Semi Conductor Tracker

The Semi Conductor Tracker (SCT) is another silicon tracking device, but in this case the modules are not segmented in pixels but in strips. Each silicon detector has a size of $6.36 \times 6.40 \text{ cm}^2$ (in the barrel) and is segmented on the readout side into 768 strips with a

pitch of $80 \mu\text{m}$. A module consists of four such sensors. Two detectors are wire-bonded together to form 12.8 cm long strips. Two such double-detectors are arranged back-to-back forming a 40 mrad stereo angle between the strips on the top and on the bottom to have access to the z coordinate of tracks.

The SCT modules are arranged in four barrel layers at mean radii between 30 cm and 52 cm , covering $|\eta| < 1.4$ and in nine disks on both sides of the barrels to measure tracks up to $|\eta| = 2.5$. The expected spatial resolution is $17 \mu\text{m}$ in $R\phi$ and $580 \mu\text{m}$ in the z direction. The total number of readout channels in the SCT is approximately 6.3 million. The coarser segmentation of the SCT is possible due to the lower track density at larger radii.

The Transition Radiation Tracker

The two high precision trackers are complemented by a less precise transition radiation tracker (TRT) that gives more space point measurements. On average it provides 36 measurements per track. It is build of straw tube detectors with diameters of 4 mm and a maximal length of 144 cm . In the center of each straw is a gold-plated tungsten-rhenium wire with a diameter of $50 \mu\text{m}$ that is placed on a positive high voltage. The straw tubes are filled with a gas mixture of 70% Xenon, 27% carbon dioxide and 3% oxygen with 5 - 10 mbar overpressure. A charged particle traversing a straw tube ionizes the gas. The produced electrons drift towards the wire with a constant velocity. Close to the wire the signal is amplified by an avalanche effect in the high electric field. With the known drift velocity, a drift circle can be calculated in which the particle must have passed the center of the straw tube. The expected spatial resolution is $130 \mu\text{m}$ per straw. In addition to the measurement of space points of charged particles, the TRT can also be used for particle identification. The straw tubes are surrounded by a radiator material (polypropylene fibers in the barrel, foils in the end-cap) so that a traversing charged particle passes many boundaries with changes in the index of refraction. An ultra-relativistic particle ($\gamma \gtrsim 1000$) will emit transition radiation photons at these boundaries at small angles to the flight direction. The photons are then absorbed by the drift gas via the photoelectric effect due to the high Z of the Xenon, resulting in an additional signal in the hit straw. Ultra-relativistic particles leave in this way a higher amplitude signal in the TRT. Due to the low mass of the electron, this technique can be used to distinguish between electrons and pions over a wide momentum range, completely complementary to calorimetric information.

The barrel consists of about 50000 straws arranged in three rings with a total of 73 layers. It covers radii from 56 cm to 107 cm and $|\eta| < 0.7$. Larger pseudo-rapidities are covered by two end-caps, each built of 18 wheels which are grouped into wheel 'A' (6 disks), wheel 'B' (8 disks) and wheel 'C' (4 disks with smaller inner radii than the other two wheels). In these wheels the straw tubes are arranged radially. This geometry would result in a coverage up to $|\eta| < 2.5$. The TRT 'C'-wheels are not installed in the initial ATLAS detector, but have been deferred for a possible later addition. This reduces the TRT acceptance to $|\eta| < 2.1$. The TRT has a total number of readout channels of about 351000.

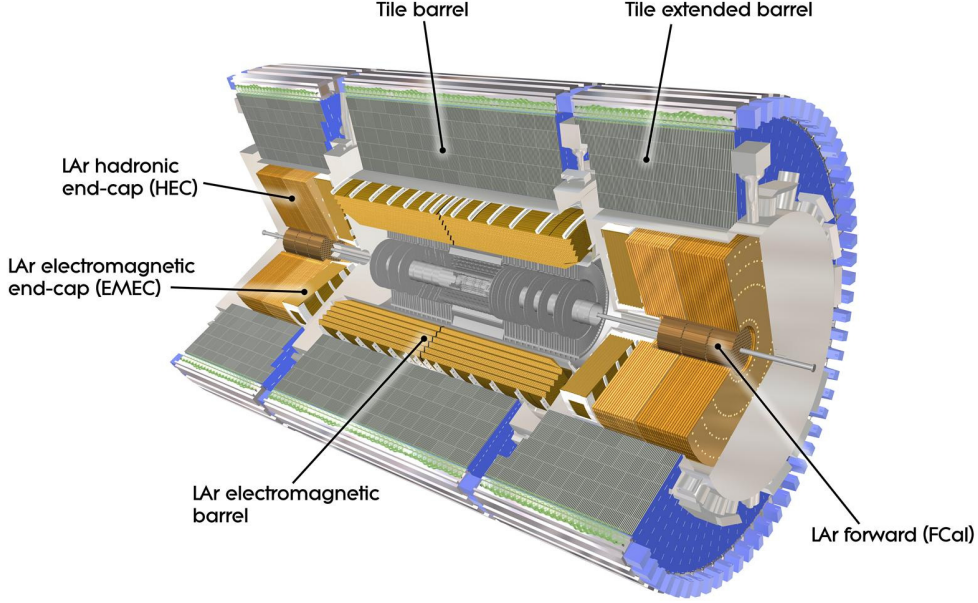


Figure 3.6: Cut-away view of the ATLAS calorimeter system [58].

3.2.4 The calorimeter system

The ATLAS calorimeter system shown in Figure 3.6 consists of the electromagnetic calorimeter (ECAL) followed by the hadron calorimeter (HCAL). Both calorimeters are sampling calorimeters constructed of alternating layers of an active medium and of passive absorber material in order to measure the energy of absorbed particles.

The electromagnetic calorimeter identifies electrons and photons and precisely measures their energies. It comprehends a barrel part covering the region $|\eta| < 1.5$ and two end-cap calorimeters (EMEC) covering $1.4 < |\eta| < 3.2$. All parts are using liquid argon (LAr) as the active medium and lead as the absorber material arranged in accordion-like shape in order to achieve homogeneous ϕ -coverage. The design goal for the energy resolution of electrons and photons is [58]:

$$\frac{\sigma(E)}{E} = \frac{0.1}{\sqrt{E/\text{GeV}}} \oplus 0.007. \quad (3.8)$$

Furthermore, the electromagnetic calorimeter is used to trigger on electrons and photons within $|\eta| < 2.5$.

The hadron calorimeter comprises a tile calorimeter and two liquid argon end-cap calorimeters (HEC). The tile calorimeter consists of a barrel part with $|\eta| < 1.0$ and two extended barrels covering $0.8 < |\eta| < 1.7$. All parts are using steel as absorber and scintillating tiles as active material. Radially, the tile calorimeter extends from an inner radius of 2.28 m to an outer radius of 4.25 m. Because the irradiation doses are too high for

scintillators in the end-cap region, liquid argon is used there as active material and copper as absorber. The end-cap calorimeter is composed of two independent wheels per end-cap, each built from 32 wedge-shaped modules, following behind the EMECs and sharing the same cryostats.

In the region $3.1 < |\eta| < 4.9$, LAr Forward Calorimeters are integrated in the end-cap cryostats, each consisting of an electromagnetic module (FCAL1) and two hadronic modules (FCAL2 and 3) using copper and tungsten as absorber material, respectively. The design goal for the energy resolution for jets is [58]:

$$\frac{\sigma(E)}{E} = \frac{0.5}{\sqrt{E/\text{GeV}}} \oplus 0.03 \quad |\eta| < 3.2, \quad (3.9)$$

$$\frac{\sigma(E)}{E} = \frac{1.0}{\sqrt{E/\text{GeV}}} \oplus 0.10 \quad |\eta| > 3.2. \quad (3.10)$$

The total thickness of the calorimeter system is more than 22 radiation lengths (X_0) and approximately ten hadronic interaction lengths, which is required to achieve good containment for electromagnetic and hadronic showers with limited punch-through into the muon spectrometer. The thickness and the large η coverage (up to $|\eta| = 4.9$) of the calorimeter system provides accurate E_T^{miss} measurement and high energy resolution for highly energetic jets.

3.2.5 The muon spectrometer

The layout of the muon spectrometer is shown in Figure 3.7. The purpose of this outermost subdetector is to provide a precise muon momentum measurement based on the magnetic deflection of muon tracks in the magnetic field generated by the three air-core toroids (cf. Section 3.2.2). The muon spectrometer is instrumented with dedicated trigger chambers, Resistive Plate Chambers (RPC) in the barrel region and Thin Gap Chambers (TGC) in the end-cap region. Monitored Drift Tube (MDT) chambers and Cathode Strip Chambers (CSC) serve as high precision tracking systems in the barrel and the end-cap regions, respectively. The muon chambers in the barrel region are arranged in three cylindrical layers around the beam axis whereas the chambers in the end-cap regions are installed in four planes perpendicular to the beam axis.

The design based on air-core toroids has been chosen to minimize multiple scattering and hence, to allow for a stand-alone measurement of the muon momentum and direction. However, in order to achieve higher precision and efficiency, in particular for low- p_T muons, also inner detector and calorimeter measurements are exploited in the muon reconstruction.

The different chamber types are described in more detail in the following.

Precision chambers

Two types of chambers are used for the precision measurements of muon trajectories: Monitored Drift Tubes (MDT) and Cathode Strip Chambers (CSC). In the barrel they are located in three cylindrical layers around the beam axis at approximate radii of 5, 7.5, and 10 m.

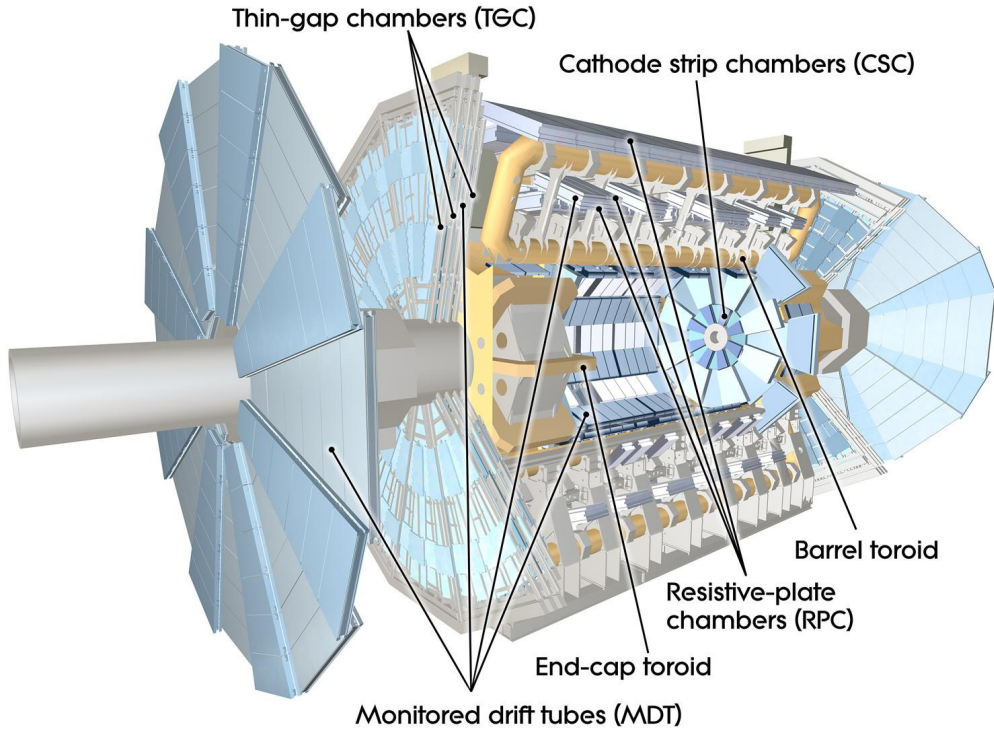


Figure 3.7: Cut-away view of the ATLAS muon spectrometer [58].

In the end-cap regions the four stations are installed horizontally at $|z| \sim 7, 10, 14,$ and $21\text{-}23$ m.

Over almost the whole pseudo-rapidity range ($|\eta| < 2.0$) the precision measurement is performed exclusively using MDTs. These consist of cylindrical drift tubes made of aluminum with a diameter of 3 cm. In the middle of each tube is a tungsten-rhenium sense wire with a diameter of $50 \mu\text{m}$. The used drift gas is a mixture of 93% argon and 7% carbon dioxide at a pressure of 3 bar. The total gas-filled volume is about 800 m^3 . The expected spatial resolution is $80 \mu\text{m}$ perpendicular to the wire direction, which corresponds to the Rz plane. Between three and eight layers of these drift tubes are combined in one chamber.

In the region $2.0 < |\eta| < 2.7$ with larger radiation and background levels, CSCs are used in the inner muon station due to their higher granularity and relative insensitivity to neutron backgrounds. They are flat multiwire proportional chambers with $30 \mu\text{m}$ diameter tungsten-rhenium anode wires. The drift gas is 80% argon and 20% carbon dioxide with a total volume of 1.1 m^3 . The readout is done using a cathode segmented into strips. In combination with charge interpolation between neighboring strips a spatial resolution of $60 \mu\text{m}$ is reached.

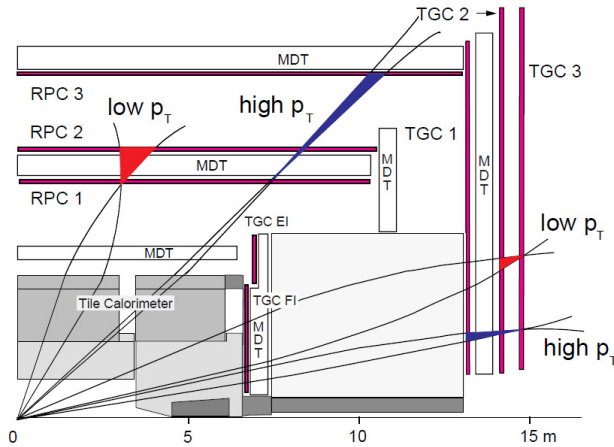


Figure 3.8: Schematic view of the muon trigger system [58]. RPC2 and TGC3 are the reference (pivot) planes for barrel and end-cap, respectively.

Trigger chambers

The trigger chambers have to provide fast information on the transverse momentum of muon tracks traversing the muon spectrometer to be used in the L1 trigger logic (see Section 3.2.6). In addition, they have to provide bunch-crossing identification and a measurement of the second coordinate perpendicular to the bending plane of the muon track which both cannot be provided by the MDT chambers. The muon trigger system covers the full ϕ -range and the pseudo-rapidity range up to $|\eta| = 2.4$.

The muon momenta corresponding to a given p_T are strongly increasing with η and the end-cap trigger layers are located outside the magnetic field (see Figure 3.8). Furthermore, the background rates in the end-cap regions exceed the ones in the barrel on average by a factor ten. Hence, in order to obtain a constant p_T -resolution over the covered η -range, different detector technologies and granularities have to be employed depending on the location of the chamber. Resistive Plate Chambers (RPC) are used in the barrel region ($|\eta| < 1.05$) and Thin Gap Chambers (TGC) in the end-cap regions ($1.05 < |\eta| < 2.4$).

Figure 3.8 shows the schematic layout of the muon trigger system. The barrel trigger system consists of three layers of RPCs located below and above the middle MDT layer (RPC1 and RPC2) and above (below) the outer MDT layer in the large (small) sectors (RPC3). In the end-cap regions, three TGC planes provide trigger information. One in front (TGC1) and two behind (TGC2 and TGC3) the second MDT wheel. The trigger is generated by coincidence patterns which correspond to certain curvatures of the tracks and are used as a criterion that the track passes a certain p_T threshold. A measure of the curvature, i.e. the deviation of the track from straightness, is the difference of the slope of the track segment between two trigger chambers and the slope of the straight line from the interaction point to a hit on the track in the reference (pivot) plane which is the RPC2 plane in the barrel and the TGC3 plane in the end-caps. For example in the barrel, for the low (high)- p_T trigger the slope of the track segment between hits in the RPC2 and RPC1 (RPC3) plane is compared to the slope of the straight line between the interaction point and the hit in the RPC2 plane.

The RPCs consist of two resistive plates which are kept parallel to each other at a distance of 2 mm by insulating spacers. An electric field of 4.9 kV/mm is applied, leading to

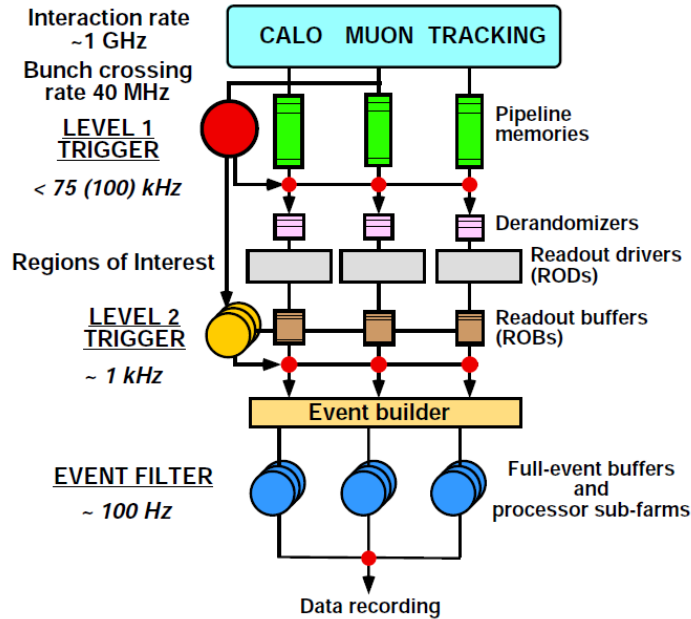


Figure 3.9: The ATLAS trigger system [66].

the formation of avalanches when an ionizing particle passes the gas volume. The gas used is a mixture of 94.7% $C_2H_2F_4$, 5% Iso- C_4H_{10} , and 0.3% SF_6 .

The TGCs are similar to multiwire proportional chambers with both wire readout for the radial coordinate in the bending direction and azimuthal information by radial strips. They are operated in saturation mode providing a very quick response. The gas mixture is 55% carbon dioxide and 45% n-pentane with a total volume of 11 m³.

3.2.6 Trigger and data acquisition

The high luminosity of the LHC imposes an enormous technical challenge on the trigger and data acquisition system in order to reduce the event rate by efficiently selecting and recording interesting physics events. With an average event size of approximately 1.3 Mbyte, the ATLAS computing system is capable of handling a final event rate of 200 Hz which has to be met by the output of the trigger system.

The trigger selection proceeds in three consecutive levels, L1, L2 and the event filter and are shown in Figure 3.9. Each level refines the trigger decision of the previous one. The first level (L1) is completely hardware based and uses only a limited amount of detector information to provide a trigger decision in less than 2.5 μ s. It exploits trigger information provided by the muon spectrometer and the calorimeters at a reduced granularity. The selection criteria and thresholds are chosen to select events with high- p_T muons, electrons, photons, jets and hadronically decaying τ -leptons as well as large missing and total transverse energy. The selected events with their associated Regions-of-Interest (RoI), i.e. the regions in the detector where interesting patterns have been identified, are passed to the second trigger level (L2) at a rate of 75 kHz. The L2 selection criteria have been cho-

sen such that the event rate is reduced to 3.5 kHz at an event processing time of 40 ms. The selection is based on the detector information at full granularity and precision within the RoIs ($\sim 2\%$ of the data). The full detector information for events selected by the L2 trigger is collected by the event builder and passed to the event filter (EF). This third step of the event selection is entirely software based and is running on a dedicated computer farm. Offline event reconstruction algorithms are employed and the final trigger decision is provided at an event processing time on the order of four seconds and at a final event rate of 200 Hz. Events selected by the trigger system are recorded on mass-storage devices for further processing and physics analyses. One year of ATLAS data taking at the LHC amounts to a data volume of approximately 1 Pbyte. The data volume recorded by all experiments at the LHC cannot be stored and processed by one local computing center alone. Therefore, after initial processing at CERN, the recorded data is distributed to many computing centers outside CERN which together form the LHC Computing Grid (LCG), a worldwide computing framework [67, 68].

4 Outline of the analysis strategy

In this Section the analysis strategy for detecting a heavy charged Higgs boson in the $H^+ \rightarrow t\bar{b}$ decay channel is described. The full chain of production and decay for a positively charged Higgs boson is given by ¹:

$$g\bar{b}/gg \rightarrow [b]H^+\bar{t} \rightarrow [b]t\bar{b}\bar{t} \rightarrow [b]bW^+\bar{b}W^-\bar{b} \rightarrow [b]bl\nu\bar{b}q\bar{q}'\bar{b}. \quad (4.1)$$

Here, one of the two top quarks is required to decay leptonically in order to provide a hard isolated lepton to trigger on. The complete final state to be reconstructed is very complex with three respectively four jets coming b quarks, two hadronic jet from lighter quarks, one high- p_T lepton and one neutrino. One of the possible Feynman diagrams describing such an event is shown in Figure 4.1. This channel has previously been studied in ATLAS at a center-of-mass energy of $\sqrt{s} = 14$ TeV in the m_h -max scenario for an integrated luminosity of 30 fb^{-1} [64]. No H^+ discovery or exclusion power could be extracted from this channel on its own. It, however, contributes to the combined H^+ sensitivity. As it was shown in these study, the large background from Standard Model $t\bar{t}$ -production complicates the detection of the charged Higgs boson. Purpose of the present study is to improve the discovery reach by applying a different analysis technique.

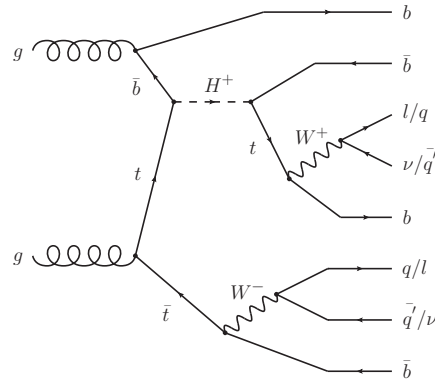


Figure 4.1: One of the possible Feynman diagrams for heavy charged Higgs boson production and decay.

The analysis is divided into three parts. In the first step all events are required to pass a set of selection cuts in order to reject most of the Standard Model background and to ensure the minimum prerequisites needed for subsequent event reconstruction. The second part is intended to find the combination of jets that correctly reconstructs the two top quark decays. For each event the jet combination is found which has the highest probability of

¹The oppositely charged Higgs boson, H^- , is meant to be included in all following equations and decay modes.

being correct with the help of a kinematic fitting procedure described in Section 5.4. Once the best combination is found in each event, one of the remaining jets is grouped together with one of the top quarks in order to reconstruct the charged Higgs boson. In the last step, several cuts on kinematic or topological variables are applied, aiming at separating the signal from the Standard Model background processes. The reconstruction of H^+ is presented in Section 5.6. Various systematic uncertainties are considered and their impact is evaluated and discussed in Section 6.

In order to extract the discovery and exclusion potential in the m_h -max scenario, all events within a certain mass window around the nominal mass of the charged Higgs boson are selected. The significance is calculated for each H^+ mass and value of $\tan\beta$ with the help of the Profile Likelihood method [69] described in Section 7. Systematic uncertainties are taken into account and the resulting discovery and exclusion contours are determined and discussed.

5 Analysis

5.1 Signal and background

In this Section the main Standard Model background components for the reconstruction of heavy charged Higgs bosons in the decay mode $H^+ \rightarrow t\bar{b}$ are described. The considered Monte Carlo samples together with their cross-sections are given for an center-of-mass energy of $\sqrt{s} = 10$ TeV.

5.1.1 Physics background

The main background to charged Higgs boson production and its decay as in Eq. 4.1 is the Standard Model top anti-top quark production. This background is very challenging not only because of its similarity to the signal final state but also because of its large production cross-section of about 401.6 pb [70,71]. Given the high jet multiplicity in the signal process (≥ 5 jets), only $t\bar{t}$ events produced together with at least one extra jet contribute. Since most of these extra jets are from the hadronisation of light quarks, this contribution is reduced if three (or four) jets are identified as b -jets.

An irreducible background comes from $t\bar{t}b\bar{b}$ production which comprises the same final state objects as the signal process. This background can proceed via QCD or electroweak (EW) interactions with a total cross-section of the order of 4 pb [72]. Some of the Feynman diagrams involved in the two production mechanisms are shown in Figure 5.1 and Figure 5.2. For this channel only LO calculations are used. A newer calculation [73] has been recently published but has not been incorporated within this study. In the LHC energy range, the ratio between NLO and LO cross-section for this process can vary between 0.5 and 1.5 or even more in some corners of phase-space, making it important to use the NLO predictions for a proper background estimate in successor studies or to estimate the background from data.

Several other backgrounds, such as W +jets, single top and QCD multijet production, could also have a non-negligible impact on the analysis. The $W + 2$ jets cross-section is about 3.4 nb ($W \rightarrow \ell\nu + 2$ -5 jets). It is shown in this analysis that the contribution can be reduced to a negligible level if a three b -tag requirement is applied. This is also true for the less abundant single top background, which has a cross-section of about 165 pb [74].

Even when three or more b -jets are requested in the event, contamination from QCD $b\bar{b}b\bar{b}$ production, which has a cross-section of a few hundred nb [75], is still possible. In this analysis, any QCD background is however neglected. The reconstruction of the $t\bar{t}$ system allows a certain degree of safety against non-top background.

5.1.2 Monte Carlo samples and cross-sections

In this study, four different charged Higgs boson masses are considered. Table 5.1 lists the mass points for which Monte Carlo samples are produced and gives the cross-sections and

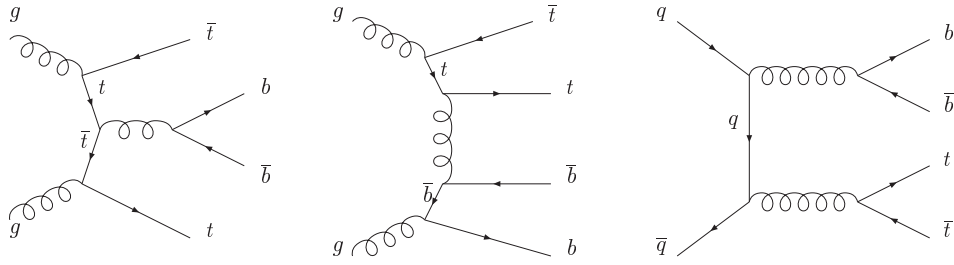


Figure 5.1: Example of Feynman diagrams for the $t\bar{t}b\bar{b}$ QCD production.

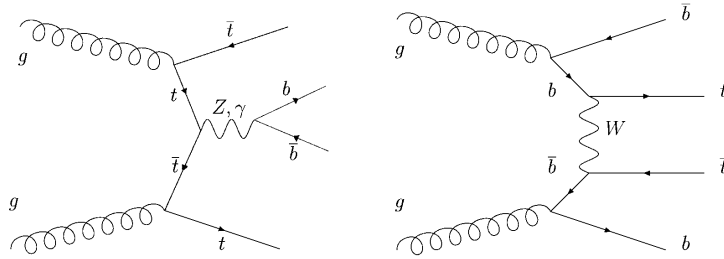


Figure 5.2: Example of Feynman diagrams for the $t\bar{t}b\bar{b}$ electroweak production.

the corresponding Monte Carlo luminosities for $\tan\beta = 30$. Details of the signal Monte Carlo sample can be found in Appendix A.

The list of background Monte Carlo samples considered in this study is given in Table 5.2. They include the Standard Model processes involving top quarks and W bosons. The table summarizes the cross-sections, calculated using the respective Monte Carlo generator of the different processes, together with the corresponding numbers of generated events and the equivalent integrated luminosity. All branching fractions and filter efficiencies are included.

The reducible $t\bar{t}$ background events are generated at next-to-leading order with the *MC@NLO* [76] program, interfaced to *Herwig* and *Jimmy* [77]. The events in this sample correspond to the processes $pp \rightarrow t\bar{t} \rightarrow (\ell\nu, q\bar{q}')b\ell\nu b$ with $\ell = e, \mu, \tau$. For the inclusive $t\bar{t}$ cross-section the NLO+NLL calculation of $\sigma(pp \rightarrow t\bar{t}) = 401.6$ pb was used.

For both $t\bar{t}b\bar{b}$ QCD and EW samples, the exact process generated is $gg \rightarrow t\bar{t}b\bar{b} \rightarrow \ell\nu b\bar{q}\bar{q}' b\bar{b}X$, with $\ell = e$ or μ . For the $t\bar{t}b\bar{b}$ QCD sample, *Alpgen* [78] is used and interfaced to *Herwig* and *Jimmy* for the simulation of the initial and final state radiation, hadronisation and decay. The $t\bar{t}b\bar{b}$ EW sample is generated using *AcerMC* [79] and *Pythia* [80]. Both samples are only available using ATLAS fast simulation (*Atlfast*).

There is an overlap of the $t\bar{t}$ and $t\bar{t}b\bar{b}$ samples since the extra gluon in the NLO $t\bar{t}$ calculation can split into a $b\bar{b}$ pair during parton showering. This affects about 10% of the events in the $t\bar{t}$ sample. Following the overlap treatment as explained in Reference [64],

m_{H^+} [GeV]	$\sigma \times \text{BR}$ [fb]	L [fb^{-1}]
250	253	44
300	182	61
400	81	140
600	14	837

Table 5.1: Summary of the signal samples for the various charged Higgs boson masses studied in this analysis. Every sample consist of about 20k events. The cross-sections are calculated at NLO and the luminosities are quoted for $\tan\beta = 30$ for the m_h -max scenario. The branching ratios contain only the process $H^+ \rightarrow t\bar{b}$.

events with additional $b\bar{b}$ pairs in the *MC@NLO* sample are rejected on an event-by-event basis and the associated cross-section is corrected for this subtraction.

5.2 Reconstruction of physics objects

In this Section the definitions of the basic reconstructed objects - electrons, jets, muons and missing transverse energy - used in this analysis is given. The definitions are based upon standard reconstruction algorithms developed for the ATLAS detector [64].

Electrons

Electron candidates are reconstructed by the calorimeters and the inner tracker of ATLAS, i.e. are electromagnetic energy deposits matched to tracks. A cut-based quality requirement identifies signal electrons with high efficiency while keeping the misidentification rate from hadronic jets low; the electrons candidates are required to satisfy the so-called *medium* purity cuts [64]. In addition, they are required to have pseudo-rapidity $|\eta| < 2.5$ and transverse momentum $p_T > 20$ GeV. Finally, the electron candidates are required to be isolated based on calorimeter energy deposition. The total transverse energy E_T in a cone of $\Delta R = 0.2$ around the centroid of the electromagnetic cluster, which is deposited in addition to the E_T of the electron candidate, has to be below 6 GeV.

Jets

Jet reconstruction is performed with the seeded anti- k_r algorithm [81] (*AntiKt4HI**Topo*) using calorimeter topological clusters and a cell calibration using the H1 method [64]. The topological cell clusters are a representation of the calorimeter signals where three-dimensional energy depositions, representing the showers developing for each particle entering the calorimeter, are reconstructed. The jets are required to lie within $|\eta| < 5.0$ and to have a transverse energy above a given threshold $p_T > 20$ GeV.

Since most electron candidates are also reconstructed as jets, those jets near selected electrons should be removed to avoid double-counting. Therefore, all jets overlapping with a selected electron candidate within a cone of size $\Delta R < 0.2$ are not considered within this analysis.

Process	$\sigma \times \text{BR}$ [pb]	N_{events}	L [fb ⁻¹]
$t\bar{t}$ not fully hadronic	218.1	2297000	7.8
$t\bar{t}b\bar{b}$ QCD	2.65	195000	73.4
$t\bar{t}b\bar{b}$ EW	0.07	50000	704.2
Single top t -channel	43.2	125000	2.9
Single top Wt -channel	14.3	20000	1.4
$Wb\bar{b}$ + 0 parton	6.1	15500	2.5
$Wb\bar{b}$ + 1 parton	6.1	15500	2.5
$Wb\bar{b}$ + 2 parton	3.5	9000	2.5
$Wb\bar{b}$ + 3 parton	2.0	5000	2.5
$W \rightarrow e\nu$ + 2 parton	824.7	778000	0.9
$W \rightarrow e\nu$ + 3 parton	248.0	225000	0.9
$W \rightarrow e\nu$ + 4 parton	68.4	59000	0.9
$W \rightarrow e\nu$ + 5 parton	20.3	17000	0.8
$W \rightarrow \mu\nu$ + 2 parton	832.4	774000	0.9
$W \rightarrow \mu\nu$ + 3 parton	246.4	211000	0.9
$W \rightarrow \mu\nu$ + 4 parton	67.7	58000	0.9
$W \rightarrow \mu\nu$ + 5 parton	19.9	17000	0.9
$W \rightarrow \tau\nu$ + 2 parton	820.8	792000	1.0
$W \rightarrow \tau\nu$ + 3 parton	247.3	242000	1.0
$W \rightarrow \tau\nu$ + 4 parton	67.5	59000	0.9
$W \rightarrow \tau\nu$ + 5 parton	20.7	16000	0.8

Table 5.2: Summary of Monte Carlo background samples listed with their cross-section and number of events used in this analysis. The $t\bar{t}$ cross-section is evaluated at NLO precision and includes the k-factor for near-NNLO precision. All other cross-sections are at leading order, but NLO k-factors for ($Wb\bar{b}$ and $W \rightarrow \ell\nu$) + n -partons as well as for the single top samples are included.

Muons

Muons are reconstructed by using both the muon spectrometer and inner detector. The muon reconstruction is performed using the *StacoMuon* algorithm [64]. They are defined by combining information from the muon chambers and the tracking system. Muons are required to have a minimum transverse momentum $p_T > 20$ GeV and to be in the pseudo-rapidity range $|\eta| < 2.5$. They have to be isolated based on calorimeter energy: the additional transverse energy, E_T , in a cone with radius $\Delta R = 0.2$ around the muon is required to be less than 6 GeV.

Muons which are close to a selected jet, within a cone of radius $\Delta R < 0.3$, are not considered within this analysis. This helps to remove those muons which arise from decays of hadrons inside jets, such as B -mesons originating from the b quark in top decays, since this analysis aims to identify muons coming from W boson decays.

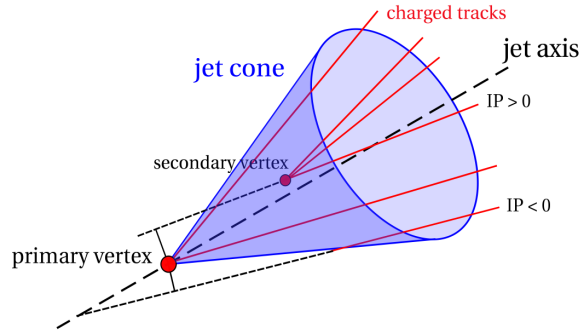


Figure 5.3: Representation (not to scale) of a hadron jet from a b quark. The impact parameter (IP) is the point of closest approach of the track with respect to the primary vertex.

Missing transverse energy definition

The missing transverse energy, E_T^{miss} , is associated with particles that escape detection. For example, E_T^{miss} is the signature of weakly interacting neutral particles such as neutrinos. It can also originate from a mismeasurement of the true transverse energy of objects or from backgrounds such as cosmic rays or beam halo. Missing \vec{E}_T is defined by $\vec{E}_T^{\text{miss}} = -\sum E_T^i \hat{n}_i$, where i is the calorimeter tower number for $|\eta| < 4.9$ and \hat{n}_i is a unit vector perpendicular to the beam axis and pointing at the i -th tower. The magnitude E_T^{miss} is defined by $|\vec{E}_T^{\text{miss}}|$. Corrections are made to the E_T^{miss} for the reconstructed objects, including electrons, muons and jets. In addition to this, in the algorithm used (*MET_RefFinal*) the E_T^{miss} is also corrected for dead material in the cryostat.

Identification of b-jets

The identification of jets originating from a b quark is a key ingredient in this analysis. Several properties of such jets can be exploited which makes it possible to distinguish them from jets stemming only from lighter quarks. One property is the relatively long lifetime of $\tau \sim 1.5$ ps of the b -hadron, which corresponds to a $c\tau \sim 460$ μm . Hence, a b -hadron in a jet with $p_T = 50$ GeV will have a significant flight path length of about 4 mm in the transverse plane before it decays with an average charged track multiplicity of 5. Therefore, tracks coming from b -hadron decays tend to have larger impact parameters since they come from a displaced vertex, while tracks originating from the primary vertex will have an impact parameter compatible with the tracking resolution. The impact parameter is the distance of closest approach of the track trajectory to the primary vertex. It is signed as positive (negative) if the decay occurs downstream (upstream) the jet, i.e. if the dot product of the jet direction with the impact parameter direction is positive (negative). As illustrated in Figure 5.3, tracks from b -hadron decays tend to have positive impact parameters since the decay vertex of the b -hadron, the so-called secondary vertex, is displaced by $\beta\gamma c\tau$ from the primary vertex. Here, $\beta\gamma$ denote the Lorentz factors of the b -hadron.

A large variety of b -tagging algorithms have been developed in ATLAS and are described in detail in Reference [64]. Most of them are based on a likelihood ratio approach and are very powerful. For such sophisticated tagging algorithms the commissioning may take some time and they need more experience with first data.

For the initial period of data taking much simpler and more robust tagging algorithms have been developed. One of them is the *TrackCounting* algorithm [82]. It has been devised, tested and fully integrated into the ATLAS software framework during this study. This algorithm has a simple requirement of a minimum number of good quality tracks with a transverse impact parameter significance exceeding a given threshold. The impact parameter significance is the impact parameter divided by its error, which gives more weight to precisely measured tracks. Tracks which fulfill the b -tagging quality cuts, e.g. at least one hit in the innermost pixel layer, are ordered by decreasing impact parameter significance. The discriminating quantity is defined as the second highest transverse impact parameter significance. Good b -tagging performance can be obtained using this algorithm. It is simple and robust and it does not require any special initialization such as calibration functions. A detailed discussion of the performance of *TrackCounting* in comparison with other b -tagging algorithms can be found in Reference [82].

Such simple tagging algorithms are very useful at the early stage of data taking because they offer a very quick optimization step and adaptation to the physical process due to the limited number of parameters. They also offer a quick feedback for detector optimization and evaluation of the impact of experimental effects (such as pile-up, misalignment, changes of the baseline design and detector parameters) on the b -tagging performance.

The *TrackCounting* algorithm is part of the recommended algorithms for the early data taking period in ATLAS. The behavior of these algorithms has been studied with the first 7 TeV collision data recorded in 2010, corresponding to an integrated luminosity of about 15nb^{-1} , and were found to compare well with expectations from Monte Carlo simulation [83, 84]. The distribution of the discriminating variable, the second highest impact parameter significance, is shown in Figure 5.4 for data and Monte Carlo. It can be seen that the overall distributions agree fairly well with each other. The negative impact parameter significances are dominated by tracks coming from light jets whereas positive ones are dominated by heavy flavor contributions. A cut on this variables is therefore leading to a very similar fraction of b -tagged jets in the experimental and in the simulated data.

However, due to the low expected cross-section of charged Higgs bosons and the challenging background this analysis will require an integrated luminosity of several tenth of fb^{-1} . If such an amount of data will be accumulated in ATLAS more sophisticated b -tagging algorithms than *TrackCounting* will be available. Hence, this analysis will use the more refined tagging algorithms.

In this study, b -jets are identified using the *IP3D+SV1* tagging algorithm which exploits both the impact parameter of tracks and properties of an inclusive secondary vertex, using a likelihood approach which leads to a single discriminating variable: the b -tagging weight.

This weight is obtained as follows: the measured value S_i of a discriminating variable is

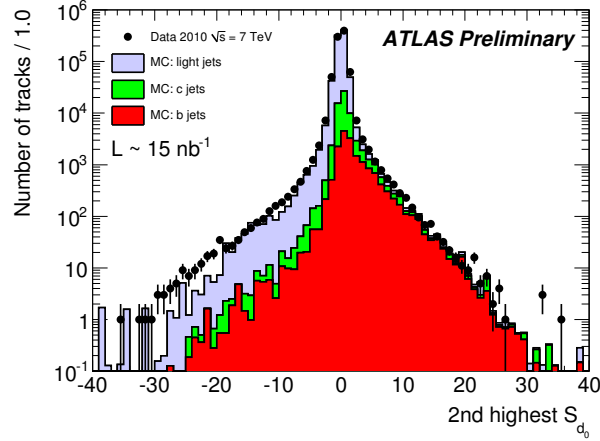


Figure 5.4: Distribution of the second highest impact parameter significance S_{d_0} for data (black points) and Monte Carlo (plain histograms) for an integrated luminosity of 15 nb^{-1} . (from [84])

compared to pre-defined smoothed and normalized distributions for both the b - and light jet hypotheses, $b(S_i)$ and $u(S_i)$. Two- and three-dimensional probability density functions are used as well for some tagging algorithms. The ratio of the probabilities $b(S_i)/u(S_i)$ defines the track or vertex weight, which can be combined into a jet weight W_{jet} as the sum of the logarithms of the n_t individual track weights w_i :

$$W_{jet} = \sum_{i=1}^{n_t} w_i = \sum_{i=1}^{n_t} \ln \frac{b(S_i)}{u(S_i)}. \quad (5.1)$$

The *IP3D* algorithm uses two-dimensional distributions of the longitudinal versus transverse impact parameters. *SVI* exploits three properties of the secondary vertex: the invariant mass of all tracks associated to the vertex, the ratio of the sum of the energies of the tracks participating to the vertex to the sum of the energies of all tracks in the jet and the number of two-track vertices. This algorithm relies on a two-dimensional distribution of the two first variables and a one-dimensional distribution of the number of two-track vertices.

The resulting b -tag weight spectrum for b - and light jets in the $t\bar{t}$ background sample is shown in the left-hand plot of Figure 5.5. A cut on the weight defines which jets will be eventually identified as b -jets in the analysis.

The b -tagging performance is given in terms of b -tagging efficiency (ϵ_b) and light jet (udsg) rejection rate. Both variables are defined on a per jet basis. The b -tagging efficiency is defined as the fraction of jets coming from a b quark that are tagged by the b -tagging algorithm while the mistagging rate is the fraction of light jets tagged as b -jets. The rejection rate is just the inverse of the mistagging rate. The decision if a jet is coming from a b quark or not is done by calculating ΔR between generated b quark and reconstructed jet. If $\Delta R < 0.3$ the jet is referred to as matched.

The b -tagging performance strongly depends on the transverse momentum, p_T , and the pseudo-rapidity, η , of the jets. The performance drops in regions of large $|\eta|$ due to an

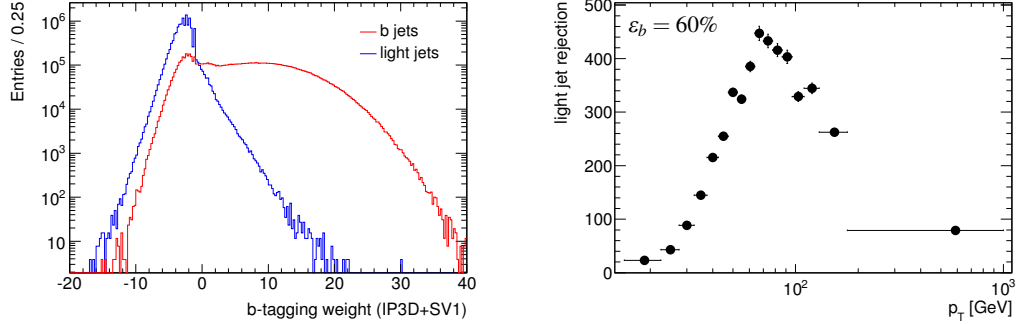


Figure 5.5: Left-hand plot: jet b -tagging weight distribution for b -jets (red histogram) and light jets (blue histogram) for the $IP3D+SV1$ tagging algorithm. The right-hand plot shows the light jet rejection rate in different intervals of jet p_T for 60% b -tagging efficiency. The width of the intervals has been chosen to contain about the same amount of jets.

increase of material compared to the central region of the inner detector. The b -tagging performance drops significantly at low p_T regions due to a decreasing charged particle multiplicity in the jet and a worse impact parameter resolution arising from increased multiple scattering of tracks coming from a softer p_T spectrum. In high p_T regions there is a mild degradation in b -tagging performance due to several effects: the pattern recognition of the track finding algorithm is more difficult if more tracks per volume are present and the multiplicity of charged particles from the primary vertex is increased due to the increase of the hadronisation component of the jet. Hence, the discrimination between light and b -jets is reduced. This behavior can be nicely seen in the right-hand plot in Figure 5.5 for a fixed b -tagging efficiency $\varepsilon_b = 60\%$.

The rejection of light jets versus b -tag efficiency, obtained by varying the weight cut, is illustrated in the left-hand plot in Figure 5.6 for the $t\bar{t}$ and the four different H^+ samples. Due to different jet p_T spectra of the individual processes their performances differ up to a factor of two for a fixed b -tag efficiency. As a consequence, a simple cut on a global b -tagging weight does not lead to the same performance between the various samples. To obtain a more uniform response when requiring a certain ε_B , the weight cuts are optimized in intervals of jet transverse momentum. Figure 5.6 (right-hand plot) shows the light jet rejection rate in four intervals of the jet p_T for 60% b -tagging efficiency. It can clearly be seen that the light jet rejection rates agree well between the different samples.

In this analysis, 17 intervals of jet p_T are used to obtain different weight cuts for a given ε_B . The high statistic $t\bar{t}$ sample was used for this optimization.

5.3 Reconstruction of semileptonic top anti-top candidates

The reconstruction of the four-momentum of at least one of the top quarks is necessary in order to reconstruct a charged Higgs boson. In this analysis it is required to reconstruct also the second top quark to be able to control the huge combinatorial background and the

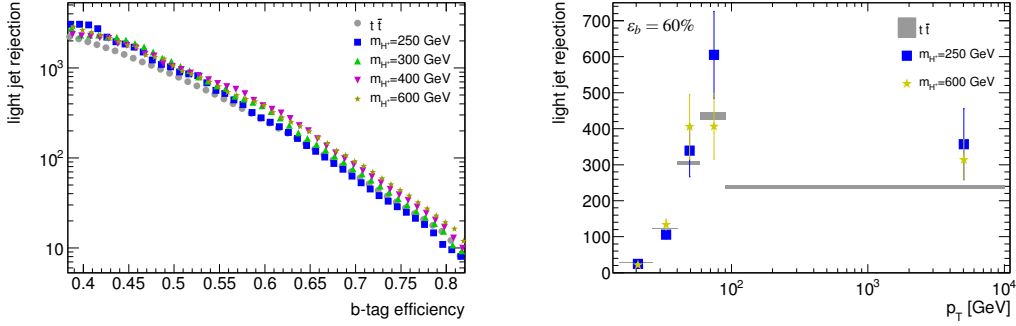


Figure 5.6: Integrated light jet rejection rate over jet p_T versus b-tagging efficiency for different samples (left-hand plot). No errors are shown but the statistical uncertainties are in the order of the markersizes. The right-hand plot shows the light jet rejection rate in four intervals of the jet p_T for 60% b-tagging efficiency. The width of the intervals has been chosen to contain about the same amount of jets.

background arising from processes not containing a $t\bar{t}$ pair.

This part of the analysis is intended to efficiently select semileptonically decaying $t\bar{t}$ pairs and to suppress most of the remaining Standard Model background.

5.3.1 Final state reconstruction

For the reconstruction of top anti-top pairs in the semileptonic decay mode, only objects fulfilling the criteria given in the previous Section are considered. In addition, it is required that only one isolated lepton (electron or muon) is selected in the event. Furthermore, a cut on $E_T^{\text{miss}} > 20$ GeV is applied since true missing energy is apparent due to a neutrino from the decay of one W boson.

In Figure 5.7, the number of selected jets per event for signal and background samples are depicted. The average number varies from about two jets for background processes up to 6 jets per event for events containing true $t\bar{t}$ pairs. Besides the physics background the latter leads to a large combinatorial background component. More than 3 jets are needed to reconstruct at least one $t\bar{t}$ candidate, whereas, from pure the statistical point of view, 12 different combinations of jet assignments are possible if 4 jets are present in the event. Even with restrictions, this number rapidly grows with the number of jets per event. In a later stage of the analysis, methods are developed which select only one combination for the final H^+ reconstruction.

Reconstruction of hadronically decaying W boson

In each event the invariant mass of every pair of jets is calculated to identify combinations consistent with the decay $W \rightarrow qq^{\bar{}}$. Only combinations satisfying $m_W^{\text{true}} \pm 60$ GeV are retained. Here, $m_W^{\text{true}} = 80.4$ GeV is the nominal W boson mass [4]. In the following, the two assigned jets will be referred to as first and second jet of the hadronically decaying W boson, ordered by their transverse momentum.

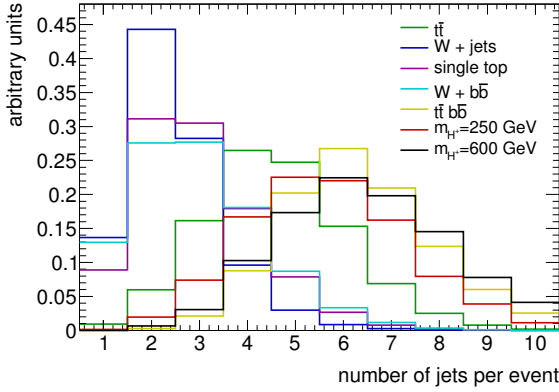


Figure 5.7: Normalized distribution of the number of jets per event. Only jets with transverse momentum $p_T > 20$ GeV are considered.

Reconstruction of leptonically decaying W boson

Since the neutrino escapes undetected, one can not directly retrieve its kinematic properties. Nevertheless, its transverse momentum, p_T , can be reconstructed assuming that the transverse energy is conserved in the collision process. The p_T of the neutrino corresponds therefore to the measured missing transverse energy E_T^{miss} in the detector. To determine the longitudinal momentum, p_z^v , of the neutrino the following equation is used:

$$\begin{aligned} m_{W,true}^2 &= m_{\ell\nu}^2 \\ &= m_\ell^2 - 2(p_x^\ell p_x^v + p_y^\ell p_y^v) + 2E_\ell \sqrt{(E_T^{\text{miss}})^2 + (p_z^v)^2} - 2(p_z^\ell p_z^v). \end{aligned} \quad (5.2)$$

This leads to a quadratic equation $ap_z^v{}^2 + bp_z^v + c = 0$ with:

$$\begin{aligned} a &= E_\ell^2 - p_z^v{}^2 \\ b &= -2p_z^v \left(\frac{m_{W,true}^2 - m_\ell^2}{2} + p_x^\ell p_x^v + p_y^\ell p_y^v \right) \\ c &= E_\ell^2 E_T^{\text{miss}2} - \left(\frac{m_{W,true}^2 - m_\ell^2}{2} + p_x^\ell p_x^v + p_y^\ell p_y^v \right)^2. \end{aligned}$$

When the discriminant $d = b^2 - 4ac$ is positive, one obtains two solutions for p_z^v :

$$p_{z,1,2}^v = \frac{-b \pm \sqrt{d}}{2a}. \quad (5.3)$$

If d is negative, no solution can be found. This can happen if the measured E_T^{miss} is large such that the neutrino-lepton invariant mass is greater than m_W^{true} . This can e.g. occur if additional neutrinos coming from semileptonic hadron decays inside jets are present in such an event. Furthermore, mismeasured transverse energy and background events contribute.

In this study, for every neutrino solution a leptonic W boson candidate is constructed where its full four-momentum is reconstructed with the help of E_T^{miss} . As a consequence of the algorithm, the reconstructed invariant mass of a W boson candidate is exactly 80.4 GeV. In case no solution can be found, a W candidate is created as well, but only one. In a later stage of the analysis its kinematic properties is estimated taking into account additional constraints.

Top quark reconstruction with the hadronic side

In each event, the hadronic top quark candidates are reconstructed by pairing all remaining jets within $|\eta| < 2.5$ with every hadronically decaying W boson candidate. Only combinations fulfilling $m_{top}^{\text{true}} \pm 80$ GeV are retained, where $m_{top,\text{true}} = 172.5$ GeV is the nominal top quark mass used in the Monte Carlo generators. In the following, the assigned jet will be denoted as the third jet of the hadronic top quark. No b -tag criteria is required so far.

Top quark reconstruction with the leptonic side

Leptonically decaying top quark candidates are reconstructed by pairing every selected jet within $|\eta| < 2.5$ with the leptonic W bosons. If a neutrino solution was found in the event, the full kinematic property of the top quarks can be reconstructed and only candidates fulfilling $|m_{top}^{\text{lep}} - 172.5 \text{ GeV}| < 80$ GeV are kept for further analysis. In the case where no solution was found, the top quark mass can not be reconstructed. However, a candidate is build in that case as well. Its four-momentum will be estimated in a later stage of the analysis. Also here, no b -tag criteria is required so far and the assigned jet will be denoted as third jet of the leptonic top quark.

5.3.2 Association of reconstructed objects to particles on Monte Carlo generator level

In order to construct and test the performance of event reconstruction algorithms, it is necessary to know the link between generated particles and reconstructed jets or leptons. The former is often referred to as *Monte Carlo generator level*, and the latter as to the *reconstructed object*.

Initially no such link between a parton and a reconstructed jet is provided by the Monte Carlo generator or the detector simulation program. Such an association is far from straightforward. In this analysis the problem is handled approximately by solving the assignment problem as described in the following. In addition, it is required that the generated object has to originate from the direct or subsequent decay of a Monte Carlo top quark.

In case of jets, the quantity which is minimized is the ΔR distance between the generated partons after final state radiation (FSR) and their associated reconstructed jet. This distribution is shown in Figure 5.8 for the different jet sources and jet transverse momenta. In all cases, a distinct minimum around $\Delta R = 0.3$ is apparent. In addition, the position of the minimum is also quite stable when selecting different intervals of the jet p_T . Hence, if the distance between a parton and its reconstructed object exceeds 0.3 it is assumed that no association is possible otherwise it is referred to as matched to a generated parton. A

slightly higher value up to about 0.4 is also possible but will lead to an increased probability of double matching. Here, more than one jet may be found around the parton fulfilling the ΔR cut. For a cut value of 0.3 such cases are very rare (per mille level) and are skipped for further analysis.

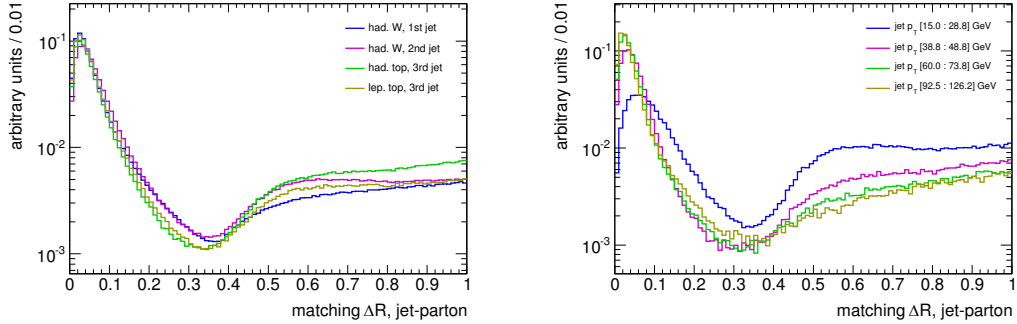


Figure 5.8: Minimal distance in ΔR between generated parton and reconstructed jet. The different source of jets are shown in the left-hand plot, the two jets assigned to the hadronically decaying W boson and the two jets assigned to the top quarks beside a W boson. The right-hand plot shows this distribution in different intervals of jet p_T for the third jet assigned to the hadronic top quark.

If the reconstructed object is a muon the same method of minimizing the geometrical distance between generated and reconstructed muon is applied. The corresponding distribution is illustrated in the left-hand plot of Figure 5.9. If ΔR is below 0.01 the reconstructed muon is considered to be matched to a generated muon. In case the reconstructed object is an electron a different method is used which is based on a comparison of inner detector hits between generated and reconstructed tracks [85]. By means of a hit by hit matching, a probability is calculated to define which Monte Carlo particle fits best to a reconstructed track. The right-hand plot in Figure 5.9 shows the distribution of this matching probability. If this quantity exceeds 0.9 the reconstructed electron is referred as matched to a generated electron.

After the association of partons and leptons to final state objects it is now possible to decide if a composite particle is correctly reconstructed or not. A hadronically decaying W boson is referred to as correctly reconstructed if both of its jets are matched to generated partons coming from the same generated W boson. The hadronically decaying top quark is correctly reconstructed if the hadronic W boson is correctly reconstructed and the third jet is matched to a generated parton and both originate from the same generated top quark. In this study a reconstructed hadronic top quark candidate is also correctly reconstructed if all of its three jets can be matched to the same generated top quark. With this definition it is possible to have more than one correctly reconstructed hadronic top quark in an event. But since this analysis is only interested in the top quark four-vector, which is the same among those candidates, this assumption is perfectly valid.

The leptonically decaying W boson is referred to as correctly reconstructed if the lepton is matched to a generated lepton and is originating from a generated W boson. The

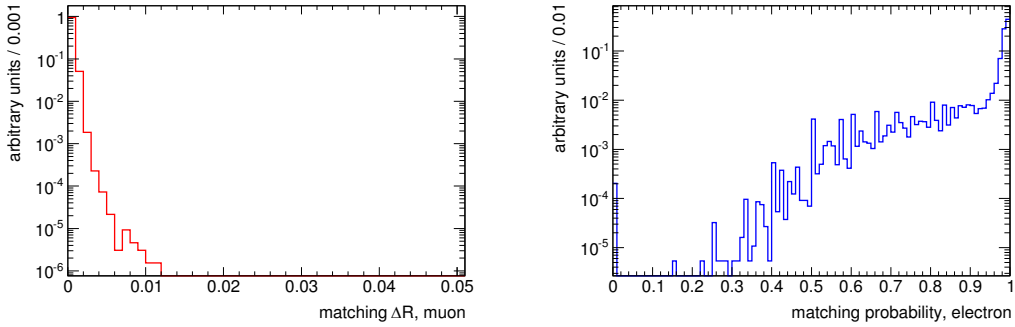


Figure 5.9: Minimal distance in ΔR between generated and reconstructed muons (left-hand plot) and matching probability between generated and reconstructed electrons (right-hand plot).

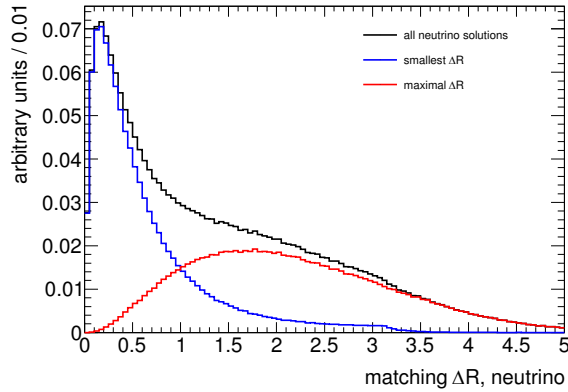


Figure 5.10: Minimal distance in ΔR between generated neutrino and the two calculated neutrino solutions. The red line denotes the smaller and the blue line the greater distance.

distribution of the smallest and maximal distance in ΔR between the two calculated neutrino solutions and the generated neutrino four-vector is illustrated in Figure 5.10. No unambiguous cut value can be found. Hence, no attempt is made to decide which neutrino solution is more correct than the other. Finally, the leptonically decaying top quark is correctly reconstructed if the leptonic W boson is correctly reconstructed and the third jet is matched to a generated parton and both originate from the same generated top quark.

5.3.3 Event selection

The definition of reconstructed objects like electrons, muons and jets as well as the reconstruction of top anti-top pairs has been discussed above. Basic event selection criteria are applied and summarized in the following:

- the event must contain exactly one lepton (electron or muon) with $p_T > 20$ GeV and $|\eta| < 2.5$
- missing transverse energy $E_T^{\text{miss}} > 20$ GeV

- at least 4 jets with $p_T > 20$ GeV and $|\eta| < 5.0$
- reconstructed W boson mass: $|m_W - 80.4 \text{ GeV}| < 60 \text{ GeV}$
- reconstructed top quark mass: $|m_{top} - 172.5 \text{ GeV}| < 80 \text{ GeV}$
- the mass cut on the leptonically decaying top quark can only be applied if a neutrino solution could be found
- $|\eta| < 2.5$ for jets assigned to the top quarks

Only events fulfilling these basic cuts with at least one reconstructed $t\bar{t}$ candidate are retained for further analysis. Table 5.3 summarizes the number of remaining events and the average number of reconstructed $t\bar{t}$ candidates per event after applying different cuts. The event numbers are given for $\tan\beta = 30$ and an integrated luminosity of 30 fb^{-1} .

Given the large number of $t\bar{t}$ candidates per event and the large physics background contribution it is clear that apart from the basic event selection a number of additional criteria have to be defined to increase the purity of the sample.

In a first step, several cuts are applied to efficiently reduce the combinatorial background. They are based on several kinematic distributions and are illustrated in Figure 5.11 for the $t\bar{t}$ sample. These distributions look very similar for the different values of the charged Higgs boson mass. The additional cuts are summarized in the following:

- jet $p_T > 30$ GeV for all jets assigned to the hadronic W boson candidate and $p_T > 40$ GeV for at least one of them
- jet $p_T > 40$ GeV for the jets assigned to the top quarks
- reconstructed W boson mass: $|m_W - 80.4 \text{ GeV}| < 30 \text{ GeV}$
- reconstructed top quark mass: $|m_{top} - 172.5 \text{ GeV}| < 60 \text{ GeV}$

In addition, a variable X is defined as the energy difference of the W boson and the b quark in the top quark rest frame [64]:

$$X = E_W^* - E_b^* = \frac{m_W^2 - m_b^2}{m_{top}}. \quad (5.4)$$

Only events fulfilling $X = (37.5 \pm 21) \text{ GeV}$ are retained. The mass cut on the leptonically decaying top quark and on the leptonic X can only be applied if a neutrino solution could be found.

The boundary values of the three latter cuts correspond to approximately three standard deviations of the respective distribution matched to generator level. The values are obtained by a Gaussian fit around its core region.

The impact of the additional cuts on the selection yields are also shown in Table 5.3. For samples containing true semileptonic $t\bar{t}$ events ($t\bar{t}$, $t\bar{t}b\bar{b}$ and the H^+ samples) the event selection efficiency is in the order of 10% while the contribution of several backgrounds

Sample	$t\bar{t}$	$t\bar{t}b\bar{b}$	single top	$Wb\bar{b}$	W + jets	$m_{H^+} = 250$ GeV	$m_{H^+} = 600$ GeV
No cuts applied							
Number of expected events	$8240(11) \cdot 10^3$	$66.0(1) \cdot 10^3$	$30.36(7) \cdot 10^6$	$9.31(4) \cdot 10^6$	$65.5 \cdot 10^{12}$	6780(60)	338(1)
Basic cuts							
Number of expected events	$1.89(1) \cdot 10^6$	$13.8(1) \cdot 10^3$	$105(4) \cdot 10^3$	$34(2) \cdot 10^3$	$2.21(2) \cdot 10^6$	1592(30)	81.0(4)
Average number of $t\bar{t}$ candidates per event	70	140	30	30	20	130	140
Additional cuts							
Number of expected events	$689(3) \cdot 10^3$	7220(30)	$20(2) \cdot 10^3$	5110(90)	$192(5) \cdot 10^3$	800(20)	44.3(3)
Average number of $t\bar{t}$ candidates per event	8	14	6	5	5	14	16

Table 5.3: Selection yields for $\tan\beta = 30$ and an integrated luminosity of 30 fb^{-1} . The numbers given in parentheses denote the statistical uncertainties on the last digits including the uncertainties arising from the available amount of Monte Carlo statistics.

5 Analysis

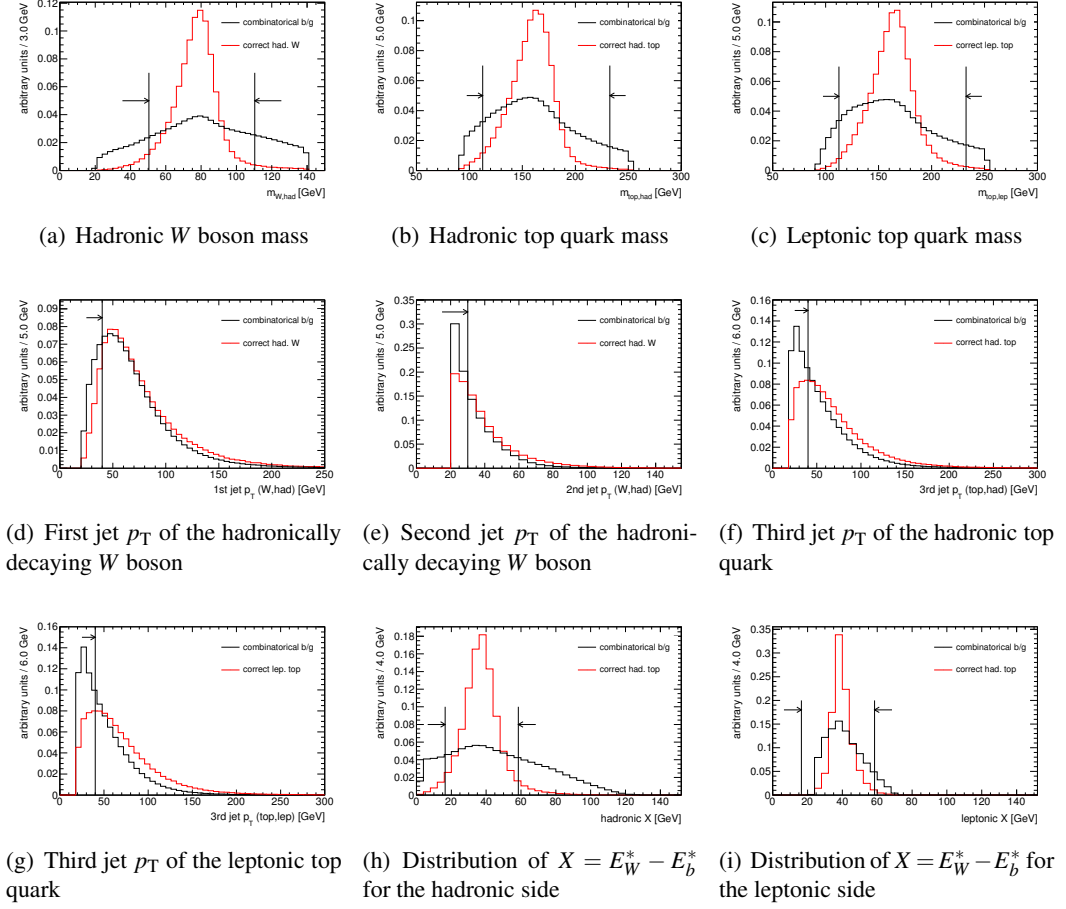


Figure 5.11: Normalized distribution of kinematic variables of the $t\bar{t}$ sample used for event selection. The black histogram denotes the pure combinatorial background and the red histogram shows the correctly reconstructed quantity. The vertical lines correspond to the bounds of the additional cuts described in the text.

is greatly reduced. After cuts, about 10 semileptonic top anti-top candidates can be reconstructed per event on average. No b -tag criteria is applied so far. In Figure 5.12 the number of additional jets not associated to one of the $t\bar{t}$ candidates is shown. At least one of these jets is necessary to reconstruct of a charged Higgs boson. It can be seen that even after choosing one $t\bar{t}$ pair in an event this will lead to combinatorial background in the signal process.

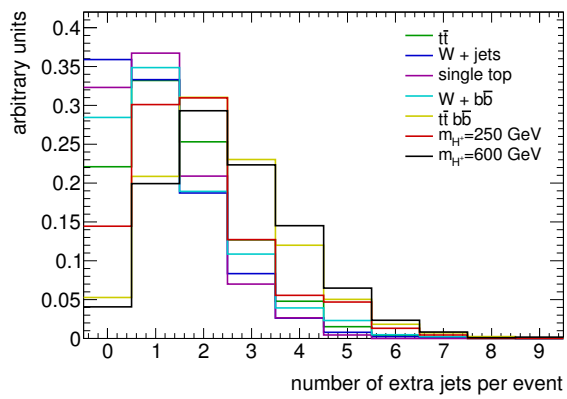


Figure 5.12: Normalized distribution of the number of extra jets per event which are not used to reconstruct a $t\bar{t}$ candidate. The additional cuts are applied and only extra jets with transverse momentum $p_T > 20$ GeV are considered.

5.4 Kinematic fit with constraints

In the previous Section it has been described how semileptonic $t\bar{t}$ pairs are efficiently reconstructed. In general, more than one pair is selected per event due to the ambiguity of choosing the correct jet combination in the reconstruction of the decay tree. For further analysis only one pair has to be selected in order to reconstruct a charged Higgs boson. The aim of the following Section is to develop a method which gives a high association efficiency for $t\bar{t}$ events with correctly assigned top pairs.

For this purpose several properties of the $t\bar{t}$ event topology, like the W boson or top quark mass, can be exploited while taking into account resolution effects of the reconstructed objects. One method is to apply a kinematic fit with appropriate constraints. The χ^2 probability of such a fit is an event observable which can be used to differentiate between true and wrong hypotheses.

The next Sections will give an overview about kinematic fits in general and the mathematics of the general non-linear least square fit technique using Lagrange multipliers.

5.4.1 Introduction

The application of constraint kinematic fitting methods in particle physics has a very long history. In particular at LEP-2 and at B -factories this analysis technique became a frequently used tool for the reconstruction of entire or partial event topologies. Due to the accurate measurement of the incoming electron and positron momenta at e^+e^- colliders the initial state is known. Applying constraints of energy and momentum conservation plus many of the stable particles as constraints has usually led to significantly improved estimators of the kinematics of the underlying event processes.

Although at proton colliders, like the LHC, these powerful constraints between initial and final state kinematics are not available and only $\sum \vec{p}_T = 0$ can be used since only partons take part in the hard scattering, the use of constraint kinematic fitting tools is still possible.

5.4.2 Fitting technique: non-linear least square fits with constraints

A physical problem in many cases consists of measured quantities as particles' four-vectors and unmeasured values, e.g. energy and momentum of missing particles like neutrinos. Often a certain hypothesis of the event topology can be imposed. Constraints like energy and momentum conservation can be used to vary the measured values within their errors to fulfill these requirements. This procedure is usually called a *kinematic fit*, which is done by a least square method [86].

Introduction

A general problem with n measured parameters \vec{y} , p unmeasured parameters \vec{a} and m constraints \vec{f} has to be solved. The following requirements will be fulfilled for the true param-

eters \vec{a} and \vec{y} :

$$\begin{aligned}
 f_1(\bar{a}_1, \bar{a}_2, \dots, \bar{a}_p, \bar{y}_1, \bar{y}_2, \dots, \bar{y}_n) &= 0 \\
 f_2(\bar{a}_1, \bar{a}_2, \dots, \bar{a}_p, \bar{y}_1, \bar{y}_2, \dots, \bar{y}_n) &= 0 \\
 &\vdots \\
 f_m(\bar{a}_1, \bar{a}_2, \dots, \bar{a}_p, \bar{y}_1, \bar{y}_2, \dots, \bar{y}_n) &= 0.
 \end{aligned} \tag{5.5}$$

Due to uncertainties, the measured values \vec{y} will not solve these conditions so that corrections $\Delta\vec{y}$ have to be applied. Eventually, the sum $\vec{y}' = \vec{y} + \Delta\vec{y}$ will fulfill the given constraints. The corrections are determined by minimizing the squared sum

$$S(\vec{y}) = \Delta\vec{y}^T \mathcal{V}^{-1} \Delta\vec{y} \tag{5.6}$$

with \mathcal{V} being the covariance matrix of the measured parameters. The matrix elements are defined by $\mathcal{V}_{ij} = \text{cov}(y_i, y_j) = E[(y_i - \mu_i)(y_j - \mu_j)]$, with $\mu_i = E[y_i]$ being the expectation value of the i -th measured parameter. The diagonal elements of \mathcal{V} contain the variances $\text{var}(y_i) = \sigma_i^2$ of the measured parameters.

A general approach to determine local extrema of functions with multiple variables incorporating constraints is the method of *Lagrange Multipliers*. It introduces m additional parameters λ_k , the Lagrange Multipliers, one for each constraint. A solution of the problem can be found by searching for a minimum of the function

$$L(\vec{y}, \vec{a}, \vec{\lambda}) = S(\vec{y}) + 2 \sum_{k=1}^m \lambda_k f_k(\vec{y}, \vec{a}) \tag{5.7}$$

with respect to all parameters \vec{y} , \vec{a} and $\vec{\lambda}$. It is equivalent to the condition for a local minimum of $S(\vec{y})$ under the constraint $f_k(\vec{y}, \vec{a}) = 0$.

If the constraints f_k are linear the solution can be calculated immediately. Otherwise it has to be found iteratively by linearizing the problem in every iteration.

Linearization

A linearized form of the constraints as defined in Eq. 5.5 can be written as

$$\begin{aligned}
 f_k(\vec{y}', \vec{a}') &\approx f(\vec{y}^*, \vec{a}^*) + \sum_{j=1}^p \frac{\partial f_k}{\partial a_j} \cdot (\Delta a_j - \Delta a_j^*) \\
 &+ \sum_{i=1}^n \frac{\partial f_k}{\partial y_i} \cdot (\Delta y_i - \Delta y_i^*), \approx 0
 \end{aligned} \tag{5.8}$$

where $\vec{y}(\vec{a})$ contains the start values of the measured (unmeasured) parameters, $\vec{y}^*(\vec{a}^*)$ contains the values of the measured (unmeasured) parameters after the previous iteration, and $\vec{y}'(\vec{a}')$ contains the values of the measured (unmeasured) parameters after current iteration.

All functional values and derivatives are calculated at $\vec{y}^* = \vec{y} + \Delta\vec{y}^*$ and $\vec{a}^* = \vec{a} + \Delta\vec{a}^*$. The difference of the start values and the next iteration is given by $\vec{y}' = \vec{y} + \Delta\vec{y}$ and $\vec{a}' = \vec{a} + \Delta\vec{a}$.

Rewriting Eq. 5.8 in matrix notation gives

$$\vec{f}^* + \mathcal{A}(\Delta\vec{a} - \Delta\vec{a}^*) + \mathcal{B}(\Delta\vec{y} - \Delta\vec{y}^*) \approx 0, \quad (5.9)$$

or

$$\mathcal{A}\Delta\vec{a} + \mathcal{B}\Delta\vec{y} - \vec{c} = 0 \quad \text{with} \quad \vec{c} = \mathcal{A}\Delta\vec{a}^* + \mathcal{B}\Delta\vec{y}^* - \vec{f}^*. \quad (5.10)$$

The vector \vec{c} in Eq. 5.10 is a constant vector for iteration n which only depends on quantities of the previous iteration ($n - 1$). In Eq. 5.9 and 5.10 the matrices \mathcal{A} and \mathcal{B} are defined as follows:

$$\mathcal{A} = \frac{\partial \vec{f}}{\partial \vec{a}} \quad \mathcal{B} = \frac{\partial \vec{f}}{\partial \vec{y}}. \quad (5.11)$$

The derivatives of the constraints with respect to the parameters \vec{a} and \vec{y} analyzed in matrix form:

$$\mathcal{A} = \begin{pmatrix} \partial f_1/\partial a_1 & \partial f_1/\partial a_2 & \dots & \partial f_1/\partial a_p \\ \partial f_2/\partial a_1 & \partial f_2/\partial a_2 & \dots & \partial f_2/\partial a_p \\ \vdots & & & \\ \partial f_m/\partial a_1 & \partial f_m/\partial a_2 & \dots & \partial f_m/\partial a_p \end{pmatrix}, \quad (5.12)$$

$$\mathcal{B} = \begin{pmatrix} \partial f_1/\partial y_1 & \partial f_1/\partial y_2 & \dots & \partial f_1/\partial y_n \\ \partial f_2/\partial y_1 & \partial f_2/\partial y_2 & \dots & \partial f_2/\partial y_n \\ \vdots & & & \\ \partial f_m/\partial y_1 & \partial f_m/\partial y_2 & \dots & \partial f_m/\partial y_n \end{pmatrix}, \quad (5.13)$$

$$\vec{f}^* = \begin{pmatrix} f_1(\vec{a}^*, \vec{y}^*) \\ f_2(\vec{a}^*, \vec{y}^*) \\ \vdots \\ f_m(\vec{a}^*, \vec{y}^*) \end{pmatrix}. \quad (5.14)$$

In practice the constraints often depend directly on the four-vector components ($\vec{P} = (\vec{p}, E)$). By using the chain rule for derivatives, $\partial \vec{f}/\partial \vec{y} = \partial \vec{f}/\partial \vec{P} \cdot \partial \vec{P}/\partial \vec{y}$, the calculation can be simplified.

In this new notation the likelihood to be minimized is given by:

$$L = \Delta\vec{y}^T \mathcal{V}^{-1} \Delta\vec{y} + 2\lambda^T (\mathcal{A}\Delta\vec{a} + \mathcal{B}\Delta\vec{y} - \vec{c}). \quad (5.15)$$

The condition for an extremum of L is obtained by differentiation w.r.t. \vec{y}, \vec{a} and $\vec{\lambda}$:

$$\begin{aligned} \mathcal{V}^{-1} \Delta\vec{y} + \mathcal{B}^T \vec{\lambda} &= 0 \\ \mathcal{A}^T \vec{\lambda} &= 0 \\ \mathcal{B}\Delta\vec{y} + \mathcal{A}\Delta\vec{a} &= \vec{c} \end{aligned} \quad (5.16)$$

resulting in a coupled system of $n + p + m$ differential equations that need to be solved for the unknown values of $\Delta\vec{y}, \Delta\vec{a}$ and $\vec{\lambda}$.

Solution

The system of coupled differential equations defined in Eq. 5.16 can be written in only one equation with partitioned matrices:

$$\begin{pmatrix} \mathcal{V}^{-1} & 0 & \mathcal{B}^T \\ 0 & 0 & \mathcal{A}^T \\ \mathcal{B} & \mathcal{A} & 0 \end{pmatrix} \begin{pmatrix} \Delta \vec{y} \\ \Delta \vec{a} \\ \lambda \end{pmatrix} = \begin{pmatrix} 0 \\ 0 \\ c \end{pmatrix}. \quad (5.17)$$

In order to find a solution the inverse of the matrix given in Eq. 5.17 has to be calculated. Writing its inverse matrix in a partitioned form,

$$\begin{pmatrix} \mathcal{V}^{-1} & 0 & \mathcal{B}^T \\ 0 & 0 & \mathcal{A}^T \\ \mathcal{B} & \mathcal{A} & 0 \end{pmatrix}^{-1} = \begin{pmatrix} C_{11} & C_{21}^T & C_{31}^T \\ C_{21} & C_{22} & C_{32}^T \\ C_{31} & C_{32} & C_{33} \end{pmatrix} \quad (5.18)$$

and using the abbreviations

$$\mathcal{V}_{\mathcal{B}} = (\mathcal{B}\mathcal{V}\mathcal{B}^T)^{-1} \quad \text{and} \quad \mathcal{V}_{\mathcal{A}} = (\mathcal{A}^T\mathcal{V}_{\mathcal{B}}\mathcal{A}) \quad (5.19)$$

gives

$$C_{11} = \mathcal{V} - \mathcal{V}\mathcal{B}^T\mathcal{V}_{\mathcal{B}}\mathcal{B}\mathcal{V} \quad (5.20)$$

$$+ \mathcal{V}\mathcal{B}^T\mathcal{V}_{\mathcal{B}}\mathcal{A}\mathcal{V}_{\mathcal{A}}^{-1}\mathcal{A}^T\mathcal{V}_{\mathcal{B}}\mathcal{B}\mathcal{V} \quad (5.21)$$

$$C_{21} = -\mathcal{V}_{\mathcal{A}}^{-1}\mathcal{A}^T\mathcal{V}_{\mathcal{B}}\mathcal{B}\mathcal{V} \quad (5.22)$$

$$C_{22} = \mathcal{V}_{\mathcal{A}}^{-1} \quad (5.23)$$

$$C_{31} = \mathcal{V}_{\mathcal{B}}\mathcal{B}\mathcal{V} - \mathcal{V}_{\mathcal{B}}\mathcal{A}\mathcal{V}_{\mathcal{A}}^{-1}\mathcal{A}^T\mathcal{V}_{\mathcal{B}}\mathcal{B}\mathcal{V} \quad (5.24)$$

$$C_{32} = \mathcal{V}_{\mathcal{B}}\mathcal{A}\mathcal{V}_{\mathcal{A}}^{-1} \quad (5.25)$$

$$C_{33} = -\mathcal{V}_{\mathcal{B}} + \mathcal{V}_{\mathcal{B}}\mathcal{A}\mathcal{V}_{\mathcal{A}}^{-1}\mathcal{A}^T\mathcal{V}_{\mathcal{B}} \quad (5.26)$$

With this notation the corrections to the parameters are derived:

$$\Delta \vec{y} = C_{31}^T \vec{c} = (\mathcal{V}\mathcal{B}^T\mathcal{V}_{\mathcal{B}} - \mathcal{V}\mathcal{B}^T\mathcal{V}_{\mathcal{B}}\mathcal{A}\mathcal{V}_{\mathcal{A}}^{-1}\mathcal{A}^T\mathcal{V}_{\mathcal{B}}) \vec{c} \quad (5.27)$$

$$\Delta \vec{a} = C_{32}^T \vec{c} = (\mathcal{V}_{\mathcal{A}}^{-1}\mathcal{A}^T\mathcal{V}_{\mathcal{B}}) \vec{c} \quad (5.28)$$

$$\vec{\lambda} = C_{33} \vec{c} = (-\mathcal{V}_{\mathcal{B}} + \mathcal{V}_{\mathcal{B}}\mathcal{A}\mathcal{V}_{\mathcal{A}}^{-1}\mathcal{A}^T\mathcal{V}_{\mathcal{B}}) \vec{c} \quad (5.29)$$

The parameters for the next iteration step are obtained by $\vec{y}' = \vec{y} + \Delta \vec{y} = \vec{y} + C_{31}^T \vec{c}$.

The variance of the fitted parameters \vec{y}' can be calculated with error propagation from the covariance matrix of the measured parameters:

$$\mathcal{V}(\vec{y}') = \underbrace{(\mathcal{J} + C_{31}^T \frac{\partial \vec{c}}{\partial \vec{y}})}_{-\mathcal{B}} \mathcal{V}(\vec{y}) \quad (5.30)$$

$$= \underbrace{\mathcal{V} - \mathcal{V}\mathcal{B}^T\mathcal{V}_{\mathcal{B}}\mathcal{B}\mathcal{V} + \mathcal{V}\mathcal{B}^T\mathcal{V}_{\mathcal{B}}\mathcal{A}\mathcal{V}_{\mathcal{A}}^{-1}\mathcal{A}^T\mathcal{V}_{\mathcal{B}}\mathcal{B}\mathcal{V}}_{C_{11}}. \quad (5.31)$$

The combined covariance matrix for the fitted parameters eventually given by:

$$\mathcal{V} \left[\begin{pmatrix} \vec{y}' \\ \vec{a}' \\ \vec{\lambda}' \end{pmatrix} \right] = \begin{pmatrix} C_{11} & C_{21}^T & 0 \\ C_{21} & C_{22} & 0 \\ 0 & 0 & -C_{33} \end{pmatrix}. \quad (5.32)$$

The iteration is repeated until certain convergence criteria are met guaranteeing that the squared sum S has reached a minimum and all constraints are fulfilled. The convergence criteria is defined by:

$$\frac{S(n-1) - S(n)}{ndf} < \varepsilon_S \quad \text{and} \quad \sum_{k=1}^m f_k^{(n)}(\vec{y}, \vec{a}) < \varepsilon_F \quad (5.33)$$

where n denotes the number of iterations and ndf defines the number of degrees of freedom which is given by difference of the number of constraints and the number of unmeasured parameters,

$$ndf = m - p. \quad (5.34)$$

The parameter ε_S defines the size of the allowed change of S from one iteration to the next. The precision by which the constraints have to be fulfilled is defined by the parameter ε_F .

Implementation

An iterative solution of the least square problem with non-linear constraints has been implemented in a dedicated *KinFitter* software package [87] during this study. This was performed together with J. E. Sundermann.

Several four-vector parametrization schemes of the particles to be fitted has been implemented. Constraints like energy and momentum conservation as well as mass constraints including finite width of instable particles are included. All features have been carefully tested with the help of Toy Monte Carlo. Details can be found in Reference [87]. Due to the object oriented design of *KinFitter* it is relatively easy to add new constraints or particle parametrization. The high flexibility of the fitting algorithm assures its application to many physical problems and decay topologies. The analytical nature of the procedure ensures high speed performance, as well as reliable convergences.

The *KinFitter* package is implemented into the ATLAS software framework but it has been taken care that it is also usable outside of this framework. A detailed user and installation guide can be found in Reference [88].

5.5 Kinematic fit of semileptonic top anti-top events

The input for the kinematic fit are the four jets and the lepton momentum together with the missing transverse energy as an estimate of the transverse component of the neutrino momentum. The longitudinal component of the neutrino enters the fit as unmeasured parameter.

5.5.1 Four-vector parametrization

The momentum vector \vec{p} of the reconstructed objects is parametrized in coordinates with the free parameters p_T , η , and ϕ :

$$\vec{p} = p_T \begin{pmatrix} \cos \phi \\ \sin \phi \\ \sinh \eta \end{pmatrix}. \quad (5.35)$$

All objects are assumed to be massless. This is a very appropriate assumption in the energy range considered. Hence, the energy in this parametrization is simply

$$E = \sqrt{|\vec{p}|^2}. \quad (5.36)$$

For all objects the fitted quantities are the absolute values of the components defined in Eq. 5.35. The only exception is the jet transverse momentum. Here, the relative component of p_T is fitted, i.e. if p_T^m is the measured transverse momentum and a is the parameter entering the kinematic fit then the fitted transverse momentum is $p_T^f = ap_T^m$. The reason of choosing different parametrization of the fitted objects is explained in the following.

The function to be minimized by the fit is given in Eq. 5.7. If the constraints are fulfilled, which is e.g. the case if a local minimum is found, the likelihood function is reduced to the standard χ^2 function. Such a χ^2 fit is a commonly used fitting technique in physics. It assumes Gaussian distributed uncertainties of the parameters which enter the fit via a covariance matrix. Only if this condition is fulfilled, the fit result can be properly interpreted. In the minimum, the χ^2 value itself is a measure of the goodness of this fit and the so-called *PULL*-distributions of the fitted parameters are standard normal distributed. This very useful behavior is e.g. exploited in the various tests of the *KinFitter* package.

Therefore, it is preferable that a parametrization is chosen in a way that all parameter uncertainties are Gaussian distributed. But it has to be pointed out that this does not mean, if this prerequisite is not fulfilled, that the fit does not work or does not converge. Only the interpretation of the fit result is not straight-forward anymore.

In addition, the resolution of a parameter may depend on other or the value of the same parameter. Hence, it is also favorable to at least obtain the uncertainties in intervals of the parameters they depend on resulting in so-called parametrized resolution functions. Otherwise all $t\bar{t}$ combinations will get the same weight during the kinematic fit but they may be measured with different precisions. The resolution of momentum and direction strongly depend on their measured transverse momentum and detector region. The resolution is worse in regions of large $|\eta|$ due to an increase of material compared to the central region of the detector. Other effects like dead material or transition regions within the ATLAS detector also have an impact on the resolution. The measured precision on p_T is mainly given by the resolution of the detector components involved used to measure energy, momentum and direction.

The resolutions of p_T , η , and ϕ of jets and leptons are obtained in intervals of the measured transverse momentum and pseudo-rapidity. It is assumed that all measurements are

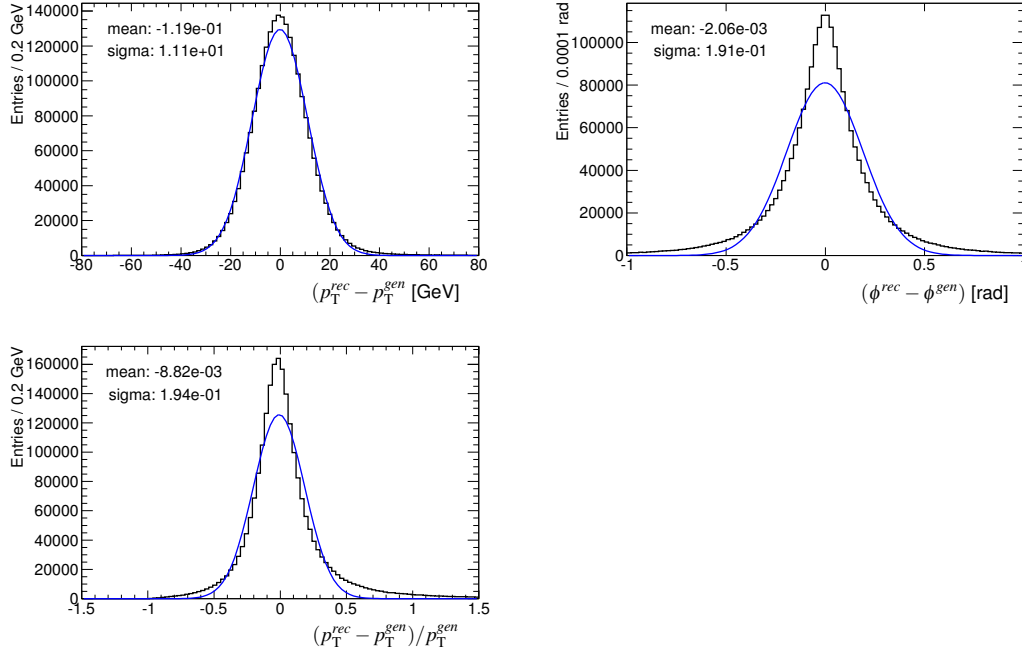


Figure 5.13: Distribution of the resolution of p_T (left) and ϕ (right) of the **missing transverse energy**. The upper row shows the resolution of their absolute values and the lower row of their relative p_T , respectively. The blue lines shows the results of Gaussian fits and the obtained means and standard deviations are given. The fit is applied over the whole range of the histogram.

symmetric in ϕ . For the missing transverse energy only p_T and ϕ dependence is considered. Therefore, these quantities are compared between the reconstructed and generated object. The matching algorithm is described in Section 5.3.2. The resulting distribution is fitted with a Gaussian function and the mean and standard deviation, σ , of the fit is extracted. For the missing transverse energy and jets stemming from b quarks the integrated resolution, i.e. the resolution not obtained in specific intervals of the parameters, of the absolute components and relative p_T are shown in Figure 5.13 and 5.14. For the electron, muon and light jet they are illustrated in Appendix B.

The resolution of the momentum vector components is dominated by the transverse momentum except for E_T^{miss} , where the angular contribution is of the same order of magnitude. Angles of leptons and jets are usually well measured such that uncertainties on p_T and E_T dominates the uncertainties on the reconstructed W boson and top quark mass. As already mentioned, it is preferable that the uncertainties are Gaussian distributed, in particular for p_T . For this reason, the leptons and neutrinos are parametrized by the absolute values of the components in Eq. 5.35 and the jets p_T by the relative component. But for jets the asymmetry is still quite pronounced for the relative p_T component and is larger for b -jets. This might be due to neutrinos coming from semileptonic hadron decays inside jets. These neutrinos carry away a fraction of the jet energy, introducing a systematic underestimation

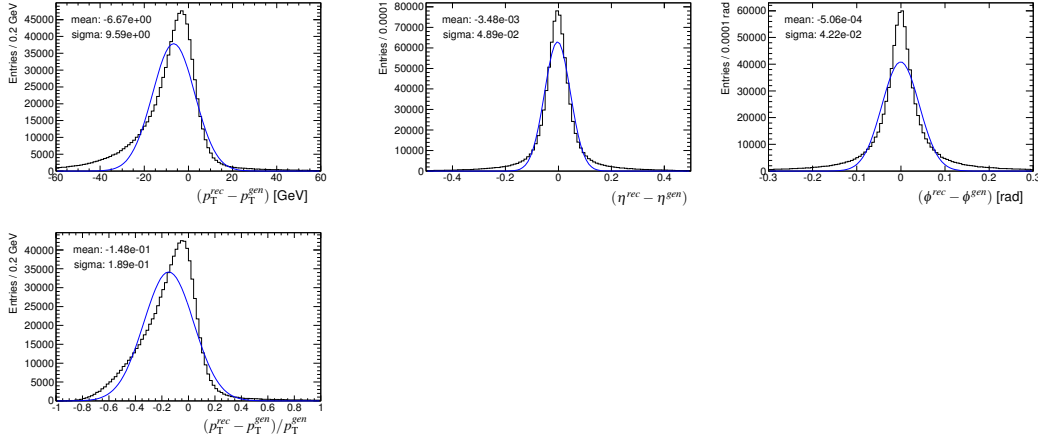


Figure 5.14: Distribution of the resolution of p_T (left), η (middle) and ϕ (right) of **b-jets**. The upper row shows the resolution of their absolute value and the lower row of their relative p_T , respectively. The blue lines shows the results of Gaussian fits which are applied over the whole range of the histograms and the obtained means and standard deviations are given.

of the energy of such jets. A neutrino from the semileptonically decaying b -hadron inside a jet carries over 10% of the total jet p_T [64]. Additional sources are possible since the jet energy calibration is only done to a so-called physics jets level where the jet energy is calibrated to match the energy of stable Monte Carlo jet particles and not to the parton level.

Mean and σ are illustrated in Figure 5.15 for the missing transverse energy. The asymmetry in the mean vs. p_T distribution of ϕ can not be explained. But the influence on the result of the kinematic fit should be negligible since the asymmetry is very small and the resolution of ϕ is at least one order of magnitude higher. For b -jets, means and σ 's together with their obtained uncertainty are shown in Figure 5.16 and 5.17. For the electron, muon and light jets they are shown in Appendix B. No significant asymmetry in the angular measurement can be determined.

The obtained means are used to correct the input parameters before they enter the kinematic fit. In case of jets, this corresponds to an jet energy correction to the parton level. This correction is found to be quite substantial and can be up to several tenth of % in case of the transverse momentum of b -jets. The accuracy of the jet energy scale is an important input for the kinematic fitting process, since it is assumed that the measured parameters are distributed symmetrically, i.e. without a systematic shift, around the true value.

The σ 's are used to fill the diagonal elements of the covariance matrix \mathcal{V} as defined in Eq. 5.6. Simply speaking, the kinematic fit is allowed to vary the parameters within these uncertainties to fulfill the given constraints. In case of the b -jet p_T the resolution is in the order of 20%. The correlations between angular and momentum measurement are found to be negligible. In addition, no correlations between parameters of different objects are introduced. Hence, all off-diagonal elements of the covariance matrix \mathcal{V} are set to zero.

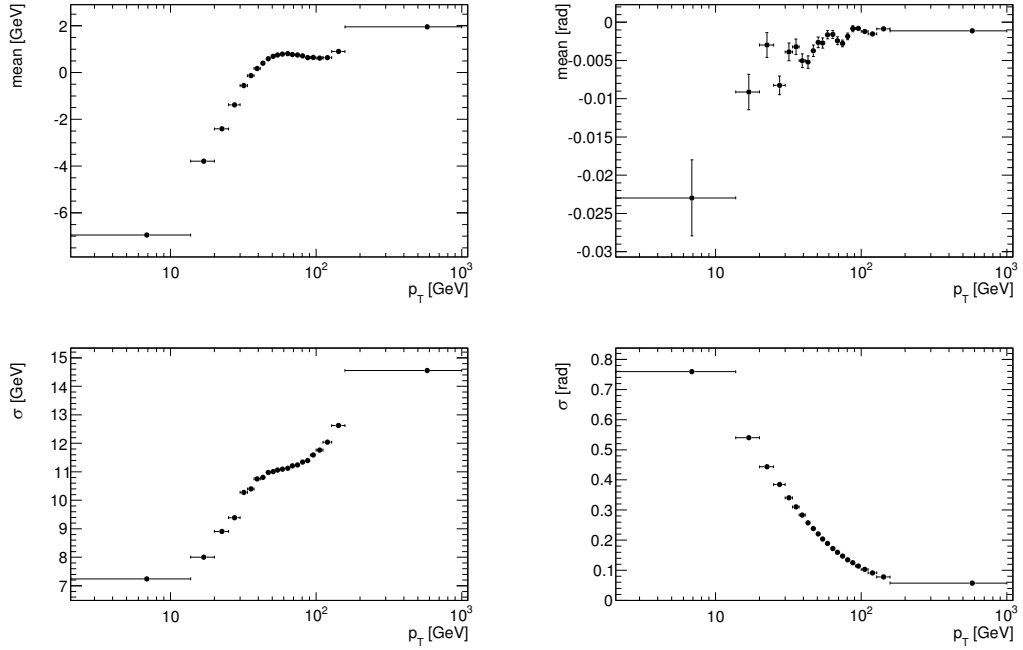


Figure 5.15: Distribution of mean and one standard deviation of the resolution of p_T (left) and ϕ (right) of the **missing transverse energy**. The values are obtained by a Gaussian fit in 22 intervals of the measured missing transverse momentum. The upper row shows mean and the lower row shows σ , respectively.

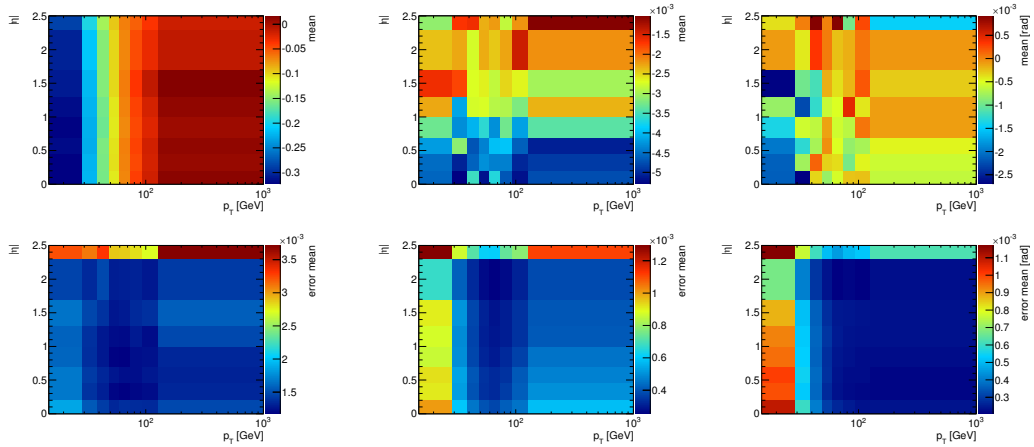


Figure 5.16: Distribution of the mean (upper row) and its statistical uncertainty (lower row) of the resolution of relative p_T (left), absolute η (middle) and ϕ (right) of **b-jets**. The values are obtained by a Gaussian fit in 8 intervals of the measured p_T and η , respectively.

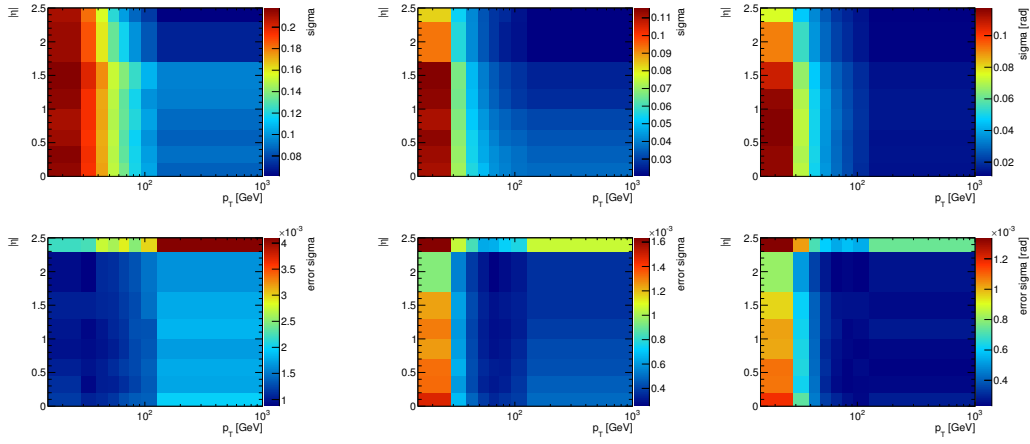


Figure 5.17: Distribution of the standard deviation (upper row) and its statistical uncertainty (lower row) of the resolution of relative p_T (left), absolute η (middle) and ϕ (right) of **b-jets**. The values are obtained by a Gaussian fit in 8 intervals of the measured p_T and η , respectively.

5.5.2 Constraints

Since one parameter remains unmeasured, the pseudo-rapidity of the neutrino, two constraints are necessary to have at least one degree of freedom within the fit. In this analysis, four mass constraints of fixed values are applied with 80.4 GeV for the two W bosons and 172.5 GeV for the two top quarks. Other constraints are possible and their impact is discussed in Appendix C.

5.5.3 Results

After the event selection presented in Section 5.3.3 a kinematic fit is applied on all remaining semileptonic $t\bar{t}$ candidates. At the beginning of the fitting procedure the values of the measured parameters are set to the corrected measured values and the start value of unmeasured longitudinal neutrino component is either set to zero or to one of the two neutrino solutions if Eq. 5.3 can be solved. After the fit, the $t\bar{t}$ candidate with the smallest χ^2 is selected.

The fitting algorithm does not always converge. This can even happen if the fit is applied on $t\bar{t}$ candidates that are correctly reconstructed, i.e. if they can be matched to a generated $t\bar{t}$ pair. In events with or without a neutrino solution the fit fails in about 1.7% or 33% of the cases, respectively. In these cases, the reconstructed and true values differ by more than several standard deviations or the hypothesis is not fulfilled. If e.g. more than one neutrino is present in the event than the assumption that the neutrino from the W boson decay is the only source of E_T^{miss} is obviously not fulfilled. In addition, highly mismeasured quantities appearing as non-Gaussian tails in the parameter resolution can also lead to a worse convergence behavior. In the following, events where the kinematic fit fails are no considered for further analysis but are taken into account within the performance estimators.

The distributions of the smallest χ^2 and the χ^2 probability ($\text{prob}(\chi^2)$) are depicted in Figure 5.18. If the selected top anti-top quark is correctly reconstructed, the χ^2 distribution tends to peak at small values with an expectation value of $nfd = 3$ (cf. Eq. 5.34) whereas wrong combinations have larger χ^2 values. A cut on the χ^2 value of the selected candidates will therefore lead to a pure sample. In addition, most wrong combinations peak at small values of the $\text{prob}(\chi^2)$ distribution. In an ideal world, the correctly reconstructed combinations should be distributed equally between zero and one. Discrepancies from this behavior are due to non-Gaussian tails in the parameter resolutions.

The performance of the kinematic fit is evaluated in terms of efficiency ε and purity p , defined as

$$\varepsilon = \frac{N_{\chi_{\min}^2}(\text{correct})}{N_{\text{all}}(\text{correct})} \quad \text{and} \quad p = \frac{N_{\chi_{\min}^2}(\text{correct})}{N_{\chi_{\min}^2}(\text{all})}. \quad (5.37)$$

Here, $N_{\chi_{\min}^2}(\text{correct})$ denotes the number of correctly reconstructed $t\bar{t}$ candidates having the minimum χ^2 in the event. $N_{\text{all}}(\text{correct})$ is the number of all events entering the kinematic fit that contain a correctly reconstructed $t\bar{t}$ candidate. Here, such candidates are also

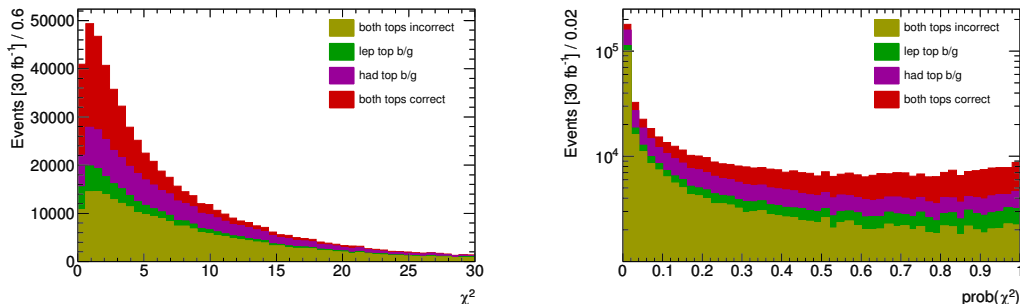


Figure 5.18: Minimum χ^2 (left) and $\text{prob}(\chi^2)$ (right) distribution of the $t\bar{t}$ sample. The colors in the stacked histograms represent different levels of matching to generator level objects. Red: both top quarks are correctly reconstructed; Purple: only leptonic top is correctly reconstructed; Green: only hadronic top is correctly reconstructed; Yellow: both top are not correctly reconstructed

counted where the kinematic fit fails. $N_{\chi_{min}^2}(\text{all})$ is the number of all events with a minimum χ^2 candidate regardless if this candidate is correctly reconstructed. In other words, ε is the fraction of events where the kinematic fit finds a correctly reconstructed candidate within those candidates containing at least one correctly reconstructed candidate. This definition reflects the true performance of the fitting algorithm and is disentangled from any cut efficiency applied beforehand as well as from any background contamination of the preselected sample. The purity is the fraction of events where a correctly reconstructed $t\bar{t}$ candidate is selected among all selected events.

Figures 5.19 and 5.20 show the purity versus efficiency, χ_{min}^2 and the number of expected events in 30 fb^{-1} for different cut values of the maximal allowed χ_{min}^2 . Only events from the $t\bar{t}$ sample are considered so far. The maximal efficiency for all events is in the order of 75%. This means that with the relatively loose additional cuts, introduced in Section 5.3.3, and without b -tagging, 75% of the correctly reconstructed $t\bar{t}$ candidates are found with a purity of about 28%. It can clearly be seen that a tighter cut on χ_{min}^2 leads to an increased purity while losing efficiency. In addition, the events are separated into events where a neutrino solution could be found or not. In the latter case the performance is worse due to less available information for the kinematic fit. But retaining such events leads to approximately 20% more $t\bar{t}$ candidates available for further analysis. The cut values leading to the same purity are very similar to each other in all cases.

For full evaluation of the fit performance various background events are included. The resulting χ_{min}^2 distribution is illustrated in Figure 5.21. Events containing a true top anti-top pair have very similar shape. A different distribution of the background events is clearly visible. They do not show such a distinct peaking behavior at small χ_{min}^2 values compared to signal events, as expected. Hence, a cut on the allowed χ_{min}^2 will lead to a larger separation of events containing a true $t\bar{t}$ pair and background events.

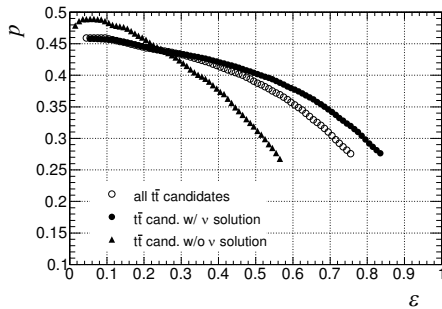


Figure 5.19: Purity versus efficiency of the kinematic fit for different cuts on χ^2_{min} for the $t\bar{t}$ sample. The filled circles represent $t\bar{t}$ sample events where a neutrino solution could be found and the filled triangles where not. For the events denoted by open circles no such distinction is made.

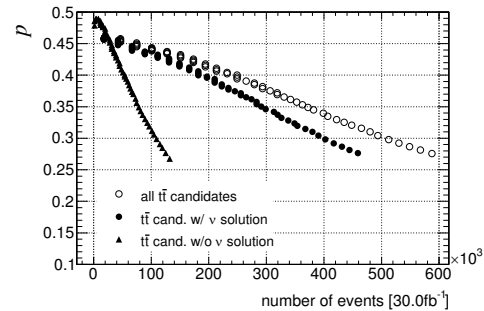
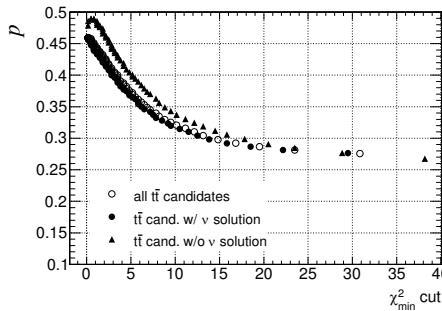


Figure 5.20: The left plot shows purity versus the χ^2_{min} cut value and the right plot shows purity versus number of expected events for an integrated luminosity of 30 fb^{-1} for different cuts on χ^2_{min} . Both plots contain only events from the $t\bar{t}$ sample. The filled circles represent events where a neutrino solution could be found and the filled triangles where not. For the events denoted by open circles no such distinction is made.

Including background leads to a decreased purity of about 5% for high efficiencies and of about 3% for lower efficiencies. Figure 5.22 shows the purity versus efficiency, χ^2_{min} and the number of expected events in 30 fb^{-1} for different cut values of the maximal allowed χ^2_{min} . In addition, the performance is compared to b -tagged $t\bar{t}$ pairs with 60% tagging efficiency. Applying b -tagging increases purity and efficiency by approximately a factor of two and by 5%, respectively. Such an increase in purity could not be gained by restricting χ^2_{min} alone. But, of course, the number of remaining events is reduced when applying b -tagging. When b -tagging is applied, the number of background events is greatly reduced to a nearly negligible level. This can e.g. be seen in the distribution of the reconstructed invariant masses of the top quarks illustrated in Figure 5.23. Here, the masses of the hadronically and leptonically decaying top quark are shown in a stacked histogram with and without background. It can be seen that the main contribution to the impurity is due to combinatorial background.

Various studies with different options of the kinematic fit, e.g. unbinned resolution func-

5.5 Kinematic fit of semileptonic top anti-top events

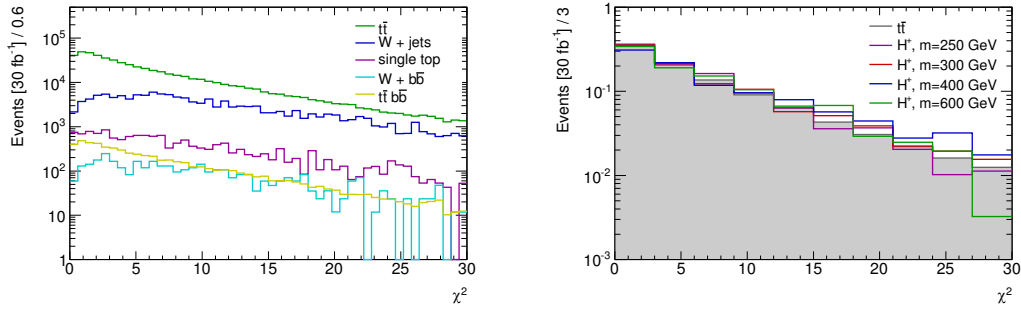


Figure 5.21: Minimum χ^2 distribution. Left: $t\bar{t}$ and various background samples for an integrated luminosity of 30 fb^{-1} . Right: Normalized distribution for $t\bar{t}$ and four charged Higgs boson mass samples. No statistical uncertainties are shown but the shapes of the distributions are in good agreement to each other.

tions and different constraints, and an alternative approach in selecting one $t\bar{t}$ candidate, are presented and discussed in Appendix C. It turns out that fit configuration presented here are the most performing ones in terms of efficiency and purity. Therefore, they are used for the reconstruction of a charged Higgs boson.

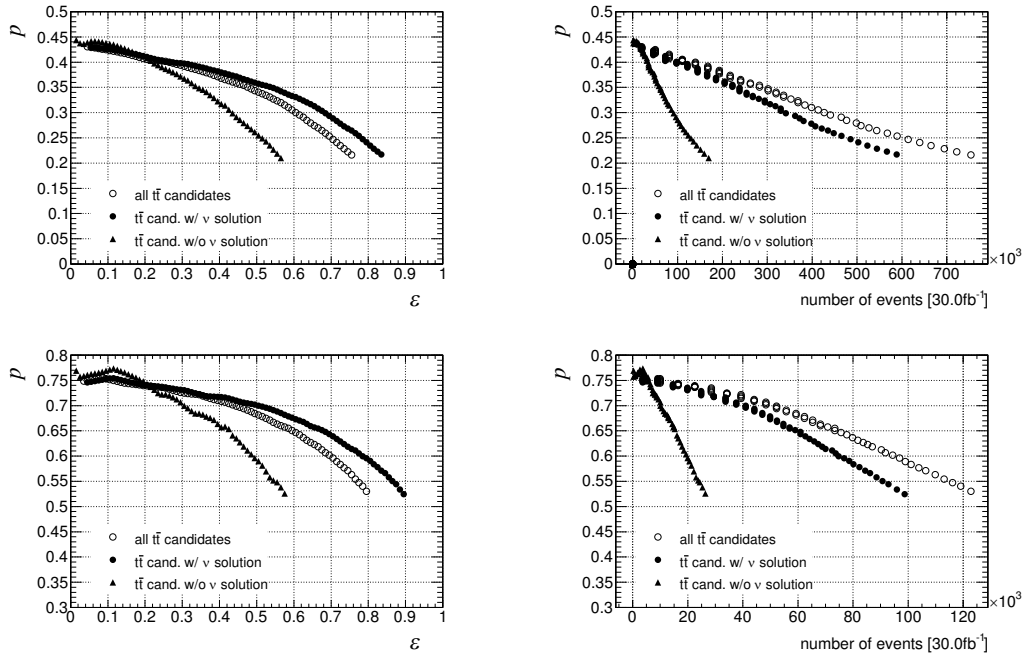


Figure 5.22: The left plots show purity versus efficiency and the right plots purity versus number of expected events for an integrated luminosity of 30fb^{-1} for different cuts on χ^2_{min} . The upper row is without and the lower row is with b -tagging ($\epsilon_b = 60\%$) applied. The plots contain $t\bar{t}$ + background events. The filled circles represents events where a neutrino solution could be found and the filled triangles where not. For the events denoted by open circles no such distinction is made.

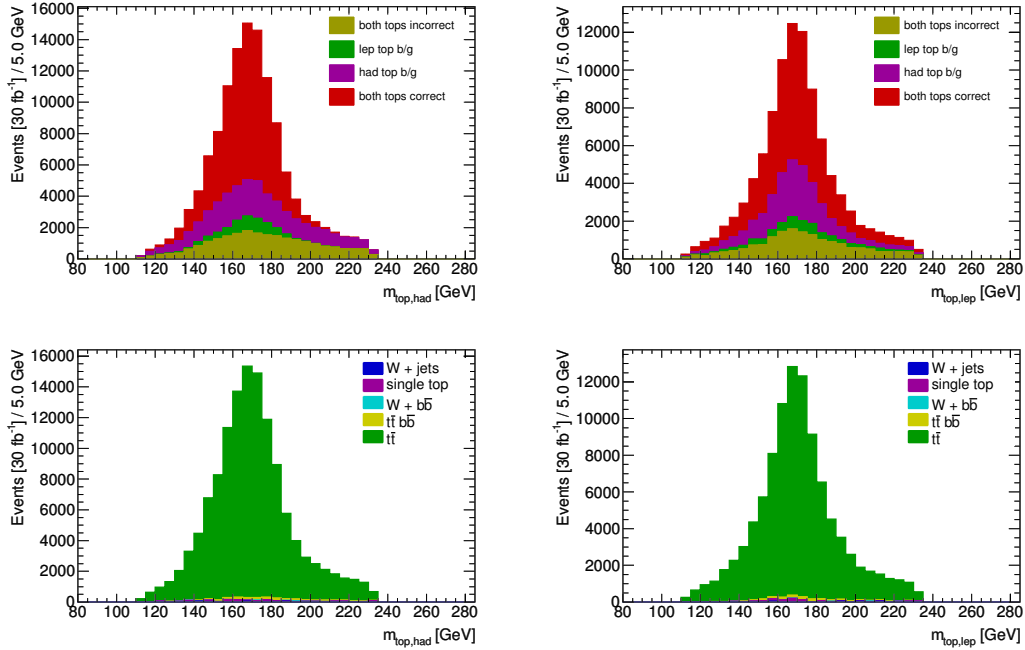


Figure 5.23: Reconstructed invariant masses of the hadronically (left) and leptonically (right) decaying top quark of the χ_{min}^2 candidate. Additional selection cuts and b -tagging with $\varepsilon_b = 60\%$ are applied. The upper row shows only events from the $t\bar{t}$ sample. For the plots in the lower row also various background samples are included. The events are scaled to an integrated luminosity of 30 fb^{-1} . The colors represent different levels of matching to generator level objects. Red: both top quarks are correctly reconstructed; Purple: only leptonic top is correctly reconstructed; Green: only hadronic top is correctly reconstructed; Yellow: both top are not correctly reconstructed

5.6 Reconstruction of charged Higgs bosons

In Sections 5.3 and 5.5 it has been presented how semileptonically decaying top anti-top quarks are reconstructed and one of the pairs is efficiently selected per event by applying a kinematic fit. In the following, only $t\bar{t}$ pairs fulfilling $\text{prob}(\chi^2) > 10^{-3}$ are retained for further analysis. This cut removes a large fraction of Standard Model background as well as correctly reconstructed but mismeasured $t\bar{t}$ candidates. In addition, the mass cuts for the reconstructed W boson and the top quarks are tightened and symmetrized around the reconstructed invariant masses of correctly reconstructed candidates (cf. Figure 5.11). Both cuts reduce the combinatorial and physical $t\bar{t}$ background with only little influence on the signal.

The cuts applied after kinematic fitting are summarized in the following:

- reconstructed W boson mass: $|m_W - 75 \text{ GeV}| < 25 \text{ GeV}$
- reconstructed top quark mass: $|m_{top} - 160 \text{ GeV}| < 40 \text{ GeV}$
- $\text{prob}(\chi^2) > 10^{-3}$

In order to reconstruct a charged Higgs boson in the process $H^+ \rightarrow t\bar{b}$ all of the remaining jets lying fulfilling $|\eta| < 5.0$ are paired with both of the selected top quarks in each event. The normalized mass distributions for correctly reconstructed combinations are shown in Figure 5.24 for four different charged Higgs boson masses. Here, no distinction between hadronic and leptonic H^+ decay mode is made. The four mass peaks are clearly visible. They get broader with increasing mass which additionally complicates the signal detection. The resolution of the reconstructed mass distribution is approximately 10% and 20% of the H^+ mass for $m_{H^+} = 250 \text{ GeV}$ and 600 GeV , respectively. This is a factor three to four more than the width of the generated H^+ mass. Furthermore, the mean values are slightly shifted to smaller values compared to the nominal masses. This is a consequence of a non-optimal jet-parton energy scale already mentioned in Section 5.5.1. Only the in- and output quantities of the kinematic fit are approximately corrected for this offset.

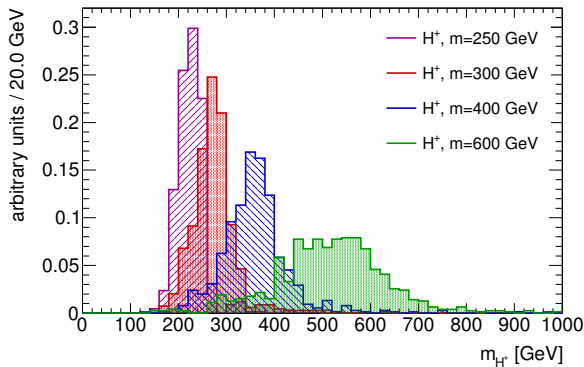


Figure 5.24: Normalized distributions of the correctly reconstructed charged Higgs boson mass for $m_{H^+} = 250, 300, 400$ and 600 GeV .

With minimum prerequisites, i.e. a reconstructed $t\bar{t}$ candidate plus an additional extra jet with $|\eta| < 5.0$, at least two charged Higgs boson candidates can be reconstructed per event.

It turns out that choosing the remaining jet with the highest transverse momentum leads to the best signal efficiency. If the selected top quark decays hadronically (leptonically) then the H^+ candidate is referred to as hadronic (leptonic) charged Higgs boson and the selected jet will be denoted as the second jet of the H^+ decay. Figure 5.25 shows the fitted and normalized hadronic and leptonic charged Higgs boson mass for the four different signal mass points and the combined background components. Here, “fitted” means that the four-vector of the top quark after kinematic fit is used for H^+ reconstruction.

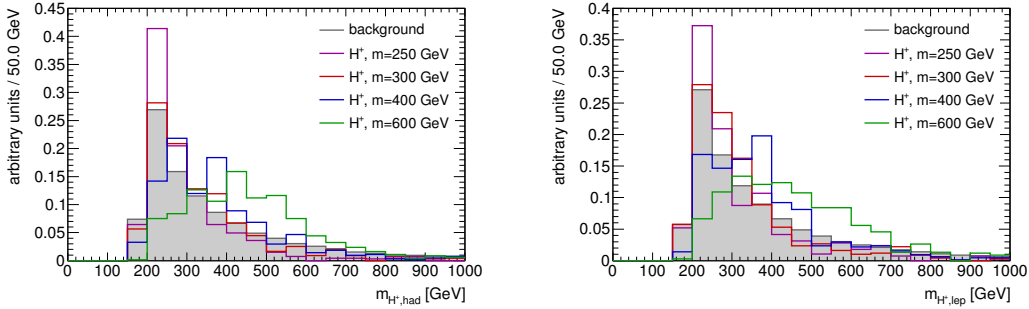


Figure 5.25: Normalized distributions of the fitted hadronic (left) and leptonic (right) charged Higgs boson mass for various signal samples. The gray shaded histograms show the sum of all considered background processes.

Without any assumptions about the mass of the charged Higgs boson it is difficult to decide if a hadronic or leptonic H^+ is present in the event or to find adequate properties to separate signal from background. Therefore, it is very difficult to apply a mass independent search. If a certain charged Higgs boson mass is assumed, several kinematic and topological event characteristics can be exploited to choose one H^+ combination and to separate signal from Standard Model background processes.

Among the two reconstructed charged Higgs bosons the one closer to the nominal H^+ mass is selected. This is a reasonable assumption but will also lead to an accumulation of background events in the search region. To separate signal and background, differences in the distributions of the following variables are exploited:

- (a) Minimum χ^2 of the kinematic fit: non- $t\bar{t}$ background is expected to have higher χ^2 values than events containing a true top anti-top pair. This cut corresponds to a tightening of the already applied $\text{prob}(\chi^2)$ cut.
- (b) Transverse momentum of the second jet of the H^+ decay: the heavier the charged Higgs boson the greater the momentum of the decay products should be. This variable is correlated to the jet pseudo-rapidity and is shown in Appendix D.
- (c) The H^+ centrality: the energy of the decay products of heavy objects like the charged Higgs boson should be deposited more centrally in the detector. The centrality, C , is

defined as:

$$C = \frac{\sum E_T}{\sqrt{(\sum E_T)^2 + (\sum p_z)^2}} . \quad (5.38)$$

Here, the sum runs over all objects assigned to the H^+ decay.

- (d) Opening angle in ΔR between the charged Higgs boson decay products - the top quark and the second jet of the H^+ decay. Lighter object tend to be more boosted and thus their decay products are more collimated in the laboratory frame. This variable is correlated to the to the H^+ transverse momentum and is shown in Appendix D.
- (e) Scalar sum of the transverse momenta of the two top quarks.
- (f) Opening angle in ΔR between the second jet of the H^+ decay and the extra jet. If more than one extra jet is present in the event the one with the highest b -tagging weight is taken. In background events where both of the b -jets may come from gluon-splitting the opening angle is expected to be lower than in signal events. This variable is correlated to the invariant mass of the two jets and is shown in Appendix D.
- (g) ΔR between the the system of the second jets of the top quarks and the second jet of H^+ .
- (h) b -tag weights
 - i) of the second jets of the top quarks
 - ii) of the second jet of the H^+
 - iii) of the extra jets with $p_T > 20$ GeV not associated to the top quarks and H^+ . For the signal process this extra jet is expected to be a b -jet. The η distribution of the extra jet is shown in Appendix D.

All properties of the top quarks are used after applying the kinematic fit. Otherwise, differentiation of events with and without neutrino solution must be made. Figure 5.26 and Figure 5.27 illustrate the distributions of the cut variables for the four H^+ masses and the sum of the various background components.

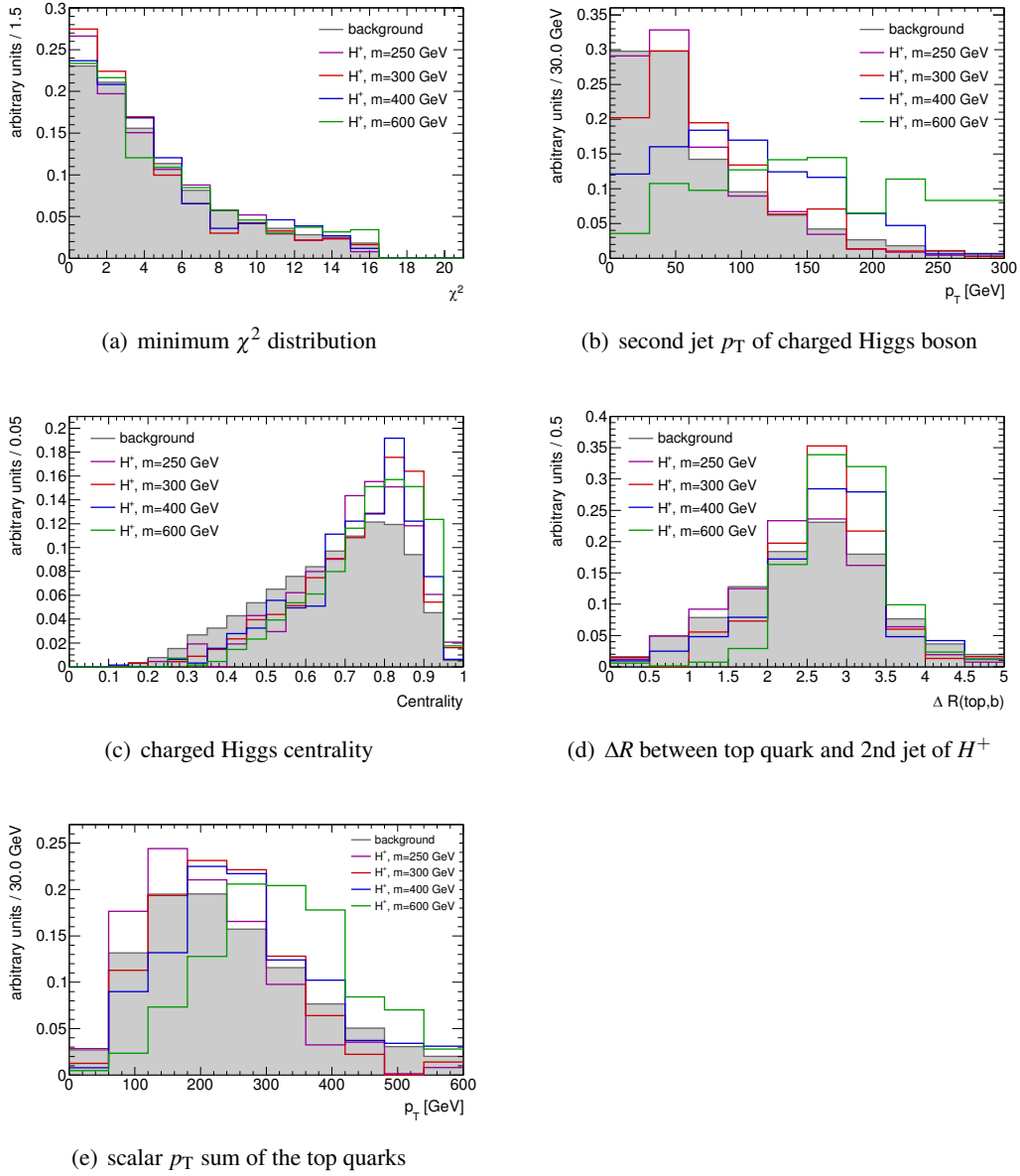


Figure 5.26: Normalized distributions of variables used for H^+ event selection. The colors denote different charged Higgs boson masses. The gray shaded histograms show the sum of all considered background processes.

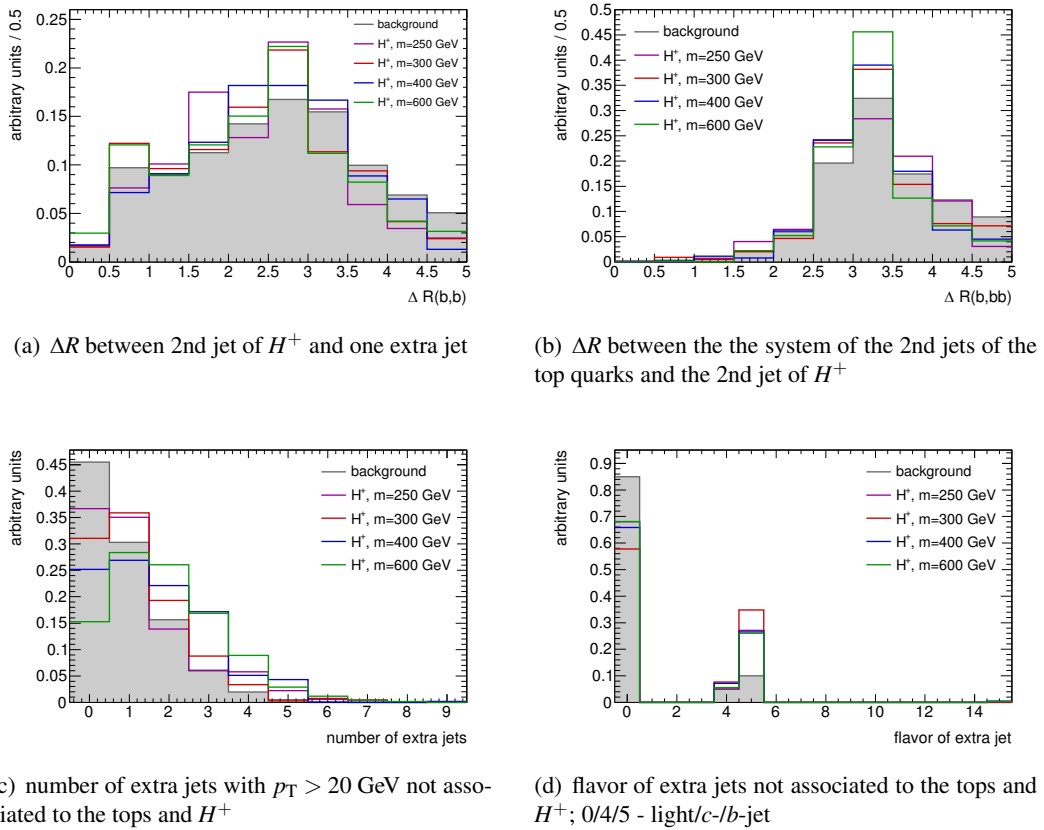


Figure 5.27: Normalized distributions of variables used for H^+ event selection. The colors denote different charged Higgs boson masses. The gray shaded histograms show the sum of all considered background processes.

m_{H^+} [GeV]	250	300	400	600	250	300	400	600
	Three b -tag analysis				Three b -tag + extra jet analysis			
Variable	Cut value							
(a), $\chi^2 <$	10	12.5	12.5	12.5	10	12.5	12.5	12.5
(b), $p_T >$	25	30	70	70	25	30	70	70
(c), $C >$	0.45	0.4	0.6	0.5	0.45	0.4	0.6	0.6
(d), $\Delta R(top, b) >$	0.4	1.75	2.1	1.8	0.4	1.75	2.1	1.9
(e), $p_T >$	80	90	90	250	80	90	90	240
(f), $\Delta R(b, b) >$	-	-	-	-	0.8	0.9	1.0	0.7
(g), $\Delta R(b, bb) >$	0.5	0.5	1.5	1.5	0.6	0.5	1.2	1.5
(h) i), ε_b	0.7	0.7	0.7	0.8	0.7	0.7	0.7	0.8
(h) ii), ε_b	0.6	0.5	0.7	0.6	0.6	0.5	0.7	0.6
(h) iii), ε_b	-	-	-	-	1.0	1.0	1.0	1.0

Table 5.4: Optimized cut values for the three b -tag and three b -tag + extra jet analysis.

The analysis is divided into two main selection classes: the three b -tag and the three b -tag plus extra jet analysis. The latter imposes additional requirements on the extra jet not associated to the top quarks and the H^+ whereas the former does not.

The cuts are optimized by the following procedure: All events within a mass window of 100 GeV around the nominal charged Higgs boson mass are selected and an estimator for the signal significance, Z , is calculated. Here, $Z = S/\sqrt{B}$ with S , the number of selected signal, and B , the number of selected background events. The definition of Z is an estimator of the discovery significance. A more refined approach for the evaluation of discovery and exclusion significances is given in Section 7. The width of the mass window has little influence on the discovery potential and hence is not optimized. All cuts are varied separately one after another and are adjusted to the values which maximize Z . The position of the maximum of Z with respect to the cut values is independent of the total amount of background or signal events and hence independent of $\tan\beta$ and the integrated luminosity. The procedure is iterated three times and is found to be sufficient since the final result of the last iteration is found to be stable. During this procedure some cut variables are dropped if their impact on Z is very small. They are shown in Appendix D.

The resulting cut values are presented in Table 5.4. It turns out that only relatively soft b -tagging cuts with high ε_b should be applied. In the three b -tag + extra jet analysis no b -tagging should be applied on the extra jet which corresponds to 100% b -tag efficiency. This analysis just requires an additional jet with $p_T > 20$ GeV and therefore is not called four b -tag analysis what could be misleading.

As already mentioned, the main background is the Standard Model $t\bar{t}$ production, in particular $t\bar{t}$ production in association of additional jets. This background component in association with light jets is not suppressed applying cut (h) i) whereas cut (h) ii) does not suppress $t\bar{t} + b$ -jets. And since additional b quarks only appear at least in pairs in the latter process, cut (h) iii) does not separate this background contribution from the charged Higgs boson signal. This general statements about b -tagging are not completely true since they may depend on the kinematic properties of the b -jets, e.g. in the latter process the b -jets may lie outside the detector acceptance.

Although optimized separately, the cut values of the three b -tag and the three b -tag + extra jet analysis are quite similar. This gives a certain degree of confidence that the obtained values are not influenced too much by statistical uncertainties and the number of iterations.

Table 5.5 shows the selection yields for $\tan\beta = 30$ and an integrated luminosity of 30 fb^{-1} for four different H^+ masses and the combined background after applying different levels of selection cuts. The signal selection efficiency from the selection cuts after H^+ reconstruction to the final cut values is approximately 10% and is nearly independent of the charged Higgs boson mass. Whereas the efficiency to select background events varies from 0.1% to 0.6%. Still the background, mainly $t\bar{t}$ production, is dominating. The resulting invariant charged Higgs boson masses are shown in Figure 5.28 and 5.29 for the three b -tag and the three b -tag + extra jet analysis, respectively. Here, the fitted masses are shown for an integrated luminosity of 30 fb^{-1} and $\tan\beta = 70$. The statistical significances are given in Table 5.6. The discovery potential is greater than or equal compared to previous studies at a center-of-mass energy of 14 TeV presented in [64]. Despite different analysis techniques this behavior is not expected since a larger center-of-mass energy results in approximately the same ratio of signal over background whereas the significance, Z , gets smaller. For intermediate H^+ masses of about 400 GeV the pure statistical 5σ discovery significance is already reached at $\tan\beta = 70$, compared to $\tan\beta = 140$ in the previous analysis. This difference in $\tan\beta$ corresponds to about a factor of four difference in signal cross-section (at $\sqrt{s} = 10 \text{ TeV}$). For low m_{H^+} (250 GeV) and very high m_{H^+} (600 GeV) masses the performances are comparable to each other.

Requiring an extra jet jets in the event helps to effectively suppress the Standard Model background but leads to no significant improvement in the discovery potential compared to analysis requiring only three b -tagged jets.

m_{H^+} [GeV]	250	300	400	600
No cut applied				
Signal	6780(60)	4680(30)	1970(10)	338(1)
Background	$65.5 \cdot 10^{12}$			
Basic cuts				
Signal	1590(30)	1140(20)	503(5)	81.0(4)
Background	$4.3 \cdot 10^6$			
After H^+ reconstruction				
signal	470(20)	336(9)	139(3)	24.4(2)
background	$437(4) \cdot 10^3$			
S/B [%]	0.108(5)	0.077(2)	0.032(1)	0.0056(1)
Three b -tag analysis				
Signal	50(5)	37(3)	15(1)	2.8(1)
Background	$2.7(2) \cdot 10^3$	$1.7(1) \cdot 10^3$	$0.8(1) \cdot 10^3$	$0.8(1) \cdot 10^3$
S/B [%]	1.9(2)	2.2(2)	1.9(3)	0.35(5)
Three b -tag + extra jet analysis				
Signal	43(5)	24(2)	12(1)	2.5(1)
Background	$1.9(2) \cdot 10^3$	$0.8(1) \cdot 10^3$	$0.6(1) \cdot 10^3$	$0.6(1) \cdot 10^3$
S/B [%]	2.3(4)	3.0(5)	2.0(4)	0.4(1)

Table 5.5: Selection yields for $\tan\beta = 30$ and an integrated luminosity of 30 fb^{-1} for four different H^+ masses and combined background components. Different cut levels are shown and the signal over background ratio (S/B) is compared. The numbers given in parentheses denote the statistical uncertainties on the last digits including the uncertainties arising from the available amount of Monte Carlo statistics.

m_{H^+} [GeV]	250	300	400	600
Three b -tag analysis				
S/\sqrt{B}	5.1	5.4	3.5	0.9
Three b -tag + extra jet analysis				
S/\sqrt{B}	5.3	4.8	3.5	0.9

Table 5.6: Pure statistical significance for the three b -tag and three b -tag + extra jet analysis for $\tan\beta = 70$ and an integrated luminosity of 30 fb^{-1} .

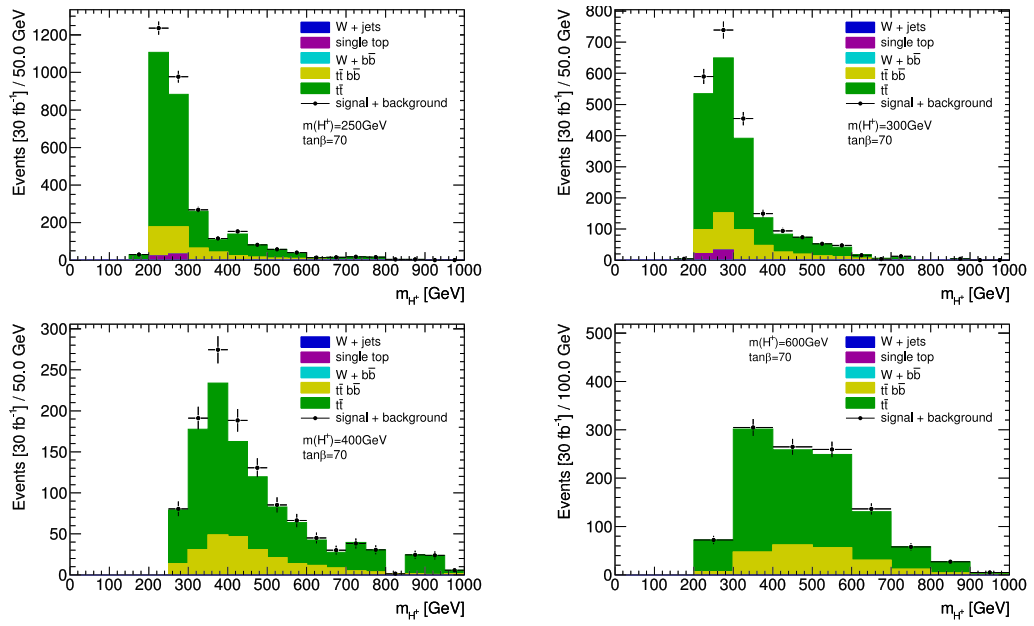


Figure 5.28: Distribution of the invariant charged Higgs boson masses for the three b -tag analysis. Here, the fitted masses are shown for an integrated luminosity of 30 fb^{-1} and $\tan\beta = 70$ for the m_h -max scenario. The given uncertainties reflect the statistical uncertainty of a data sample of 30 fb^{-1} . Systematic uncertainties are not included.

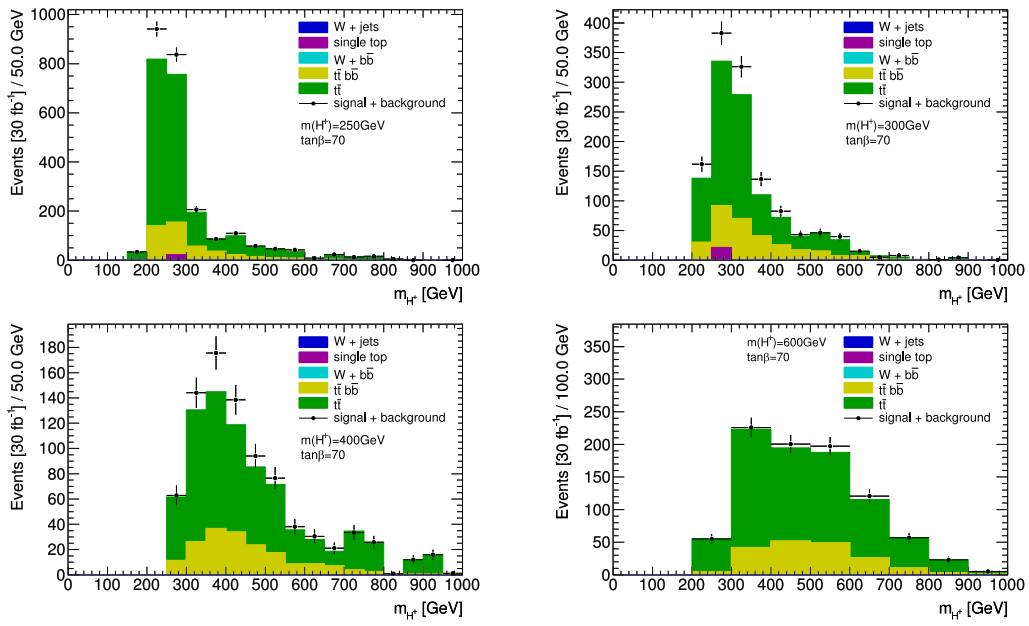


Figure 5.29: Distribution of the invariant charged Higgs boson masses for the three b -tag + extra jet analysis. Here, the fitted masses are shown for an integrated luminosity of 30 fb^{-1} and $\tan\beta = 70$ for the m_h -max scenario. The given uncertainties reflect the statistical uncertainty of a data sample of 30 fb^{-1} . Systematic uncertainties are not included.

6 Evaluation of systematic uncertainties

The observation criteria of a charged Higgs boson signal are subject to statistical and systematic uncertainties. The systematic uncertainties stem from theoretical and experimental sources.

In this analysis the experimental systematic uncertainties in the signal and background cross-section are taken from Monte Carlo predictions. This will give rise to additional systematic uncertainties due to limited available Monte Carlo statistics. The experimental uncertainties are discussed in Section 6.1 and the theoretical uncertainties in Section 6.2. Section 6.3 deals with the numerical impact of the experimental systematic uncertainties on the presented analysis.

6.1 Experimental systematic uncertainties

The experimental uncertainties consist of:

- uncertainties of the efficiencies of b -tagging and lepton (electron or muon) identification
- uncertainty in the energy scales for electrons, muons and jets
- uncertainty in the energy resolution for electrons, muons and jets
- uncertainty in the transverse missing energy scale and resolution
- uncertainty in the determination of the integrated luminosity and of background cross-sections

The expected dominant systematic uncertainties are the jet energy scale, the b -tagging efficiency and the light jet rejection rate. The systematic uncertainties considered together with their recommended values are shown in Table 6.1. The systematic uncertainty estimates are generally conservative and are based on specifications given in Reference [64]. Experimental uncertainties in the measurement of leptons and missing energy are not considered in this work.

The scale uncertainty is estimated by multiplying the jet energy with scaling factors shown in Table 6.1. For the uncertainties on the jet energy resolutions the energy is smeared by means of a Gaussian distribution. After jet energy manipulation the kinematic fit is repeated while the fit options are left unchanged.

For the uncertainty in b -tagging efficiency an offset value, β , is applied to the b -tagging weight of b -jets that are matched to generated jets coming from b quarks, such that the b -tagging efficiency is scaled down by 5%. A similar approach is applied for the uncertainty in the light jet rejection rate R . The cut on the b -tagging weight is shifted for light jets by

Source of uncertainty	Uncertainty and/or resolution
Jet energy resolution	$\sigma = 0.45 \cdot \sqrt{E}$ for $ \eta < 3.2$ $\sigma = 0.63 \cdot \sqrt{E}$ for $ \eta > 3.2$
Jet energy scale	$\pm 7\%$ for $ \eta < 3.2$ $\pm 15\%$ for $ \eta > 3.2$
b -tagging efficiency	-5%
Light jet rejection	$\pm 10\%$
Luminosity	$\pm 3\%$

Table 6.1: Recommended values for systematic uncertainties and resolution functions used to estimate the experimental systematic effects. The numbers are based on specifications given in Reference [64].

an offset value β , such that R is scaled by $\pm 10\%$. Since b -tagging is applied in intervals of jet transverse momentum, the values of β are determined as a function of jet p_T .

Additionally, a 3% uncertainty on the luminosity determination is taken into account.

6.2 Theoretical systematic uncertainties

Uncertainties in the expected production cross-sections for background and signal processes affect the discovery and exclusion potential. The uncertainty of the $t\bar{t}$ background is particularly interesting since this is the dominant background. A 6% uncertainty at NLO calculation is estimated by varying the renormalization and factorization scales by factors of two and from uncertainties in the PDFs [89]. Other backgrounds considered have similar or smaller uncertainties.

The uncertainty of the heavy H^+ production cross-section stem from PDF uncertainties and from uncertainties in the factorization and renormalization scale. The PDF uncertainties are evaluated to be between 7-20% and they do not depend on $\tan\beta$. The factorization and renormalization scale uncertainty is in the order of 20%. The relative systematic uncertainties on the charged Higgs boson branching ratio $BR(H^+ \rightarrow t\bar{b})$ is below 10% [53].

6.3 Effects of the systematic uncertainties

A detailed list of the effects for the various experimental systematic uncertainties is given in Table 6.2 and 6.3. The by far most dominant systematic uncertainty is the jet energy scale. For the background, the scale uncertainties are in the order of 20% and for the signal processes they can become even larger, up to 60%. Requiring up to three b -tags, this analysis is as expected strongly affected by uncertainties in b -tagging efficiency and rejection of light jets. They are in the order of about 10% for signal and background.

The total experimental systematic uncertainties are mostly asymmetric around zero. Even though, no attempt was made to symmetrize the uncertainties. Instead, a conservative

m_{H^+} [GeV]	250		300		400		600	
Component	S	B	S	B	S	B	S	B
Selected events	244	2249	218	1662	92	696	21	583
Systematic uncertainty								
Jet energy scale	-21 + 3	-23 +18	-39 + 0	-31 +12	-36 +21	-21 +16	-54 +10	-21 +21
Jet energy resolution	- 6	- 5	- 7	- 3	- 4	- 6	- 1	- 3
b -tag efficiency	-10	- 5	-20	- 7	- 8	- 9	-14	- 1
b -tag rejection	+ 4 - 0	+ 2 - 2	+ 0 - 2	+ 1 - 3	+ 7 - 0	+ 1 - 3	+ 3 - 6	+ 3 - 1
Luminosity	± 3	± 3	± 3	± 3	± 3	± 3	± 3	± 3
Total	-25 + 6	-25 +18	-44 + 3	-32 +12	-37 +23	-23 +17	-57 +11	-21 +21

Table 6.2: Number of selected events within a mass window of 100 GeV around the nominal H^+ mass and the effects of systematic uncertainties for the three b -tag analysis. The numbers are given in terms of percentage change in cross-section for the signal (S) and background (B). The uncertainties associated to each line are given in Table 6.1. For the total systematic uncertainty all positive and negative uncertainties are added in quadrature, respectively.

estimate is made, taking the maximal deviation for the resulting experimental systematic uncertainty.

The total experimental systematic uncertainty for the signal is between 30-60%, affecting mainly the exclusion sensitivity. For the background, the uncertainty estimates are in the order of 20% to 30%.

The fluctuations of the signal uncertainties between the four H^+ mass analysis are caused by statistical fluctuations due to the available signal Monte Carlo statistics. The large systematic uncertainty on the background prediction dilutes the discovery potential. Improved techniques, e.g. background estimation from data, direct measurement of PDF, higher level theory predictions including differential distributions, are thus needed. To evaluate the influence of a improved background level estimate, the discovery potential and exclusion limits are also calculated with only 10% background uncertainty.

Previous analysis at ATLAS neglected any theoretical systematic uncertainty [64] for discovery and exclusion limit calculation. To be consistent, they are neglected here as well.

In the ideal case of significance calculation the background cross-section is perfectly known. In order to measure the background cross-section and uncertainty from data, a signal-free sample should be obtained. For this analysis, however, the signal and back-

6 Evaluation of systematic uncertainties

m_{H^+} [GeV]	250		300		400		600	
Component	S	B	S	B	S	B	S	B
Selected events	212	1600	142	861	76	487	20	473
Systematic uncertainty								
Jet energy scale	-28	-24	-41	-33	-35	-23	-59	-21
	-10	+27	-7	+24	+10	+19	+1	+22
Jet energy resolution	-7	-6	-9	-6	-3	-5	-3	-3
b -tag efficiency	-10	-5	-17	-4	-11	-8	-11	-0
b -tag rejection	+0	+2	+0	+2	+6	+1	+4	+2
	-0	-2	-0	-2	-2	-2	-7	-1
Luminosity	± 3	± 3	± 3	± 3	± 3	± 3	± 3	± 3
Total	-32	-25	-46	-33	-37	-25	-60	-22
	+3	+27	+3	+25	+12	+20	+5	+22

Table 6.3: Number of selected events within a mass window of 100 GeV around the nominal H^+ mass and the effects of systematic uncertainties for the three b -tag + extra jet analysis. The numbers are given in terms of percentage change in cross-section for the signal (S) and background (B). The uncertainties associated to each line are given in Table 6.1. For the total systematic uncertainty all positive and negative uncertainties are added in quadrature, respectively.

ground are kinematically very similar which makes this approach very difficult. A possible way to estimate the background level from data is to impose the same selection cuts on the data as in the three b -tag analysis, but to require one b -tagged jet less. Even with two b -tagged jets, the main background remains $t\bar{t}$ production. After such a selection with only two b -tagged jets, the signal-to-background ratio is further reduced. It is then possible to calculate the expected number of background events plus its uncertainty, when tagging a third b -jet. The similar technique can then be used in an analysis with four b -tagged jets. For this method, the b -tagging efficiency and light jet rejection rate need to be measured from data.

Another possibility could be, to measure the background cross-section using side-bands in the reconstructed invariant H^+ mass distribution which are relatively signal free. The precision of this procedure depends on the charged Higgs boson mass and on the integrated luminosity available. No detailed study is conducted here.

7 Calculating significances

The primary method to quantify the statistical significance of a discovery or an exclusion is based on the p-value of the background-only or the signal+background hypothesis. The statistical formalism is based on the *Profile Likelihood* as used in [64] and described e.g. in [69, 90]. It is described, how statistical and systematic uncertainties are incorporated into the significances. For discovery, mainly the uncertainty of the background estimate is relevant but for exclusion limits in the $(\tan\beta, m_{H^+})$ space, the uncertainty on the signal estimate enters as well. In Section 7.5 the results are presented and discussed.

7.1 Introduction

The sensitivities for discovery and exclusion are calculated with the *Profile Likelihood* (PL) method [91]. This method uses a likelihood ratio to distinguish between two hypothesis, the background only hypothesis (H_0) and the signal+background hypothesis (H_1). When supposing a simple counting experiment, the expected number of background events, b , is determined with negligible uncertainty and that a signal model predicts an expected number of events s . Thus, the expectation value of the number of measured events n will follow a Poisson distribution and can be written as

$$E[n] = \mu s + b, \quad (7.1)$$

where μ is the signal strength parameter defined such that $\mu = 0$ corresponds to the hypothesis H_0 and $\mu = 1$ to the hypothesis H_1 . The signal normalization μ is the parameter of interest. All other parameters, like the background or any other adjustable parameters are considered as nuisance parameters. The PL removes the nuisance parameters in a frequentist-based way, without the explicit introduction of priors. The PL ratio is denoted by λ . In the simple case where the only nuisance parameter is the background, λ is given by:

$$\lambda(\mu) = \frac{L(\mu s + \hat{b})}{L(\hat{\mu} s + \hat{b})}. \quad (7.2)$$

Where \hat{b} is the Maximum Likelihood Estimator (MLE) of the background, $\hat{\mu}$ and \hat{b} are the MLE of the signal strength parameter and the number of background events. Here, $\hat{\mu}$ is required to be positive or zero, as this is the usual situation for a physical signal model.

From the definition of $\lambda(\mu)$, one can see that $0 \leq \lambda \leq 1$, with λ near 1 implying good agreement between the data and the hypothesized value of μ . Equivalently it is convenient to use the statistic

$$q_\mu = -2\ln\lambda(\mu) \quad (7.3)$$

as the basis of a statistical test. Higher values of q_μ correspond to an increasing incompatibility between the data and a given value of μ . A test of a hypothesized value of μ is

defined by using the statistic q_μ directly as measure of the discrepancy between the data and the hypothesis. To quantify the level of disagreement a p-value can be computed,

$$p = \int_{q_{obs}}^{\infty} f(q_\mu|\mu) dq_\mu , \quad (7.4)$$

where $f(q_\mu|\mu)$ is the sampling distribution of q_μ with the observed value q_{obs} under the assumption of μ .

Thus, to find the p-value the sampling distribution of $f(q_\mu|\mu)$ is needed. Under a set of regularity conditions and for a sufficiently large data sample, *Wilks' theorem* says that for a hypothesized value of μ , the probability density function of the statistic q_μ approaches a χ^2 distribution with one degree of freedom under the H_μ hypothesis, i.e. experiments with the signal being μs . More generally, if there are N parameters of interest, i.e. those parameters for which one gives hypothesized values in the numerator and MLE values in the denominator of the likelihood ratio in Eq. 7.2, then q_μ asymptotically follows a χ^2 distribution for N degrees of freedom. A proof and details of the regularity conditions can be found in Reference [92].

In addition of quoting only a p-value, the *significance* is often reported as well. The significance is defined as the number of standard deviations Z at which a Gaussian random variable of zero mean would give a one-sided tail area equal to the p-value. In particle physics, significances of $Z = 3$ and $Z = 5$ are referred to as so-called *evidence* and *discovery*. They correspond to p-values of $1.35 \cdot 10^{-3}$ and $2.87 \cdot 10^{-7}$, respectively. For purposes of excluding a signal hypothesis, a threshold p-value of 0.05 (i.e. 95% confidence level) is often used, which corresponds to $Z = 1.64$.

7.2 The likelihood function

In order to calculate discovery and exclusion significances with the help of the Profile Likelihood method the actual likelihood function needs to be defined.

In this study the number of selected events are treated like in a simple counting experiment. Thus, the expectation value of the measured events follows Eq. 7.1. The number of background events consists of N components,

$$b = \sum_{i=1}^N b_i . \quad (7.5)$$

In this analysis, the number of events from every background component is estimated from simulation. Each background sample consists of M_i events and the process corresponds to a cross section σ_i . This information is equivalent to the integrated luminosity $L_i = M_i/\sigma_i$ of the respective Monte Carlo sample.

A sub-sample m_i of these events are selected in the H^+ mass search region. From the statistical point of view, this is equivalent to have a auxiliary measurement of m_i following a Poisson distribution with expectation value

$$E[m_i] = \tau_i b_i . \quad (7.6)$$

If m_i is the number of Monte Carlo events found in the search region, then τ_i is the ratio of the integrated luminosities of the Monte Carlo sample to that of the anticipated (ap) luminosity,

$$\tau_i = \frac{L_{MC,i}}{L_{ap}}. \quad (7.7)$$

The anticipated luminosity corresponds to the amount of data for which the final discovery and exclusion limits are computed. The resulting likelihood function is the product of Poisson probabilities:

$$L(\mu, \mathbf{b}) = \frac{(\mu s + b)^n}{n!} e^{-(\mu s + b)} \prod_{i=1}^N \frac{(\tau_i b_i)^{m_i}}{m_i!} e^{-\tau_i b_i}. \quad (7.8)$$

The background components $\mathbf{b} = (b_1, \dots, b_N)$ are the nuisance parameters and μ is the parameter of interest. With the likelihood function given in Eq. 7.8 the statistical uncertainties arising from limited Monte Carlo statistics are properly taken into account.

If e.g. the number of background events in the search region are estimated from a number of events found in a control region, the same formalism can be used. In this case, τ_i is effectively the ratio of number of events in the signal to the control region and m_i represents the number of events found in the control region.

To quote a meaningful statistical significance of a discovery or exclusion, further systematic uncertainties on the signal and background predictions have to be taken into account. The recommended approach is to modify the model, i.e. the likelihood function, to include a nuisance parameter that corresponds to this uncertainty. This is broadened relative to the original likelihood, reflecting the loss of information due to the systematic uncertainty.

In Section 6.3 the total relative experimental systematic uncertainties for signal (δ_s) and background (δ_b) are given. It is assumed that both uncertainties are 100% correlated. To account for the uncertainties the expectation value given in Eq. 7.1 is modified to

$$E[n] = \mu(1 + \delta_s \alpha)s + (1 + \delta_b \alpha)b, \quad (7.9)$$

where α is a Gaussian distributed nuisance parameter with zero mean and width equal to one. The full likelihood function now becomes

$$L(\mu, \mathbf{b}, \alpha) = \frac{(\mu(1 + \delta_s \alpha)s + (1 + \delta_b \alpha)b)^n}{n!} e^{-(\mu(1 + \delta_s \alpha)s + (1 + \delta_b \alpha)b)} \prod_{i=1}^N \frac{(\tau_i b_i)^{m_i}}{m_i!} e^{-\tau_i b_i} \frac{1}{\sqrt{2\pi}} e^{-\alpha^2/2}. \quad (7.10)$$

Furthermore, the condition $(1 + \delta_s \alpha) \geq 0$ and $(1 + \delta_b \alpha) \geq 0$ must be fulfilled when calculating the MLE of α .

In practice, the software package *Minuit* [93] is used to fit the MLEs used in the Profile Likelihood.

7.3 Discovery potential for $H \rightarrow tb$

Establishing a discovery is equivalent to rejecting the $\mu = 0$ (background-only) hypothesis, i.e. that there is no Higgs signal present in the selected events. Since this analysis is entirely based on simulated data, a value for the measured entries n in the signal region has to be defined. In case of a discovery, a good approximation can be found simply by substituting the expectation values for signal and background $s + b$ for n (the so-called ‘‘Asimov’’ data).

In order to do this, the Profile Likelihood $\lambda(0)$ is calculated for each considered H^+ mass. The average expected sensitivity, $Z_{discovery}$, is then calculated using the χ^2 approximation

$$Z_{discovery} = \sqrt{-2\ln\lambda(\mu = 0)}. \quad (7.11)$$

The amount of expected signal is then scaled until $Z_{discovery} = 5$ is reached. The scaling factor directly translates into a value of $\tan\beta$. A change in $\tan\beta$ only affects the signal and does not alter the expected number of background events. And, as already mentioned, the position of the maximum of Z with respect to the cut values is independent of the total amount of signal or background events and hence independent of $\tan\beta$ as well.

7.4 Exclusion sensitivity for $H \rightarrow tb$

In addition to establishing discovery by rejecting the $\mu = 0$ hypothesis, an alternative hypothesis can be considered of some non-zero value of μ . Here, $\mu = 1$ is tested.

For purposes of setting an upper limit, the smallest μ has to be determined such that there is a fixed small probability (one minus the confidence level) to find data as compatible with that value of μ or less, relative to the degree of compatibility found with the real data. Therefore, the data with upward fluctuations in $\hat{\mu}$ are not counted when computing the p-value, because they would be compatible with some larger μ . Therefore, $0 \leq \hat{\mu} \leq 1$ is imposed when calculating $\lambda(1)$.

For setting limits, the Asimov data is the expected background alone. The exclusion sensitivity, $Z_{exclusion}$, is then calculated with

$$Z_{exclusion} = \sqrt{-2\ln\lambda(\mu = 1)}. \quad (7.12)$$

The amount of expected signal is then scaled until $Z_{exclusion} = 1.64$ is reached. This value corresponds to a p-value of 0.05 or 95% CL. The scaling factor directly translates into a value of $\tan\beta$.

7.5 Results

The results are summarized in the following for all four considered H^+ masses and for the three b -tag and three b -tag + extra jet analysis. They are illustrated in Figure 7.1 and Figure 7.2. They show the 5σ discovery and the 95% CL exclusion contours for the three b -tag and three b -tag + extra jet analysis, respectively. The sensitivities are calculated for two cases of statistical and three cases of systematic uncertainties to give an impression about their individual impact. The contours are drawn such that all computed points are

connected with a smooth curve [93].

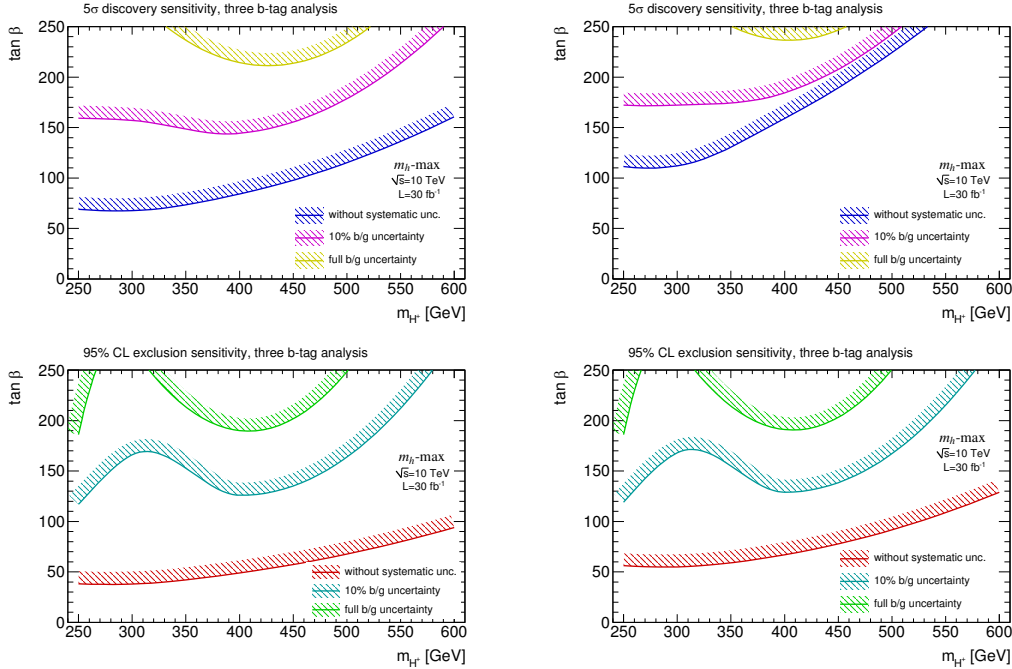


Figure 7.1: 5σ discovery (upper row) and 95% CL exclusion contour (lower row) for the three b -tag analysis for an integrated luminosity of 30 fb^{-1} . The left plots neglect and the right plots include statistical uncertainties arising from the finite amount of simulated events. Different numbers of systematic uncertainties on the background are applied and are explained in the text. The discovery and exclusion regions lie above the respective curves.

The statistical uncertainty arising from the finite amount of Monte Carlo events is either neglected or taken into account. To estimate the impact of these statistical uncertainties, the values of τ_i (cf. Eq. 7.7) are set to a very high values of 10^3 (large τ limit). This is equivalent to the case, that the expected signal and background events are estimated from Monte Carlo with a 10^3 times higher statistic than 30 fb^{-1} . The impact is clearly visible. The discovery and exclusion sensitivities are reduced by up to 40 and 10 in units of $\tan \beta$. A difference in $\tan \beta$ of about 20 correspond to a factor two in the signal cross-section (cf. Figure 2.11).

Three different cases for the systematic uncertainties are illustrated; a perfect signal and background estimate, the full signal uncertainty with either 10% or the full background uncertainty as evaluated in Section 6.3. The 10% background uncertainty is an estimate of how precise the background cross-section may be obtained. Prospects have already been addressed in Section 6. The systematic signal uncertainty is not scaled down since it is impossible to get a better estimate from data. The impact of including such uncer-

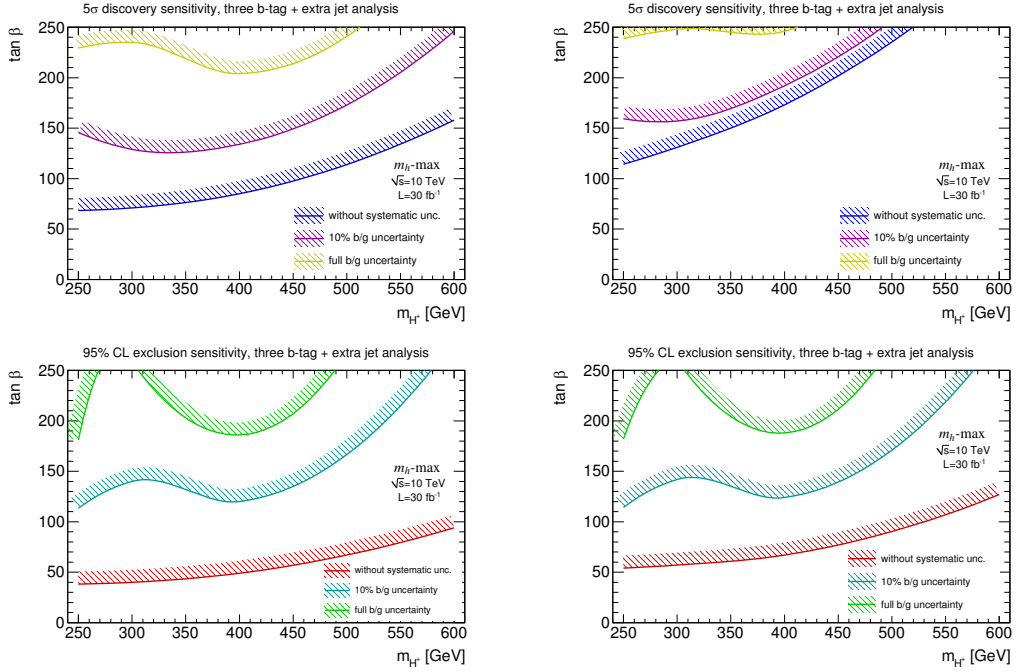


Figure 7.2: 5σ discovery (upper row) and 95% CL exclusion contour (lower row) for the three b -tag + extra jet analysis for an integrated luminosity of 30 fb^{-1} . The left plots neglect and the right plots include statistical uncertainties arising from the finite amount of simulated events. Different numbers of systematic uncertainties on the background are applied and are explained in the text. The discovery and exclusion regions lie above the respective curves.

tainties is tremendous. Even an optimistic assumption of the background uncertainty of 10% will remove most of the discovery or exclusion sensitivity. With perfect knowledge of the expected signal and background events the charged Higgs boson can be detected for $\tan\beta$ values down to 70 for $m_{H^+} = 250 \text{ GeV}$ based on an integrated luminosity of 30 fb^{-1} . Including all statistical and systematic uncertainties the reach in $\tan\beta$ reduces to approximately 250 for the same H^+ mass region. For exclusion, the region is reduced from 40 to about 180. The wavy shape of the sensitivity curves are caused by different systematic uncertainties between different charged Higgs boson masses (cf. Tables 6.2 and 6.3).

The three b -tag and the three b -tag + extra jet analysis have similar sensitivities if systematic uncertainties are neglected. When they are included, the three b -tag + extra jet analysis shows a better sensitivity especially for $m_{H^+} = 300 \text{ GeV}$ where the difference in $\tan\beta$ is about 30 for discovery and and exclusion. For the other mass point the sensitivities are comparable. The main reason is the better signal to background ratio obtained with the three b -tag + extra jet analysis.

8 Conclusion and outlook

In this work the ATLAS potential for discovering or excluding the existence of a charged Higgs boson heavier than the top quark has been evaluated. This has been done in the context of the m_h -max scenario of the Minimal Supersymmetric Standard Model (MSSM) for an integrated luminosity of 30 fb^{-1} and a center-of-mass energy of 10 TeV. The subsequent decay of the charged Higgs boson into heavy quarks $H^+ \rightarrow t\bar{b}$ has been studied, leading to a complex final state of four jets originating from b quarks, two jets from lighter quarks, one electron or muon and missing energy.

One of the main difficulties that arises when trying to reconstruct signal events is the high number of possible combinations of paired reconstructed objects in order to reconstruct the charged Higgs boson. It is shown that the reconstruction is possible by applying a kinematic fitting procedure, in which kinematic properties of the two appearing top quarks are exploited, and by a subsequent cut-based event and candidate selection. Such a kinematic fit has been developed and implemented in a dedicated *KinFitter* software package during this study together with J. E. Sundermann (University of Freiburg). It includes an iterative solution of the least square problem with non-linear constraints. The *KinFitter* package has been implemented into the ATLAS software framework. The high flexibility of the fitting algorithm assures its application to many physical problems and decay topologies and is therefore not limited to the reconstruction of top anti-top quarks.

In addition, the reconstruction of charged Higgs bosons makes high demands on the ability to identify jets containing b -hadrons. A good b -tagging performance is needed in order to efficiently reconstruct charged Higgs bosons and to suppress Standard Model background. A dedicated b -tagging algorithm, *TrackCounting*, has been developed and implemented into the ATLAS software framework during this study. Good b -tagging performance can be obtained using this algorithm. It is simple and robust and it does not require any special initialization such as reference histograms or the reconstruction of secondary vertices inside jets. The *TrackCounting* algorithm is part of the recommended algorithms for the early data taking period in ATLAS. The behavior of these algorithms has been studied with the first 7 TeV collision data recorded in 2010 and were found to compare well with expectations from Monte Carlo simulation. Although a more refined b -tagging algorithm is used in this work, such simple tagging algorithms are very useful at the early stage of data taking because they offer a very quick optimization step and adaptation to the physical process due to the limited number of parameters.

In order to reconstruct charged Higgs bosons two strategies are considered that are based on the requirement of an additional jet not associated to the charged Higgs boson and the top quarks. In both cases the dominant remaining background is $t\bar{t}$ production with additional real or misidentified jets originating from b quarks. This irreducible background component remains large and is kinematically very similar to the signal.

The discovery and exclusion sensitivity in the $H^+ \rightarrow t\bar{b}$ channel is investigated in the $(m_{H^+}, \tan\beta)$ parameter space of the MSSM. The most important experimental systematic uncertainties on the signal and background cross-section and uncertainties arising from

the limited amount of Monte Carlo statistics and their impact on the search are evaluated. The uncertainties are found to be large and they highly dilute the discovery and exclusion sensitivity. With perfect knowledge of the expected signal and background events the charged Higgs boson can be detected for $\tan\beta$ values down to 70 for $m_{H^+} = 250$ GeV. Including all considered uncertainties the reach in $\tan\beta$ reduces to approximately 250 for the same charged Higgs boson mass region. The sensitivities for the two different analysis strategies are found to be comparable.

This channel has previously been studied in ATLAS at a center-of-mass energy of 14 TeV [64]. No discovery or exclusion power could be extracted from this channel on its own. It, however, contributed to the combined H^+ sensitivity. The discovery potential obtained in this work is greater than or equal compared to the previous study. Despite different analysis techniques this behavior was not expected since a larger center-of-mass energy results in approximately the same ratio of signal over background whereas the significance gets smaller. This indicates that an application of the presented analysis technique on 14 TeV data would result in a significantly improved sensitivity compared to the previous analysis.

To extend the discovery reach several improvements are necessary. Multivariate techniques need to be employed to further improve the separation of signal and background. The applied kinematic fit already shows a good selection efficiency of correctly reconstructed $t\bar{t}$ candidates. They appear in signal (and background) events and are needed in order to reconstruct the charged Higgs boson. The output of the kinematic fit can also be incorporated in a multivariate analysis. However, a higher Monte Carlo statistics for signal and background is favorable to obtain reliable results.

It would also be favorable to measure the background cross-section directly from data. Some possible approaches have been addressed. In this work the event rates for signal and background processes are taken from Monte Carlo predictions. Two different event generators have been used for the main remaining background component, $t\bar{t}$ production with additional jets. Double counting of events can occur between the two samples. To avoid this in a rigorous way, a NLO event generator should be used to simultaneously simulate both processes. Such a generator was not available at the time of writing and the problem was solved approximately by identifying and rejecting possible overlapping events in one sample.

Finally, it should be noted that the results presented here are obtained only including the main expected systematic experimental effects. Trigger information together with their expected efficiencies are not included. In addition, the discovery potential is evaluated not taking into account theoretical systematic uncertainties.

The first collisions at the LHC took place in November 2009. Since then, several pb^{-1} of data has been recorded by the experiments. Before the big expectations, like Higgs boson discovery or discovery of physics beyond the Standard Model, can be met, the detectors like ATLAS have to be calibrated and understood first. For the detection of the charged Higgs bosons in the $H^+ \rightarrow t\bar{b}$ decay channel the identification of jets containing b -hadrons is of particular importance. The behavior of the b -tagging algorithms suited for first data has already been analyzed and are found to compare well with expectations from Monte

Carlo simulation. At the same time Standard Model processes like Z or $t\bar{t}$ production are analyzed and will provide ideal standard candles for calibration of the detector and for verification of the reconstruction performance.

A Signal sample production

Since no official signal Monte Carlo for $\sqrt{s} = 10$ TeV is available, a dedicated production starting from event generation up to reconstruction was done. The involved steps within this production process are illustrated in Figure A.1. The full production chain can be short circuit by using *Atlfast* which provides a fast simulation of the whole chain by taking the generated events and smearing them to produce AOD directly. The production of *Atlfast* Monte Carlo takes only a fraction of time compared to the full process. But since a fast detector simulation sample needs additional validation only the full chain production has been carried out.

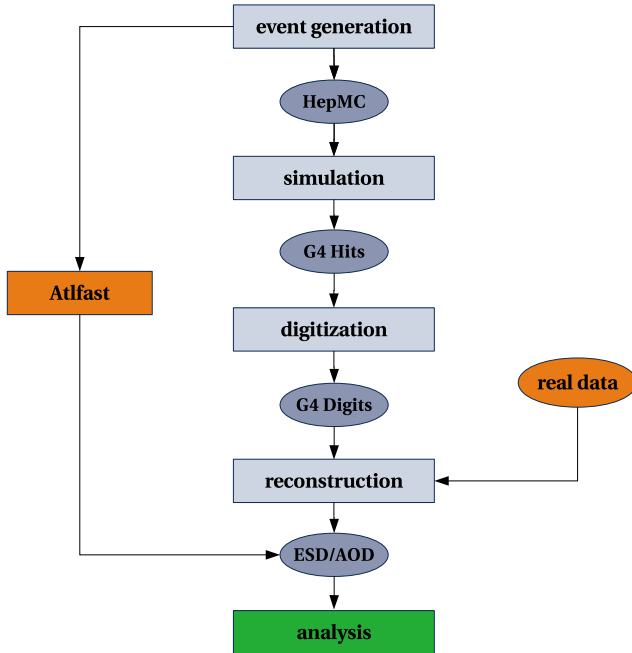


Figure A.1: Schematic representation of the ATLAS full chain Monte Carlo production.

The events ($g\bar{b}/gg \rightarrow [b]H^+\bar{\tau}$) were generated with the *Matchig* [54] event generator which matches the two twin processes for heavy charged Higgs production (cf. Section 2.3.3) by producing negative weight events from an identified double-counting term. Here, *Matchig* was used as an external process to *Pythia* for H^+ production. Although τ leptons are not used in this analysis, the correct treatment of the τ polarization is ensured. The *Pythia* τ decay was switched off and the τ handed over to *Tauola* [94] for decay. Final state QED radiation of leptons and hadrons was handled by *Photos* [95].

In total 20k events were generated for each considered H^+ mass point ($m_{H^+} = 250, 300, 400$ and 600 GeV). About 1/4 of the generated events have a negative weight. Only the sum of the weights is a physical quantity and therefore, if the integrated luminosity for each

sample is calculated, the numerator must be the sum of the weights. Simplified speaking, only about $10k$ physical events for each sample are available for analysis. This fact has been already considered in the luminosity calculation presented in Table 5.1.

Event generation, full detector simulation and reconstruction has been performed with release 15.3.1.6 of the ATLAS software. For the event generation and detector simulation the same options like, e.g. detector geometry or the version of the offline condition, are used as for the so-called *mc08* production effort. The only difference to those samples is that a newer release was used since the appropriate version of Matchig was not available for older ATLAS software. From the reconstruction of *G4Hits* onwards all options are equal to the so-called *mc08 re-reco* effort (reconstruction tag *r838*). For this campaign *mc08 G4Hits* (simulation tag *s520*) were re-reconstructed with release 15.3.1.6. All background samples are used from this campaign and for consistency reasons it was tried to produce the signal as close as possible to them.

It must be mentioned that these privately produced samples are not official, which means that they are not approved by ATLAS.

B Resolutions

In this Section the resolutions of p_T , η and ϕ of electrons, muons and light jets in intervals of the measured transverse momentum and pseudo-rapidity are illustrated. They are used to derive quantities that are used as input for the kinematic fit. The width of the intervals is chosen to contain about the same amount of the particular objects. The resolutions are obtained by comparing the respective values between the reconstructed and generated object.

Figures B.1, B.4 and B.7 show the integrated resolution, i.e. not in intervals of p_T and η , of their absolute and relative values. The blue lines indicate a fit with a Gaussian function from where the mean μ and the standard deviation σ of the resolution is obtained.

In Figures B.2, B.5 and B.8 the distribution of μ together with its uncertainty are shown in intervals of p_T and η . They are used to correct the respective measured quantities before entering the kinematic fit.

Figures B.3, B.6 and B.9 show the distribution of the obtained σ together with its uncertainty in intervals of p_T and η . They are used to construct the covariance matrix \mathcal{V} (cf. Eq. 5.6) as input for the kinematic fit.

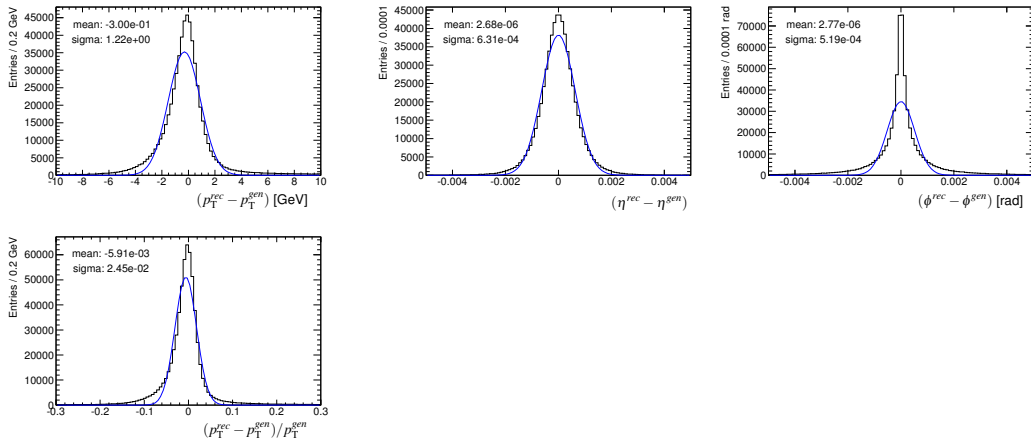


Figure B.1: Distribution of the integrated resolution of p_T (left), η (middle) and ϕ (right) of the **electron**. The upper row shows the resolution of their absolute values and the lower row of their relative p_T , respectively. The blue lines shows the results of Gaussian fits which are applied over the whole range of the histograms and the obtained means and standard deviations are given.

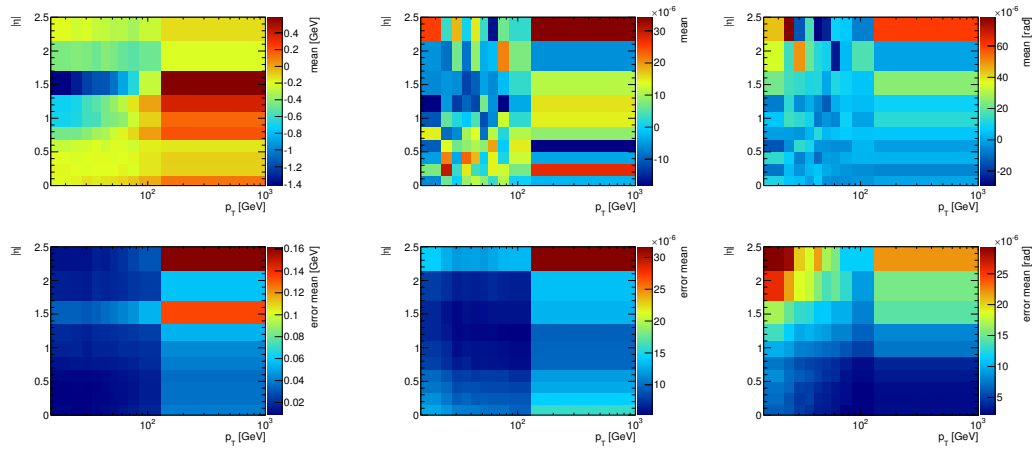


Figure B.2: Distribution of the mean (upper row) and its statistical uncertainty (lower row) of the resolution of p_T (left), η (middle) and ϕ (right) of the **electron**. The parametrization is given by the absolute values of the momentum vector components. The values are obtained by a Gaussian fit in 10 intervals of the measured p_T and η , respectively.

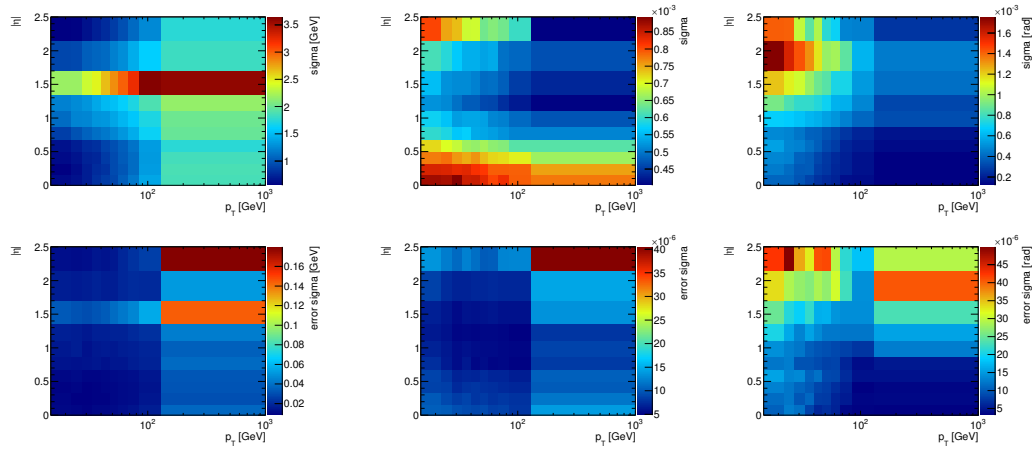


Figure B.3: Distribution of the standard deviation (upper row) and its statistical uncertainty (lower row) of the resolution of the absolute values of p_T (left), η (middle) and ϕ (right) of the **electron**. The parametrization is given by the absolute values of the momentum vector components. The values are obtained by a Gaussian fit in 10 intervals of the measured p_T and η , respectively.

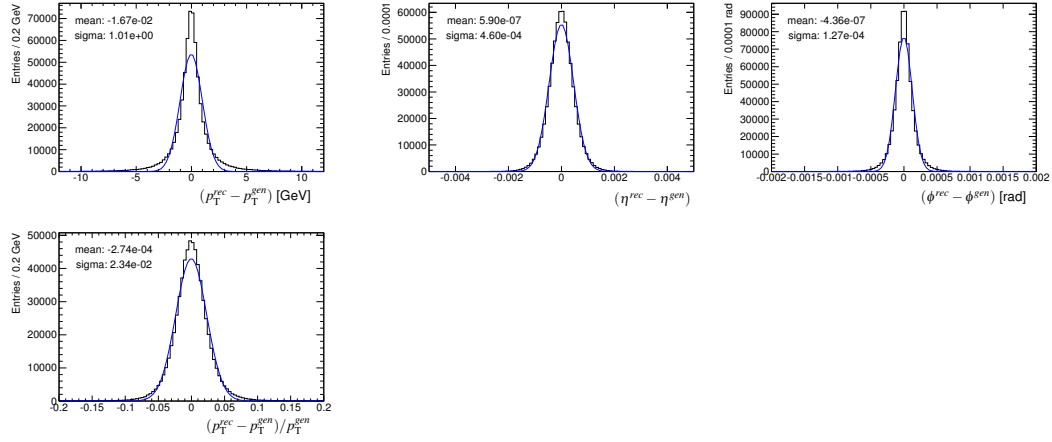


Figure B.4: Distribution of the integrated resolution of the absolute values of p_T (left), η (middle) and ϕ (right) of the **muon**. The upper row shows the resolution of their absolute values and the lower row of their relative p_T , respectively. The blue lines shows the results of Gaussian fits which are applied over the whole range of the histograms and the obtained means and standard deviations are given.

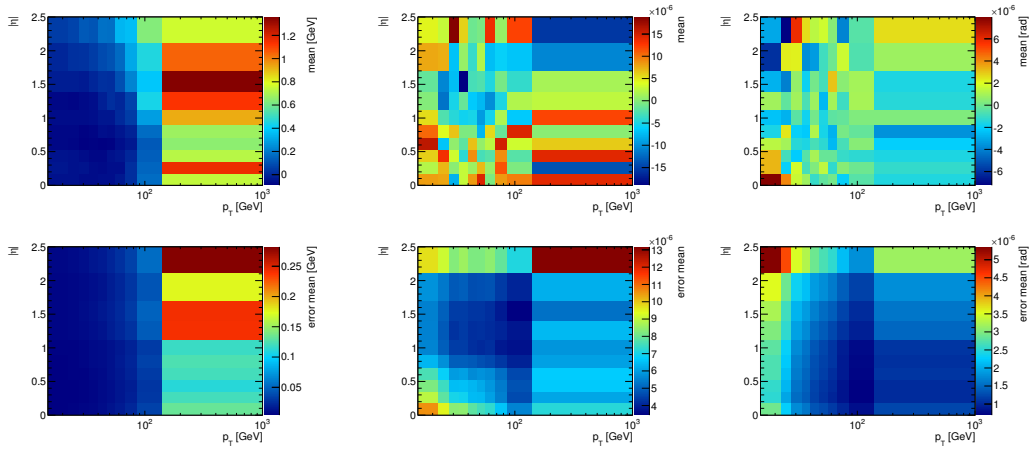


Figure B.5: Distribution of the mean (upper row) and its statistical uncertainty (lower row) of the resolution of p_T (left), η (middle) and ϕ (right) of the **muon**. The parametrization is given by the absolute values of the momentum vector components. The values are obtained by a Gaussian fit in 10 intervals of the measured p_T and η , respectively.

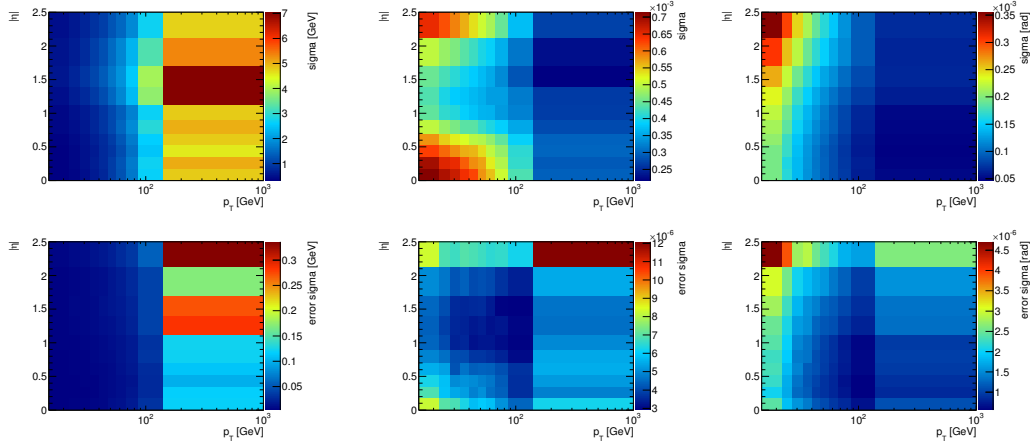


Figure B.6: Distribution of the standard deviation (upper row) and its statistical uncertainty (lower row) of the resolution of p_T (left), η (middle) and ϕ (right) of the **muon**. The parametrization is given by the absolute values of the momentum vector components. The values are obtained by a Gaussian fit in 10 intervals of the measured p_T and η , respectively.

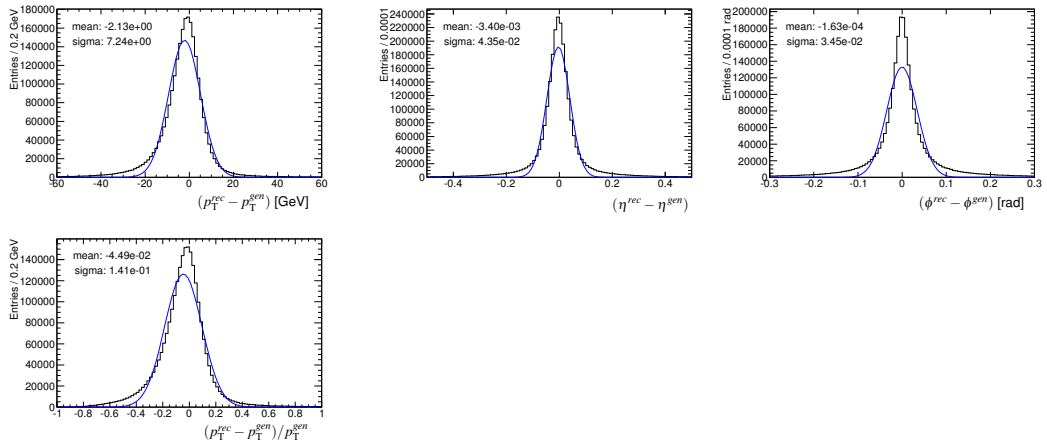


Figure B.7: Distribution of the integrated resolution of p_T (left), η (middle) and ϕ (right) of **light jets**. The upper row shows the resolution of their absolute values and the lower row of their relative p_T , respectively. The blue lines shows the results of Gaussian fits which are applied over the whole range of the histograms and the obtained means and standard deviations are given.

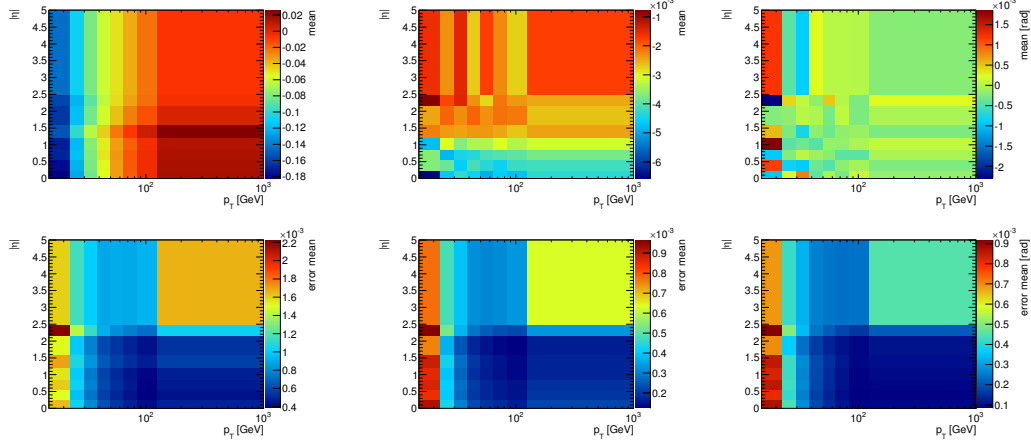


Figure B.8: Distribution of the mean (upper row) and its statistical uncertainty (lower row) of the resolution of relative p_T (left), absolute η (middle) and ϕ (right) of **light jets**. The values are obtained by a Gaussian fit in 8 intervals of the measured p_T and η , respectively.

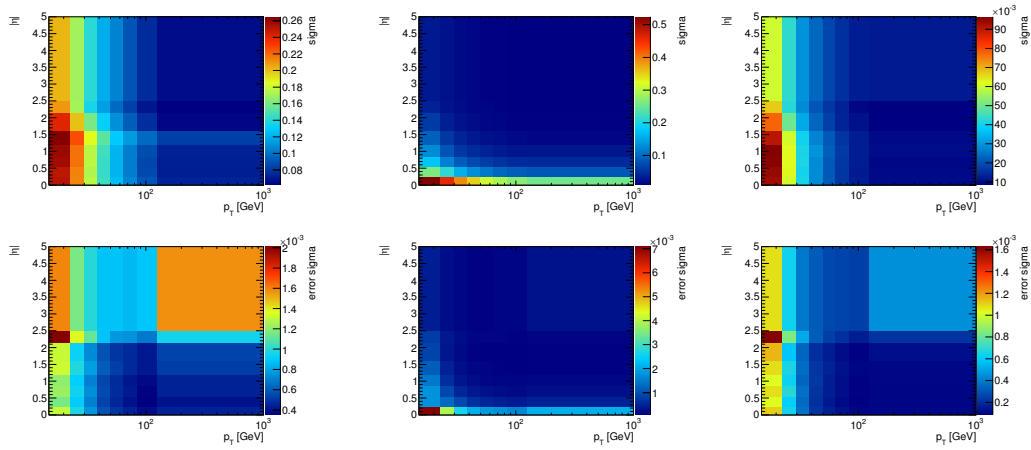


Figure B.9: Distribution of the standard deviation (upper row) and its statistical uncertainty (lower row) of the resolution of relative p_T (left), absolute η (middle) and ϕ (right) of **light jets**. The parametrization is given by the relative values of the four-vector components. The values are obtained by a Gaussian fit in 8 intervals of the measured p_T and η , respectively.

C Variations in the kinematic fit

In this Section it is discussed how different fit options and an alternative approach influence the performance of the $t\bar{t}$ candidate selection. It is preferable that the efficiency to select correctly reconstructed top anti-top pairs in conjunction with purity is high. In the standard analysis the selection is performed with the help of a kinematic fit. For convenience, the used fit options are again summarized in the following:

- resolutions in intervals of objects transverse momentum and pseudo-rapidity
- offset correction of fitted quantities before entering the kinematic fit
- four mass constraints on fixed values; two W bosons with 80.4 GeV and two top quarks with 172.5 GeV

All following studies are performed on the $t\bar{t}$ sample with the same event selection as in the standard analysis presented in Section 5.3.3.

Alternative χ^2 definition

The kinematic fit varies the measured quantities within its errors until given constraints are fulfilled. This is done in a way that a likelihood function (cf. 5.7) is minimized. The $t\bar{t}$ candidate with the smallest χ^2 is then selected for further analysis.

Another possibility is to choose a candidate with the smallest χ_{alt}^2 , defined by

$$\chi_{alt}^2 = \frac{(m_{jj} - m_W)^2}{\sigma_W^2} + \frac{(m_{jjj} - m_{top})^2}{\sigma_{top}^2} + \frac{(m_{lvj} - m_{top})^2}{\sigma_{top}^2}. \quad (C.1)$$

Where m_{jj} and m_{jjj} (m_{lvj}) are the reconstructed invariant masses of the hadronically (leptonically) decaying W boson and top quark, respectively. $m_W = 77$ GeV ($m_{top} = 160$ GeV) and $\sigma_W = 10$ GeV ($\sigma_{top} = 17.5$ GeV) are the mean and the standard deviation of the correctly reconstructed W boson (top quark) mass distribution (cf. 5.11) obtained by a Gaussian fit. Eq. C.1 can only be defined for events where at least one neutrino solution can be calculated. Additionally, no term for the leptonically W boson appears since its mass is fixed to $m_W = 80.4$ GeV.

This alternative approach is not a kinematic fit since it does not change any property of the measured particles. It selects the $t\bar{t}$ candidate whose measured composite particle masses (the W boson and the top quark) have the smallest difference, weighted with the width, to the means of the correctly reconstructed masses.

The performance in terms of efficiency and purity is illustrated in Figure C.1. For comparison the performance plot of the kinematic fit is also shown. For events where a neutrino

solution can be calculated the behavior of both approaches is quite similar. The maximal efficiency, obtained without cutting on χ^2_{min} , is almost identical. With tighter cuts on the minimum χ^2 the kinematic fit achieves a slightly better purity, e.g. for an efficiency of 50% the gain in purity is about 2.5%.

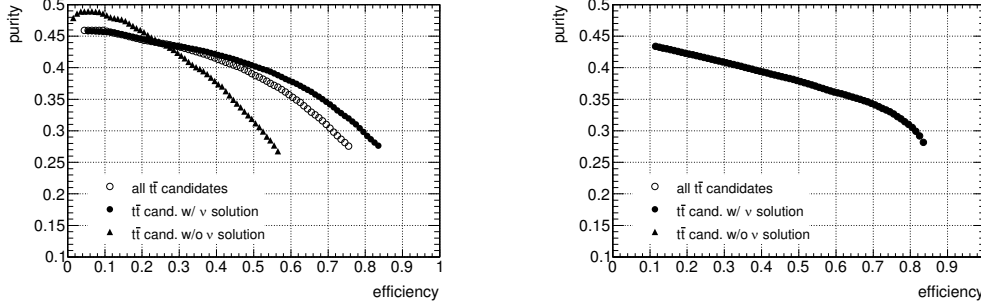


Figure C.1: Purity versus efficiency of the kinematic fit (left) and the alternative χ^2 definition (right) for different cuts on χ^2_{min} for the $t\bar{t}$ sample. The filled circles represents events where a neutrino solution could be found and the filled triangles where not. For the events denoted by open circles no such distinction is made.

Besides the slightly better performance of the kinematic fit, events with no neutrino solution can be retained. This affects about 20% of all $t\bar{t}$ events. For reasons of simplicity the alternative approach is attractive though.

Different constraints

For the standard analysis fixed mass constraints on the W bosons and top quarks are applied. It is also possible to make soft constraints with finite width either Gaussian or Breit-Wigner shaped. Both possibilities are tested with a width of $\sigma_W/\Gamma_W = 2$ GeV and $\sigma_{top}/\Gamma_{top} = 3$ GeV and are found to have negligible impact on the performance since the intrinsic width of both particles is at least one order of magnitude smaller than the detector resolution.

Another possibility is to require both top quarks to have equal mass after kinematic fit. No restriction is made about the actual value of the top quark mass. The performance plot and the leptonic and hadronic top quark mass distributions are shown in Figure C.2 and C.3, respectively. The efficiency and purity compared to the standard options is worse for all cuts on χ^2_{min} (cf. left plot in Figure C.1). Nevertheless it shows nicely the abilities of the kinematic fit. The fitted leptonic and hadronic mass distributions are, as required, identical to each other. The width of the distribution of correctly reconstructed top quarks is reduced from 15 GeV and 19.4 GeV to 12.4 GeV for the hadronic and leptonic top quark, respectively.

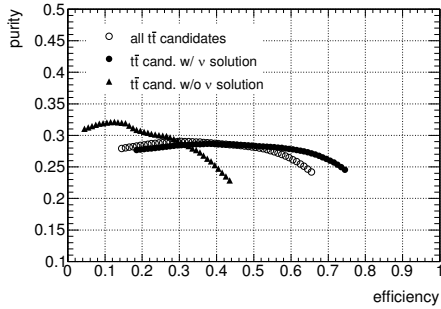


Figure C.2: Purity versus efficiency for different cuts on χ_{min}^2 for the $t\bar{t}$ sample. The two top quarks are constraint to have equal masses after the kinematic fit. The filled circles represents events where a neutrino solution could be found and the filled triangles where not. For the events denoted by open circles no such distinction is made.

Unbinned resolutions

For the standard analysis the resolution of every object is obtained in intervals (so-called *bins*) of the measured transverse momentum and pseudo-rapidity. The width of each parameter resolution is used to fill the covariance matrix \mathcal{V} as defined in Eq. 5.6. The following study analysis the performance where the resolutions are obtained unbinned or integrated over p_T and η .

Figure C.4 shows purity versus efficiency for different cuts on χ_{min}^2 for the $t\bar{t}$ sample. The overall performance is very similar to the standard analysis except for events where no neutrino solution can be calculated. The analysis using the binned resolution retains more true $t\bar{t}$ events and the efficiency is higher.

Despite performing better for events with no neutrino solution the difference was expected to be more pronounced since within the standard analysis the covariance matrix should describe true $t\bar{t}$ events much better. It is difficult to draw a conclusion what causes the similarity of both methods. One possibility is that the large tails in the resolution that are not well described by the approximation of a Gaussian function may be better described by an intermediate (unbinned) resolution function. And of course, the background is affected as well.

No offset correction

In the standard analysis the measured quantities are corrected for a systematic offset in the measurement (cf. Section 5.5.1). The following study evaluates the impact on the performance if the offset is not corrected. In Figure C.5 shows the purity versus efficiency for different cuts on χ_{min}^2 . The difference is clearly visible. The performance degrades by about 5% in efficiency and purity compared to the standard analysis. Hence it is preferable to have an accurate measurement not only in terms of resolution but also in scale.

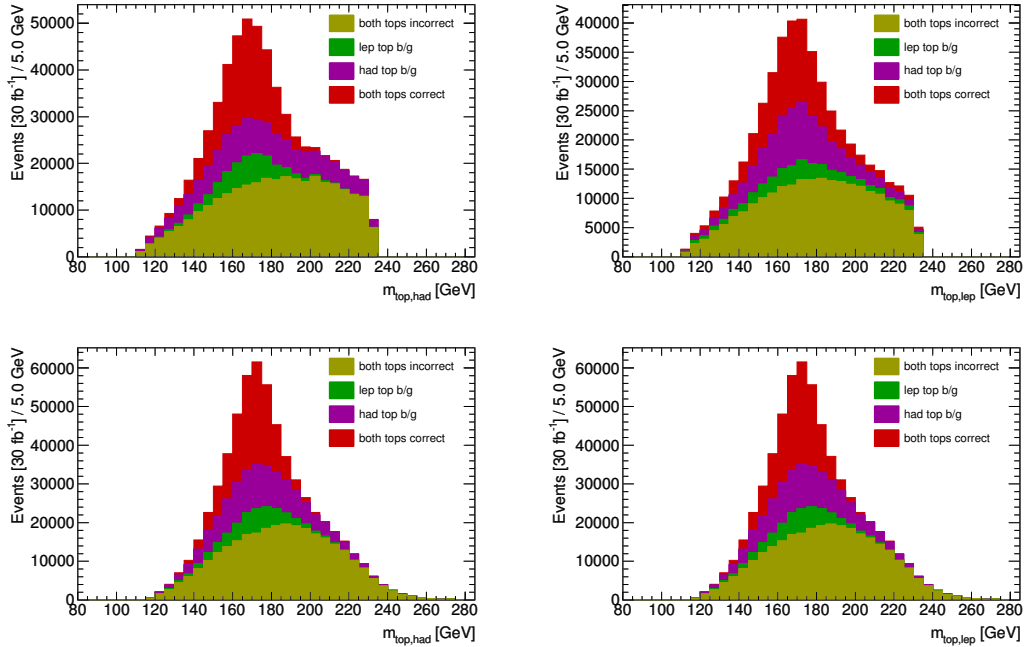


Figure C.3: Reconstructed (top row) and fitted (bottom row) invariant masses of the hadronically (left) and leptonically (right) decaying top quark after kinematic fit of the $t\bar{t}$ sample. The two top quarks are constrained to have equal masses after the kinematic fit. The colors represent different levels of matching to generator level objects. Red: both top quarks are correctly reconstructed; Purple: only leptonic top is correctly reconstructed; Green: only hadronic top is correctly reconstructed; Yellow: both top are not correctly reconstructed.

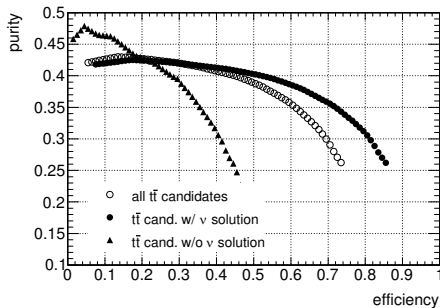


Figure C.4: Purity versus efficiency for different cuts on χ_{min}^2 for the $t\bar{t}$ sample with unbinned resolutions. The filled circles represents events where a neutrino solution could be found and the filled triangles where not. For the events denoted by open circles no such distinction is made.

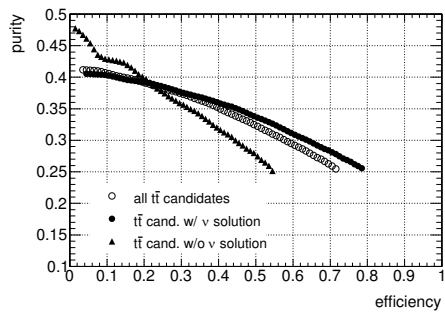


Figure C.5: Purity versus efficiency for different cuts on χ_{min}^2 for the $t\bar{t}$ sample. No offset correction is applied. The filled circles represents events where a neutrino solution could be found and the filled triangles where not. For the events denoted by open circles no such distinction is made.

D Additional discriminating variables

Variables showing some discriminating power to separate signal from background are dropped during the cut optimization process. They are shown in Figure D.1 and D.2 and described in the following.

- (a) The p_T ratio of the top quarks, the top with the smaller p_T is in the numerator: in $t\bar{t}$ events both top quarks tend to have the same scalar transverse momentum.
- (b) Vectorial sum of the transverse momenta of the two top quarks; in $t\bar{t}$ events both top quarks tend to be more back-to-back and to have more equal scalar transverse momentum.
- (c) The transverse momentum of H^+ ; The heavier the charged Higgs boson the higher its transverse momentum.
- (d) The charged Higgs p_T ratio is the ratio of the transverse momenta of the 2nd jet of the H^+ and the top quark associated to the charged Higgs boson. The smallest p_T is in the numerator.
- (e) The pseudo-rapidity of the second jet of the H^+ decay: the heavier the charged Higgs boson the more central the decay products should be.
- (f) The pseudo-rapidity of the jet not associated to the tops and the H^+ . If more than one extra jet is present in the event the one with the highest b -tagging weight is taken.
- (g) Invariant mass of the system of the second jet of the H^+ decay and the extra jet. If more than one extra jet is present in the event the one with the highest b -tagging weight is taken. In background events where both of the b -jets may come from gluon-splitting their invariant mass is expected to be lower than in signal events.

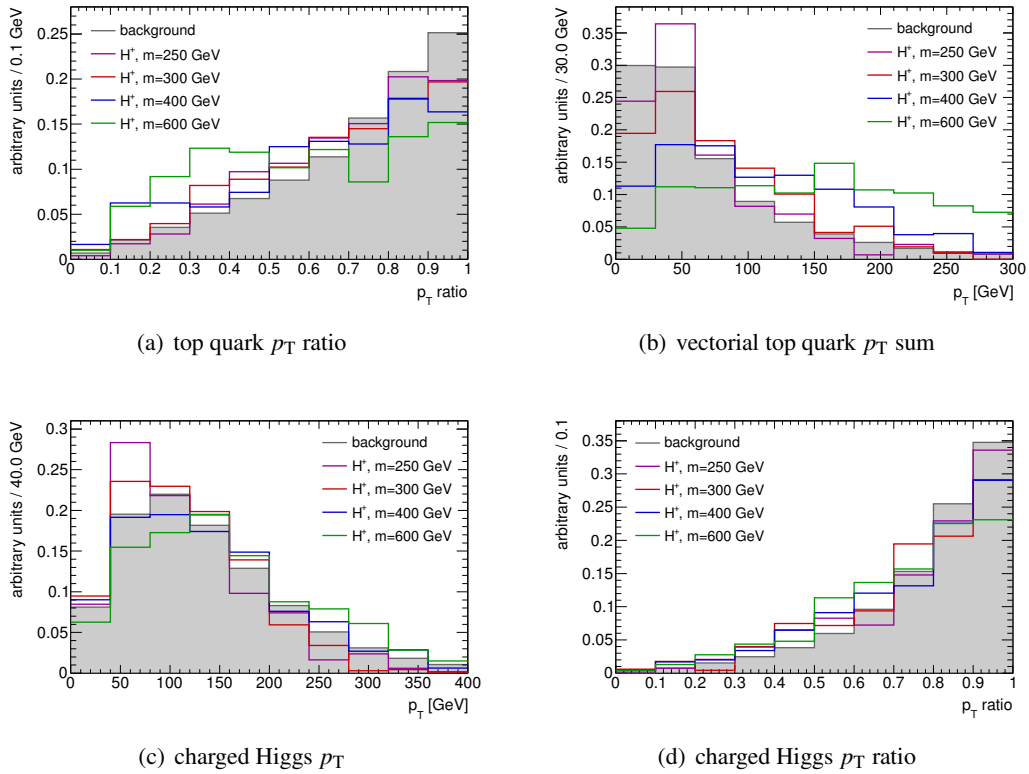
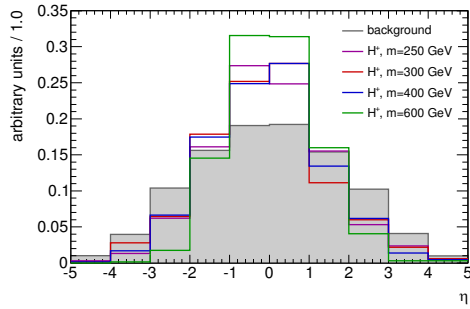
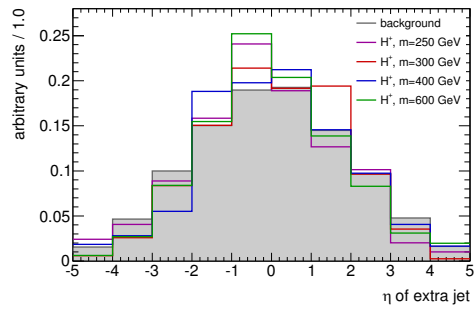


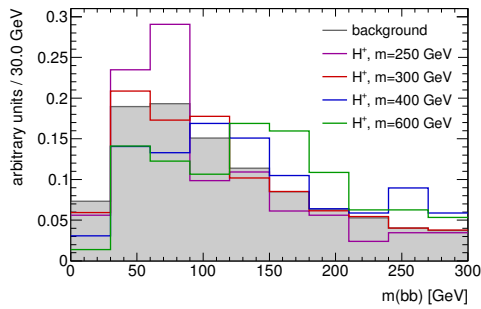
Figure D.1: Normalized distributions of variables not used for H^+ event selection but showing some discriminating power to separate signal and background. The colors denote different charged Higgs boson masses. The gray shaded histograms show the sum of all considered background processes.



(a) η of second jet of charged Higgs decay



(b) η of extra jet not associated to the tops and the H^+



(c) Invariant mass between 2nd jet of H^+ and one extra jet

Figure D.2: Normalized distributions of variables not used for H^+ event selection but showing some discriminating power to separate signal and background. The colors denote different charged Higgs boson masses. The gray shaded histograms show the sum of all considered background processes.

List of Figures

2.1	Shape of the Standard Model Higgs potential for a negative value of μ^2	9
2.2	Theoretically allowed region for the Higgs boson mass m_H in dependence of the cut-off scale Λ	12
2.3	$\Delta\chi^2$ vs. m_H curve of the fit using all electroweak data	13
2.4	Observed and expected 95% CL upper limits on the ratios to the SM cross-section, as functions of the Higgs boson mass	14
2.5	Evolution of the inverse of the three coupling constants in the Standard Model and in SUSY	15
2.6	Charged Higgs boson exclusion limits from direct searches	23
2.7	Charged Higgs boson exclusion from B physics and other constraints	24
2.8	Feynman diagrams for the signal process	25
2.9	Charged Higgs boson branching ratios	25
2.10	Charged Higgs boson production cross-section	26
2.11	Charged Higgs boson production cross-section times branching ratio	26
3.1	Schematic layout of the LHC at CERN	28
3.2	Production cross-sections and event rates for the dominant processes in proton-(anti)proton collisions	30
3.3	Cut-away view of the ATLAS detector	31
3.4	Sketch of the ATLAS magnet system with the central solenoid and the three toroids	32
3.5	Cut-away view of the ATLAS inner detector	34
3.6	Cut-away view of the ATLAS calorimeter system	36
3.7	Cut-away view of the ATLAS muon spectrometer	38
3.8	Schematic view of the muon trigger system	39
3.9	The ATLAS trigger system	40
4.1	Feynman diagrams for heavy charged Higgs boson production and decay	43
5.1	Example of Feynman diagrams for the $t\bar{t}b\bar{b}$ QCD production	46
5.2	Example of Feynman diagrams for the $t\bar{t}b\bar{b}$ electroweak production	46
5.3	Representation of a hadron jet from a b quark	49
5.4	Distribution of the second highest impact parameter significance S_{d_0} for data and Monte Carlo	51
5.5	Jet b -tagging weight distribution and light jet rejection versus jet p_T	52
5.6	Integrated light jet rejection rate over jet p_T versus b -tagging efficiency	53
5.7	Normalized distribution of the number of jets per event	54
5.8	Minimal distance in ΔR between generated parton and reconstructed jet	56
5.9	Criteria of matching lepton to generator objects	57

5.10	Minimal distance in ΔR between generated neutrino and the two calculated neutrino solutions	57
5.11	Normalized distributions of kinematic variables of the $t\bar{t}$ sample used for event selection	60
5.12	Normalized distribution of the number of extra jets per event	61
5.13	Distribution of the resolution of p_T and ϕ of the missing transverse energy.	68
5.14	Distribution of the resolution of p_T , η and ϕ of b -jets.	69
5.15	Distribution of mean and one standard deviation of the resolution of p_T and ϕ of the missing transverse energy.	70
5.16	Distribution of the mean and its statistical uncertainty of the resolution of p_T , η and ϕ of b -jets in intervals of p_T and η	70
5.17	Distribution of the standard deviation and its statistical uncertainty of the resolution of p_T , η and ϕ of b -jets in intervals of p_T and η	71
5.18	Minimum χ^2 (left) and $\text{prob}(\chi^2)$ (right) distribution of the $t\bar{t}$ sample.	73
5.19	Purity versus efficiency of the kinematic fit for different cuts on χ_{min}^2 for the $t\bar{t}$ sample.	74
5.20	Purity versus the χ_{min}^2 cut value and purity versus number of expected events for the $t\bar{t}$ events.	74
5.21	Minimum χ^2 distribution of the $t\bar{t}$ and various background samples for an integrated luminosity of 30fb^{-1}	75
5.22	Purity versus efficiency and purity versus number of expected events for $t\bar{t}$ +background events.	76
5.23	Reconstructed invariant masses of the hadronically and leptonically decaying top quark after kinematic fit.	77
5.24	Normalized distributions of the correctly reconstructed charged Higgs boson mass.	78
5.25	Normalized distributions of the fitted hadronic and leptonic charged Higgs boson mass.	79
5.26	Normalized distributions of variables used for H^+ event selection	81
5.27	Normalized distributions of variables used for H^+ event selection	82
5.28	Distribution of the invariant charged Higgs boson masses for the three b -tag analysis	86
5.29	Distribution of the invariant charged Higgs boson masses for the three b -tag + extra jet analysis	87
7.1	5σ discovery and 95% CL exclusion contour for the three b -tag analysis	97
7.2	5σ discovery and 95% CL exclusion contour for the three b -tag + extra jet analysis	98
A.1	Schematic representation of the ATLAS full chain Monte Carlo production	103
B.1	Distribution of the integrated resolution of p_T , η and ϕ of the electron.	105
B.2	Distribution of the mean and its statistical uncertainty of the resolution of p_T , η and ϕ of the electron in intervals of p_T and η	106
B.3	Distribution of the standard deviation and its statistical uncertainty of the resolution of p_T , η and ϕ of the electron in intervals of p_T and η	106

B.4	Distribution of the integrated resolution of p_T , η and ϕ of the muon. . . .	107
B.5	Distribution of the mean and its statistical uncertainty of the resolution of p_T , η and ϕ of the muon in intervals of p_T and η	107
B.6	Distribution of the standard deviation and its statistical uncertainty of the resolution of p_T , η and ϕ of the muon in intervals of p_T and η	108
B.7	Distribution of the integrated resolution of p_T , η and ϕ of light jets. . . .	108
B.8	Distribution of the mean and its statistical uncertainty of the resolution of p_T , η and ϕ of light jets in intervals of p_T and η	109
B.9	Distribution of the standard deviation and its statistical uncertainty of the resolution of p_T , η and ϕ of light jets in intervals of p_T and η	109
C.1	Purity versus efficiency of the kinematic fit compared to an alternative χ^2	112
C.2	Purity versus efficiency for different cuts on χ_{min}^2 for the $t\bar{t}$ sample with equal top quark mass constraint	113
C.3	Reconstructed and fitted invariant masses of the hadronically and leptonically decaying top quark after kinematic fit of the $t\bar{t}$ sample	114
C.4	Purity versus efficiency for different cuts on χ_{min}^2 for the $t\bar{t}$ sample with unbinned resolutions	114
C.5	Purity versus efficiency for different cuts on χ_{min}^2 for the $t\bar{t}$ sample with no offset correction	115
D.1	Normalized distributions of variables not used for H^+ event selection . .	118
D.2	Normalized distributions of variables not used for H^+ event selection . .	119

List of Tables

2.1	Fundamental fermionic content of the Standard Model	4
2.2	Fundamental representation of quarks and leptons in the electroweak interaction	7
2.3	Particle content of the MSSM	18
5.1	Charged Higgs boson cross-sections	47
5.2	Background cross-sections	48
5.3	Selection yields for $\tan\beta = 30$ and an integrated luminosity of 30 fb^{-1}	59
5.4	Optimized cut values for the three b -tag and three b -tag + extra jet analysis	83
5.5	Selection yields for $\tan\beta = 30$ and an integrated luminosity of 30 fb^{-1} for four different H^+ masses and combined background components	85
5.6	Pure statistical significance for the three b -tag and three b -tag + extra jet analysis for $\tan\beta = 70$	85
6.1	Recommended values for systematic uncertainties and resolution functions used to estimate the experimental systematic effects	90
6.2	Number of selected events within a mass window of 100GeV around the nominal H^+ mass and the effects of systematic uncertainties for the three b -tag analysis	91
6.3	Number of selected events within a mass window of 100GeV around the nominal H^+ mass and the effects of systematic uncertainties for the three b -tag + extra jet analysis	92

Bibliography

- [1] S. L. Glashow, *Partial Symmetries of Weak Interactions*, Nucl. Phys. **22** (1961) 579–588.
- [2] S. Weinberg, *A Model of Leptons*, Phys. Rev. Lett. **19** (1967) no. 21, 1264–1266.
- [3] A. Salam, *Weak and Electromagnetic Interactions*, . Originally printed in *Svartholm: Elementary Particle Theory, Proceedings Of The Nobel Symposium Held 1968 At Lerum, Sweden*, Stockholm 1968, 367-377.
- [4] K. Nakamura et al., *The Review of Particle Physics*, Journal of Physics G **37** (2010) 075021. <http://pdg.lbl.gov/>.
- [5] A. Pich, *Aspects of quantum chromodynamics*, arXiv:hep-ph/0001118.
- [6] J. Luo, L.-C. Tu, Z.-K. Hu, and E.-J. Luan, *New Experimental Limit on the Photon Rest Mass with a Rotating Torsion Balance*, Phys. Rev. Lett. **90** (2003) no. 8, 081801.
- [7] C. S. Wu, E. Ambler, R. W. Hayward, D. D. Hoppes, and R. P. Hudson, *Experimental Test of Parity Conservation in Beta Decay*, Phys. Rev. **105** (1957) no. 4, 1413–1415.
- [8] R. L. Garwin, L. M. Lederman, and M. Weinrich, *Observations of the Failure of Conservation of Parity and Charge Conjugation in Meson Decays: the Magnetic Moment of the Free Muon*, Phys. Rev. **105** (1957) no. 4, 1415–1417.
- [9] J. I. Friedman and V. L. Telegdi, *Nuclear Emulsion Evidence for Parity Nonconservation in the Decay Chain $\pi^+ \rightarrow \mu^+ + e^+$* , Phys. Rev. **105** (1957) no. 5, 1681–1682.
- [10] Super-Kamiokande Collaboration, Y. Fukuda et al., *Evidence for oscillation of atmospheric neutrinos*, Phys. Rev. Lett. **81** (1998) 1562–1567, arXiv:hep-ex/9807003.
- [11] KamLAND Collaboration, K. Eguchi et al., *First results from KamLAND: Evidence for reactor anti- neutrino disappearance*, Phys. Rev. Lett. **90** (2003) 021802, arXiv:hep-ex/0212021.
- [12] K2K Collaboration, M. H. Ahn et al., *Indications of Neutrino Oscillation in a 250 km Long- baseline Experiment*, Phys. Rev. Lett. **90** (2003) 041801, arXiv:hep-ex/0212007.
- [13] SNO Collaboration, Q. R. Ahmad et al., *Direct evidence for neutrino flavor transformation from neutral-current interactions in the Sudbury Neutrino Observatory*, Phys. Rev. Lett. **89** (2002) 011301, arXiv:nucl-ex/0204008.

- [14] E. Komatsu et al., *Seven-Year Wilkinson Microwave Anisotropy Probe (WMAP) Observations: Cosmological Interpretation*, arXiv:1001.4538 [astro-ph.CO].
- [15] F. Englert and R. Brout, *Broken Symmetry and the Mass of Gauge Vector Mesons*, Phys. Rev. Lett. **13** (1964) no. 9, 321–323.
- [16] P. W. Higgs, *Broken Symmetries and the Masses of Gauge Bosons*, Phys. Rev. Lett. **13** (1964) no. 16, 508–509.
- [17] G. S. Guralnik, C. R. Hagen, and T. W. B. Kibble, *Global Conservation Laws and Massless Particles*, Phys. Rev. Lett. **13** (1964) no. 20, 585–587.
- [18] M. Spira and P. M. Zerwas, *Electroweak symmetry breaking and Higgs physics*, Lect. Notes Phys. **512** (1998) 161–225, arXiv:hep-ph/9803257.
- [19] K. Riesselmann, *Limitations of a standard model Higgs boson*, arXiv:hep-ph/9711456.
- [20] ALEPH Collaboration, J. Alcaraz, *Precision Electroweak Measurements and Constraints on the Standard Model*, arXiv:0911.2604 [hep-ex].
- [21] LEP Electroweak Working Group, *Update for Summer 2010*, <http://lepewwg.web.cern.ch/LEPEWWG/plots/summer2010/>.
- [22] LEP Working Group for Higgs boson searches Collaboration, R. Barate et al., *Search for the standard model Higgs boson at LEP*, Phys. Lett. **B565** (2003) 61–75, arXiv:hep-ex/0306033.
- [23] CDF Collaboration, F. Abe et al., *The CDF detector: an overview*, Nucl. Instr. Meth. **A271** (1988) 387–403.
- [24] DØ Collaboration, V. Abazov et al., *The upgraded DØ detector*, Nuclear Instruments and Methods in Physics Research Section A: Accelerators, Spectrometers, Detectors and Associated Equipment **565** (2006) no. 2, 463 – 537.
- [25] The TEVNPH Working Group of the CDF and DØ Collaboration, *Combined CDF and DØ Upper Limits on Standard Model Higgs- Boson Production with up to 6.7 fb⁻¹ of Data*, arXiv:1007.4587 [hep-ex].
- [26] G. D. Kribs, *Phenomenology of extra dimensions*, arXiv:hep-ph/0605325.
- [27] M. Perelstein, *Little Higgs models and their phenomenology*, Prog. Part. Nucl. Phys. **58** (2007) 247–291, arXiv:hep-ph/0512128.
- [28] K. Lane, *Two lectures on technicolor*, arXiv:hep-ph/0202255.
- [29] S. P. Martin, *A Supersymmetry Primer*, arXiv:hep-ph/9709356.
- [30] D. I. Kazakov, *Beyond the standard model (in search of supersymmetry)*, arXiv:hep-ph/0012288.

-
- [31] H. P. Nilles, *Supersymmetry, supergravity and particle physics*, Physics Reports **110** (1984) no. 1-2, 1 – 162.
- [32] S. Coleman and J. Mandula, *All Possible Symmetries of the S Matrix*, Phys. Rev. **159** (1967) no. 5, 1251–1256.
- [33] R. Haag, J. T. Lopuszanski, and M. Sohnius, *All possible generators of supersymmetries of the S-matrix*, Nuclear Physics B **88** (1975) no. 2, 257 – 274.
- [34] P. Fayet, *Spontaneously broken supersymmetric theories of weak, electromagnetic and strong interactions*, Physics Letters B **69** (1977) no. 4, 489 – 494.
- [35] H. E. Haber, *The status of the minimal supersymmetric standard model and beyond*, Nucl. Phys. Proc. Suppl. **62** (1998) 469–484, arXiv:hep-ph/9709450.
- [36] J. F. Gunion, H. E. Haber, G. L. Kane, and S. Dawson, *The Higgs Hunter’s Guide*. Addison Wesley, 2000.
- [37] V. Barger, J. L. Hewett, and R. J. N. Phillips, *New constraints on the charged Higgs sector in two-Higgs-doublet models*, Phys. Rev. D **41** (1990) no. 11, 3421–3441.
- [38] S. Kanemura, S. Moretti, Y. Mukai, R. Santos, and K. Yagyu, *Distinctive Higgs Signals of a Type II 2HDM at the LHC*, Phys. Rev. **D79** (2009) 055017, arXiv:0901.0204 [hep-ph].
- [39] D. P. Roy, *Charged Higgs boson search at the LHC*, AIP Conf. Proc. **805** (2006) 110–116, arXiv:hep-ph/0510070.
- [40] A. E. Nelson and L. Randall, *Naturally large $\tan[\beta]$* , Physics Letters B **316** (1993) no. 4, 516 – 520.
- [41] H. Baer, J. Ferrandis, and X. Tata, *Are supersymmetric models with large $\tan(\beta)$ natural?*, Phys. Lett. **B561** (2003) 145–152, arXiv:hep-ph/0211418.
- [42] M. S. Carena, S. Heinemeyer, C. E. M. Wagner, and G. Weiglein, *Suggestions for benchmark scenarios for MSSM Higgs boson searches at hadron colliders*, Eur. Phys. J. **C26** (2003) 601–607, arXiv:hep-ph/0202167.
- [43] M. S. Carena, S. Heinemeyer, C. E. M. Wagner, and G. Weiglein, *Suggestions for improved benchmark scenarios for Higgs- boson searches at LEP2*, arXiv:hep-ph/9912223.
- [44] ALEPH Collaboration, A. Heister et al., *Search for charged Higgs bosons in e^+e^- collisions at energies up to $\sqrt{s} = 209\text{-GeV}$* , Phys. Lett. **B543** (2002) 1–13, arXiv:hep-ex/0207054.
- [45] CDF Collaboration, A. Abulencia et al., *Search for charged Higgs bosons from top quark decays in $p\bar{p}$ collisions at $\sqrt{s} = 1.96\text{-TeV}$* , Phys. Rev. Lett. **96** (2006) 042003, arXiv:hep-ex/0510065.

- [46] DØ Collaboration, V. M. Abazov et al., *Search for charged Higgs bosons in decays of top quarks*, Phys. Rev. **D80** (2009) 051107, arXiv:0906.5326 [hep-ex].
- [47] DØ Collaboration, V. M. Abazov et al., *Search for charged Higgs bosons in top quark decays*, Phys. Lett. **B682** (2009) 278–286, arXiv:0908.1811 [hep-ex].
- [48] CDF Collaboration, *A search of charged Higgs in the decay products of pair-produced top quarks, 2005*, http://www-cdf.fnal.gov/physics/new/top/2005/1jets/charged_higgs/higgs/V2/MHTB_plane.html.
- [49] D. Eriksson, F. Mahmoudi, and O. Stal, *Charged Higgs bosons in Minimal Supersymmetry: Updated constraints and experimental prospects*, JHEP **11** (2008) 035, arXiv:0808.3551 [hep-ph].
- [50] L. Hall, J. Lykken, and S. Weinberg, *Supergravity as the messenger of supersymmetry breaking*, Phys. Rev. D **27** (1983) no. 10, 2359–2378.
- [51] O. Deschamps et al., *The Two Higgs Doublet of Type II facing flavour physics data*, arXiv:0907.5135 [hep-ph].
- [52] ALEPH Collaboration, S. Schael et al., *Search for neutral MSSM Higgs bosons at LEP*, Eur. Phys. J. **C47** (2006) 547–587, arXiv:hep-ex/0602042.
- [53] The ATLAS Collaboration, N. Andari et al., *Higgs Production Cross Sections and Decay Branching Ratios*, ATL-PHYS-INT-2010-030.
- [54] J. Alwall, *MATCHIG: A program for matching charged Higgs boson production at hadron colliders*, arXiv:hep-ph/0503124.
- [55] S. Heinemeyer, W. Hollik, and G. Weiglein, *FeynHiggs: a program for the calculation of the masses of the neutral CP-even Higgs bosons in the MSSM*, Comput. Phys. Commun. **124** (2000) 76–89, arXiv:hep-ph/9812320.
- [56] T. Plehn, *Charged Higgs boson production in bottom gluon fusion*, Phys. Rev. **D67** (2003) 014018, arXiv:hep-ph/0206121.
- [57] L. Evans and P. Bryant, *LHC Machine*, Journal of Instrumentation **3** (2008) no. 08, S08001.
- [58] The ATLAS Collaboration, G. Aad et al., *The ATLAS Experiment at the CERN Large Hadron Collider*, Journal of Instrumentation **3** (2008) no. 08, S08003.
- [59] The CMS Collaboration, R. Adolphi et al., *The CMS experiment at the CERN LHC*, Journal of Instrumentation **3** (2008) no. 08, S08004.
- [60] The LHCb Collaboration, A. Augusto Alves et al., *The LHCb Detector at the LHC*, Journal of Instrumentation **3** (2008) no. 08, S08005.
- [61] The ALICE Collaboration, K. Aamodt et al., *The ALICE experiment at the CERN LHC*, Journal of Instrumentation **3** (2008) no. 08, S08002.

-
- [62] CDF Collaboration, F. Abe et al., *Observation of top quark production in $\bar{p}p$ collisions*, Phys. Rev. Lett. **74** (1995) 2626–2631, arXiv:hep-ex/9503002.
- [63] DØ Collaboration, S. Abachi et al., *Observation of the top quark*, Phys. Rev. Lett. **74** (1995) 2632–2637, arXiv:hep-ex/9503003.
- [64] The ATLAS Collaboration, G. Aad et al., *Expected Performance of the ATLAS Experiment - Detector, Trigger and Physics*, arXiv:0901.0512 [hep-ex].
- [65] S. Catani, *Aspects of QCD, from the Tevatron to the LHC*, arXiv:hep-ph/0005233.
- [66] *ATLAS detector and physics performance: Technical Design Report, 1*. Technical Design Report ATLAS. CERN, Geneva, 1999.
- [67] *LCG Homepage*, <http://lcg.web.cern.ch/lcg/>.
- [68] C. Eck et al., *LHC computing Grid: Technical Design Report. Version 1.06 (20 Jun 2005)*. Technical Design Report LCG. CERN, Geneva, 2005.
- [69] G. Cowan, K. Cranmer, E. Gross, and O. Vitells, *Using the Profile Likelihood in Searches for New Physics*, arXiv:1007.1727 [physics.data-an].
- [70] S. Moch and P. Uwer, *Theoretical status and prospects for top-quark pair production at hadron colliders*, Phys. Rev. **D78** (2008) 034003, arXiv:0804.1476 [hep-ph].
- [71] Y. Kiyo, J. H. Kuhn, S. Moch, M. Steinhauser, and P. Uwer, *Top-quark pair production near threshold at LHC*, Eur. Phys. J. **C60** (2009) 375–386, arXiv:0812.0919 [hep-ph].
- [72] The ATLAS Collaboration, C. Bernius, S. Dean, and N. Konstantinidis, *Removing the matrix element / parton shower overlap in $t\bar{t}$ + jets backgrounds in the semileptonic $t\bar{t}H^0(H^0 \rightarrow b\bar{b})$ analysis*, ATL-COM-PHYS-2010-088.
- [73] A. Bredenstein, A. Denner, S. Dittmaier, and S. Pozzorini, *NLO QCD corrections to $pp \rightarrow t$ anti- t b anti- b + X at the LHC*, Phys. Rev. Lett. **103** (2009) 012002, arXiv:0905.0110 [hep-ph].
- [74] The ATLAS Collaboration, *Strategy to Search for Single-Top Events using early Data of the ATLAS Detector at the LHC*, ATL-PHYS-PUB-2010-003, May, 2010.
- [75] S. Tsuno et al., *GRPPA_4b: A Four bottom quark production event generator for $pp/p\bar{p}$ collisions*, Comput. Phys. Commun. **151** (2003) 216–240, arXiv:hep-ph/0204222.
- [76] S. Frixione and B. R. Webber, *Matching NLO QCD computations and parton shower simulations*, JHEP **06** (2002) 029, arXiv:hep-ph/0204244.
- [77] G. Corcella et al., *HERWIG 6.5: an event generator for Hadron Emission Reactions With Interfering Gluons (including supersymmetric processes)*, JHEP **01** (2001) 010, arXiv:hep-ph/0011363.

- [78] M. L. Mangano, M. Moretti, F. Piccinini, R. Pittau, and A. D. Polosa, *ALPGEN, a generator for hard multiparton processes in hadronic collisions*, JHEP **07** (2003) 001, arXiv:hep-ph/0206293.
- [79] B. P. Kersevan and E. Richter-Was, *The Monte Carlo event generator AcerMC version 1.0 with interfaces to PYTHIA 6.2 and HERWIG 6.3*, Comput. Phys. Commun. **149** (2003) 142–194, arXiv:hep-ph/0201302.
- [80] T. Sjostrand, S. Mrenna, and P. Z. Skands, *PYTHIA 6.4 Physics and Manual*, JHEP **05** (2006) 026, arXiv:hep-ph/0603175.
- [81] M. Cacciari et al., *The anti- k_t jet clustering algorithm*, JHEP04 **2008** (2008) no. 4, 063.
- [82] The ATLAS Collaboration, T. Göpfert, *Counting Signed Impact Parameter based b -tagging algorithm with ATLAS*, ATL-PHYS-INT-2009-064.
- [83] The ATLAS Collaboration, T. Göpfert, C. Lapoire, L. Vacavant, and K. Zenker, *Impact parameter-based b -tagging algorithms in the 7 TeV collision data with the ATLAS detector: the TrackCounting and JetProb algorithms*, ATLAS-CONF-2010-041, May, 2010.
- [84] The ATLAS Collaboration, N. Bousson et al., *Performance of Impact Parameter-Based b -tagging Algorithms with the ATLAS Detector using Proton-Proton Collisions at $\sqrt{s} = 7$ TeV*, ATLAS-CONF-2010-091, 2010.
- [85] private communication with M. Elsing. October, 2008.
- [86] V. Blobel and E. Lohrmann, *Statistische und numerische Methoden der Datenanalyse*. Teubner, 1998.
- [87] The ATLAS Collaboration, J. E. Sundermann and T. Göpfert, *KinFitter - A Kinematic Fit with Constraints*, ATL-COM-SOFT-2009-014.
- [88] T. Göpfert and J. E. Sundermann, *KinFitter - A Kinematic Fit with Constraints*, <https://twiki.cern.ch/twiki/bin/view/Atlas/KinFitter>.
- [89] The ATLAS Collaboration, *Prospects for the Top Pair Production Cross-section at $\sqrt{s} = 10$ TeV in the Single Lepton Channel in ATLAS*, ATL-PHYS-PUB-2009-087, Aug, 2009.
- [90] K. Cranmer, *Statistical Challenges for Searches for New Physics at the LHC*, in *Statistical Problems in Particle Physics, Astrophysics and Cosmology*. 2006. arXiv:physics/0511028.
- [91] S. S. Wilks, *The Large-Sample Distribution of the Likelihood Ratio for Testing Composite Hypotheses*, The Annals of Mathematical Statistics **9** (1938) no. 1, 60–62.
- [92] M. G. Kendall, A. Stuart, J. K. Ord, and S. Arnold, *Classical inference and the linear model; 6th ed.* Kendall's Adv. Theor. Stat. Springer, Berlin, 1999.

- [93] R. Brun and F. Rademakers, *ROOT – An object oriented data analysis framework*, Nuclear Instruments and Methods in Physics Research Section A: Accelerators, Spectrometers, Detectors and Associated Equipment **389** (1997) no. 1-2, 81 – 86. New Computing Techniques in Physics Research V.
- [94] S. Jadach, J. H. Kühn, and Z. Was, *TAUOLA - a library of Monte Carlo programs to simulate decays of polarized [tau] leptons*, Computer Physics Communications **64** (1991) no. 2, 275 – 299.
- [95] E. Barberio and Z. Was, *PHOTOS - a universal Monte Carlo for QED radiative corrections: version 2.0*, Computer Physics Communications **79** (1994) no. 2, 291 – 308.

Danksagung

Zum Schluss möchte ich mich bei all denjenigen bedanken, ohne die diese Arbeit nicht möglich gewesen wäre.

Mein Dank geht an Herrn Prof. Kobel für die gute Betreuung und die Möglichkeit, diese Arbeit in der ATLAS Kollaboration anzufertigen. Der Freiraum und die Möglichkeit viele meiner Ideen zu verwirklichen hat mir viel bedeutet.

Bei Heiko Lacker bedanke ich mich, dass er sich so spontan bereit erklärt hat, als Gutachter dieser Dissertation zu fungieren.

Die ganze Arbeit wäre nicht möglich gewesen ohne die aufopfernde Arbeit von Rainer Schwierz und Andreas Petzold für unsere Rechnersysteme. Mein Dank gilt auch dem ZiH für die Bereitstellung, Wartung und freundliche Nutzerbetreuung des Hochleistungsrechenzentrums.

Insbesondere möchte ich mich bei Martin zur Nedden für die Betreuung während der Endphase dieser Arbeit bedanken, bei Martin Flechl für die Unterstützung bei der Produktion des Signal Monte Carlos, bei Verena Klose und Jan Erik Sundermann für die erfolgreiche Umsetzung des KinFitter Projektes, bei Christian Weiser, Gordon Watts und Laurent Vacavant für die hilfreichen Diskussionen in der *b*-tagging Gruppe und deren Unterstützung bei der Umsetzung meines *b*-tagging Projektes und bei allen Korrekturlesern, wobei Arno Straessner ganz besonderer Dank gilt.

Und natürlich möchte ich mich bei der ganzen Belegschaft des IKTP bedanken, es war eine schöne Zeit. Viel Spaß und Ablenkung, körperlicher und geistiger Art, hatte ich vor allem bei unseren Trainingseinheiten im Beutlerpark. Ich finde es immer noch erstaunlich, dass man dort die meisten Raucher getroffen hat.

Ganz besonderer, persönlicher Dank geht an meine Familie und Verena.

Versicherung

Hiermit versichere ich, dass ich die vorliegende Arbeit ohne unzulässige Hilfe Dritter und ohne Benutzung anderer als der angegebenen Hilfsmittel angefertigt habe; die aus fremden Quellen direkt oder indirekt übernommenen Gedanken sind als solche kenntlich gemacht. Die Arbeit wurde bisher weder im Inland noch im Ausland in gleicher oder ähnlicher Form einer anderen Prüfungsbehörde vorgelegt.

Diese Arbeit wurde am Institut für Kern- und Teilchenphysik der Technischen Universität Dresden unter wissenschaftlicher Betreuung von Prof. Dr. M. Kobel angefertigt.

Es haben keine früheren erfolglosen Promotionsverfahren stattgefunden.

Ich erkenne die Promotionsordnung der Fakultät Mathematik und Naturwissenschaften an der Technischen Universität Dresden vom 20. März 2000, in der Fassung der vom Fakultätsrat am 19.06.2002 und 12.07.2002 beschlossenen und mit Erlass des Sächsischen Staatsministeriums für Wissenschaft und Kunst vom 18.03.2003 genehmigten Änderungen gemäß Satzung vom 16.04.2003, an.

Dresden, den 22.11.2010

Thomas Göpfert